CARBON NANOMATERIALS AND THEIR ELECTROCHEMICAL APPLICATIONS

by

Yifan Tang

B.S., Nanjing University, 2007

Submitted to the Graduate Faculty of

The Dietrich School of Arts and Sciences in partial fulfillment

of the requirements for the degree of

Doctor of Philosophy

University of Pittsburgh

2013

UNIVERSITY OF PITTSBURGH

The Dietrich School of Arts and Sciences

This dissertation was presented

by

Yifan Tang

It was defended on

June 28, 2013

and approved by

Dr. Adrian C. Michael, Professor, Department of Chemistry

Dr. Geoffrey Hutchison, Assistant Professor, Department of Chemistry

Dr. Tomasz Kowalewski, Professor, Department of Chemistry, Carnegie Mellon University

Committee Chair: Dr. Alexander Star, Associate Professor, Department of Chemistry

Copyright © by Yifan Tang

2013

CARBON NANOMATERIALS
AND THEIR ELECTROCHEMICAL APPLICATIONS

Yifan Tang, PhD

University of Pittsburgh, 2013

Recent years have witnessed the continuously growing interest in the area of nanotechnology. Among the innumerable novel compounds and materials, carbon nanomaterials, especially carbon nanotubes (CNTs) and graphene, are undeniably two of the most glorious shining stars due to their unique structures and promising physical, chemical, and electrical properties. Numerous research projects have been focused on the synthesis, characterization, and functionalization of carbon nanomaterials, as well as their enormous possible applications in energy generation/storage, sensors, electronics, reinforcement of composite materials, and drug delivery.

Of particular interest in this dissertation are the functionalization of carbon nanomaterials − either by decorating with Pt nanoparticles (NPs) or by doping with nitrogen atoms − and their electrochemical applications for both fuel cell catalysts (and supports) and electrochemical sensors/biosensors. I have successfully synthesized and characterized hybrid structures of Pt NP-CNTs or Pt NP-graphene, and also a novel carbon nanomaterial − nitrogen doped carbon nanotube cups (NCNCs). The electrochemical properties and applications of these nanomaterials were also investigated.

Pt NP decorated CNTs or graphene were studied and compared for their electrochemical sensor performance in order to obtain further understanding on the structure-property relationship between 1-dimensional and 2-dimensional nanomaterials as the sensing platform.

Both Pt-CNTs and NCNCs were investigated as fuel cell catalysts with the aim of improving the performance and stability, decreasing the amount of expensive Pt, and most importantly, understanding and optimizing NCNCs as non-precious-metal catalysts to ultimately replace expensive Pt-based catalysts. Pt-CNTs demonstrated extraordinary stability with less material used compared to commercial Pt/C catalysts in long term stability testing. NCNCs also exhibited good catalytic activity towards oxygen reduction reaction (ORR) which makes them promising alternatives to Pt-based catalysts. Further look into the ORR mechanism suggested that the presence of both nitrogen and iron from catalyst of NCNCs synthesis process is crucial for the improved ORR catalytic activity.

From the materials point of view, a novel simple sonication method was studied to separate stacked NCNCs into individual nanocups structures, with the long-term objective of drug delivery or nano-reactor applications. Both the separation mechanism and the structure-property relationship of the stacked and separated NCNCs were investigated.

TABLE OF CONTENTS

LIST OF TABLES

LIST OF FIGURES

PREFACE

First, I would like to express my sincere gratitude and appreciation to my research advisor, Professor Alexander Star, for his guidance through my six years' perusing in graduate school. He has been a great mentor for my development, changing me from a student with curiosity in the nano-world to a real scientist. I do benefit tremendously from his insights and ideas on the projects, his attitude and enthusiasm towards scientific research and of course his full support and encouragement of my graduate studies and research. It is really an honor to work with him and learn from him.

I would like to thank my committee members, Professor Adrian Michael, Professor Geoffrey Hutchison and Professor Tomasz Kowalewski, for their patience, valuable suggestions, as well as their inspirational discussions and excellence in their respective fields.

I would also like to thank all members of the Star Group, past and present, and our collaborators for their help, participation and suggestions on my research over the years, making my graduate school experience a more enjoyable journey. Special thanks go to Dr. Douglas R. Kauffman for his valuable assistance and help as senior group member at the very beginning stage of my own research, also for setting up a great example in the group. I am also grateful to have Dr. Yanan Chen, Dr. Mengning Ding, Gregg P. Kotchey, and Yong Zhao around, for their help in the research, as well as our memorable lunch time chatting, discussion and sharing of wisdom throughout all these years. I extend my gratitude to Mingjiang Zhong and Dr. Gowtam

Atthipalli, who are the best collaborators outside the chemistry department. To Seth C. Burkert, your reliable assistance on CVD and electrochemistry is really appreciated. To all other past members of the group, Dr. Harindra Vedala, Dr. Pingping Gou, Sruti Bhaumik, Ian Feigel, Brian Barth and also current members Dr. Nadine Kraut, Dr. Haifeng Dong, Hao Bai, Gordon Chiu, Zachary Michael, Wanji Seo, James E. Ellis, Gregory J. Morgan and James Gaugler, it was really great working with you and I wish you all the very best.

I would like to extend my gratitude to the entire faculty and students of the Department of Chemistry as well as all the staff members for their assistance throughout my six years life in Pittsburgh. In particular, I want to thank Fran Nagy, our former Graduate Student Administrator, for making my life in the department so much delightful. To Tom Gasmire and Jeff Sicher from the chemistry machine shop and Chuck Fleishaker from the chemistry electronics shop, you are the ones who helped to turn my imagination (design of experiment setups) into reality. I would also like to thank Albert Stewart and Cole Van Ormer from MEMS and Tom Harper from the Department of Biological Science for their assistance with electron microscopy, Michael L. McDonald and Dr. Susheng Tan from NFCF for help in the cleaning room, RJ LEE group and Professor Richard A. Butera for their help with XPS analysis.

I would not have been able to achieve my goals without the love and support of my family and friends. I have my most sincere appreciation to my parents, for their unconditional love, support and encouragement to pursue my dreams, even if this means to be thousands of miles away from them for a long long time. To my dear friends from graduate school, college, high school, and middle school, here in the U.S., back in China or elsewhere, some of whom have already been named, thank you for the support and help and I do treasure our precious friendship.

And last, but certainly not least, I am forever indebted to my girlfriend Yangmiao Zhang. Your warmth, understanding, encouragement and kind indulgence have given me the strength and confidence to finish this journey. Although separated apart by the distance most of the time, every moment being with you, physically or mentally, is always joyful, not matter how hard the life is.

In the end, I would like to extend my gratitude to University of Pittsburgh, National Science Foundation and the Bayer MaterialScience for the financial support.

1.0 INTRODUCTION

Carbon nanomaterials, especially carbon nanotubes (CNTs) and graphene are the raising stars at the forefront of materials research. Graphene can be described as a one-atomic thick layer of sp^2 hybridized carbon, or one sheet of graphite, and is recognized as the basic building block for other graphitic materials.[1-2] Carbon nanotubes, on the other hand, can be viewed as a cylindrical structure formed by rolling up a sheet or multiple sheets of graphene.[3] Although having the simplest chemical composition and atomic bonding configuration of graphitic sp^2 carbons, carbon nanotubes and graphene exhibit great, perhaps the highest diversity and richness in structures and structure-property relationships among nanomaterials.[4] Due to their unique structures, CNTs and graphene possess extraordinarily high aspect ratio (length to diameter, for CNTs) or surface-to-volume ratio (for graphene), as well as the resulted outstanding electrical, mechanical and chemical/electrochemical properties. This allows many attractive applications in a variety of disciplines, such as sensors,[5-10] catalysts,[11-15] energy generation/storage,[16-19] electronic devices,[20-23] composite materials,[24-27] and drug delivery.[28-29] Moreover, the chemical functionalization of CNTs and graphene, such as doping with nitrogen atoms[30-32] or decorating with nanoparticles,[33-35] is of great interest to further tailor the structures and proprieties of the carbon nanomaterials. The resulting materials could demonstrate further enhanced properties for applications such as sensors or fuel cell catalysts.

1.1 CARBON NANOTUBES AND GRAPHENE

Carbon nanotubes (CNTs) were commonly recognized as first discovered by Sumio Iijima in his highly cited nature work in 1991[36] on the topic of arc-discharge synthesis of needle-like graphitic carbon tubes. After about a decade, in 2004, free standing graphene was experimentally obtained by Geim and Novoselov at the University of Manchester,[37] who later shared the Nobel Prize in Physics in 2010. Both CNTs and graphene are new allotropes of carbon, compared to graphite or diamond. And each of them became the focus of extensive researches soon after their discovery. As the scope of this document is primarily focusing on CNTs, with graphene being mentioned in some chapters, the following introduction sections would cover graphene briefly and more extensively CNTs related topics.

1.1.1 Structures and Properties

Graphene is a one-atomic thick layer of sp^2 carbon atoms tightly packed into a two-dimensional (2D) honeycomb lattice as shown in Figure 1-1a.[1-2] The 2D structure of graphene resulted in a lot of unique and interesting properties, such as an ambipolar electric field-effect along with ballistic conduction of charge carriers,[37] high elasticity and great mechanical strength,[38] extraordinarily high surface-to-volume ratio,[39] and rapid heterogeneous electron transfer.[1-2, 40-41] Ideally, graphene should only have one single layer, however, bi-layer and few-layer (three to ten layers) graphene are also considerably interesting materials due to their distinct properties from stacking and also the limitations of the production methods.[2, 41-42]

Single-walled carbon nanotubes (SWNTs) are one-dimensional (1D) tube structures formed by rolling up one graphene sheet seamlessly (Figure 1-1b).[3] They are usually 0.4-2.0 nm

in the diameter while the length can vary from a few hundred nanometers to several millimeters.[40] On the other hand, multi-walled carbon nanotubes (MWNTs) consist of several concentrically nestled SWNTs sharing a common longitudinal axis, with a diameter of 2–100 nm and an inter-tubular distance of 0.34 nm (Figure 1-1c).[43] In a broader concept, MWNTs may occur in various morphologies[44] such as "hollow tube",[36] "bamboo",[45] "herringbone",[46] "stacked-cups"[31, 47] or even "filamentous carbons",[48] depending on their method of preparation.

The properties of SWNTs are mainly defined by the way that the graphene sheet is rolled up, which could be quantified using a pair of integers - the chirality vectors ($\mathbf{c}_h = n\mathbf{a_1} + m\mathbf{a_2} =$ (n, m)). Depending on the values of the chirality vectors, SWNTs can be classified into three types: armchair (n=m), zigzag (m=0) and chiral (n≠m). The electronic properties are directly related to the vectors/types: all armchair SWNTs are metallic; if (n - m) is a multiple of 3, the SWNTs are semiconductors with a tiny band gap, which also have metallic behavior; and all the rest are semiconductors with a band gap which inversely depends on the nanotube diameter.[3, 22, 49] For MWNTs, in the ideal case, their properties should be rather similar to those of perfect SWNTs, because the interaction between the cylinders is weak.[3] However, in reality, since there is no particular control on the chiralities of individual cylindrical tubes, MWNTs will typically be composed of a mixture of SWNTs with different chiralities, thereby resembling turbostratic graphite and will exhibit a metallic behavior.[43]

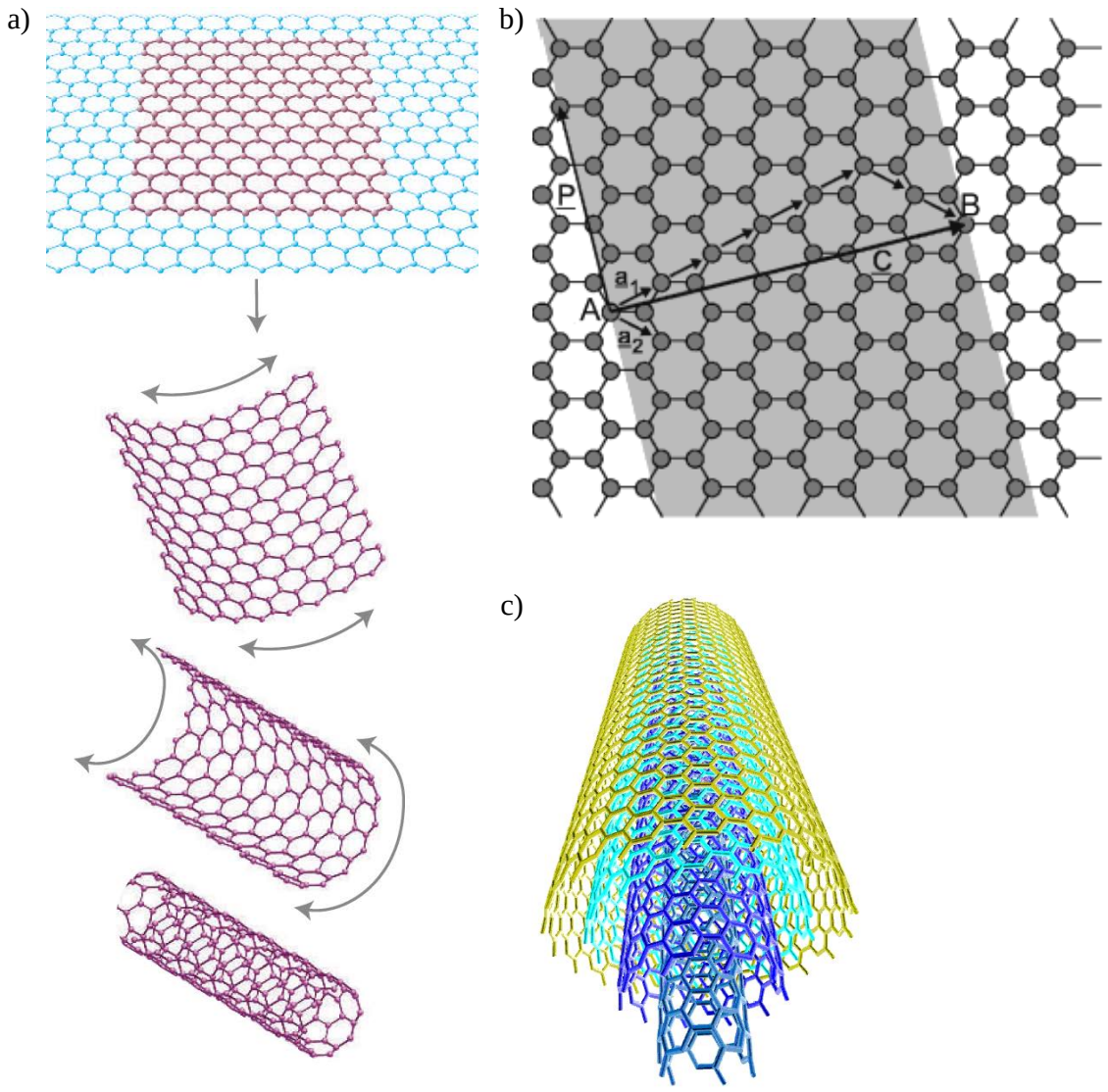

Figure 1-1. a) Schematic illustration of a single layer graphene (top) and the rolling of graphene into single-walled carbon nanotube (SWNT), adapted from ref 1; b) Schematic illustration of a graphene sheet by the $c_h = na_1 + ma_2 = (n, m)$, where a1 and a2 are the unit vectors of the hexagonal lattice, adapted from ref 20; c) Representation of a multi-walled carbon nanotube (MWNT), adapted from ref 50.

1.1.2 Synthesis of Carbon Nanotubes and Graphene

Currently, there are three major techniques to synthesize carbon nanotubes: (i) arc discharge,[36] (ii) laser ablation,[51] and (iii) chemical vapor deposition (CVD).[52] Other techniques have been also reported, such as rolling of graphene/graphite,[53-54] flame synthesis,[55] electrolysis,[56] or solar synthesis[57]. However these methods have not yet been developed to reach a stage of large scale synthesis as the first three.

Arc discharge technique involves applying a direct current (DC) between two close spaced (<1 mm) graphite electrodes in an inert gas (helium or argon) at a low pressure as shown in Figure 1-2a. The high current generates high temperature plasma and evaporates the carbon anode, depositing CNTs and other carbon by-products on the cathode.[58-59] Large scale synthesis of MWNTs was achieved by Ebbesen and Ajayan in gram scale with diameters of 2 ~ 20 nm and lengths in micrometer scale.[60] By co-evaporation of graphite and metal catalysts, SWNTs with diameters around 1.4 nm were also obtained in high yields (70–90%).[61]

Laser ablation technique shares a similar basic principle with the arc discharge method: evaporation of the carbon source at high temperature. Here the carbon is vaporized from the surface of a solid disk of graphite into a high-density helium (or argon) flow, by heating with a focused pulsed laser in a furnace (Figure 1-2b).[59] The evaporated carbon species are carried by the inert gas from the high-temperature zone and deposited on a conical water-cooled copper collector.[59] In 1996, Smalley and co-workers achieved the growth of high quality SWNTs at the 1–10 g scale with a yield >70% by laser ablation (vaporization) of graphite rods with small amounts of Ni and Co at 1200 °C.[62]

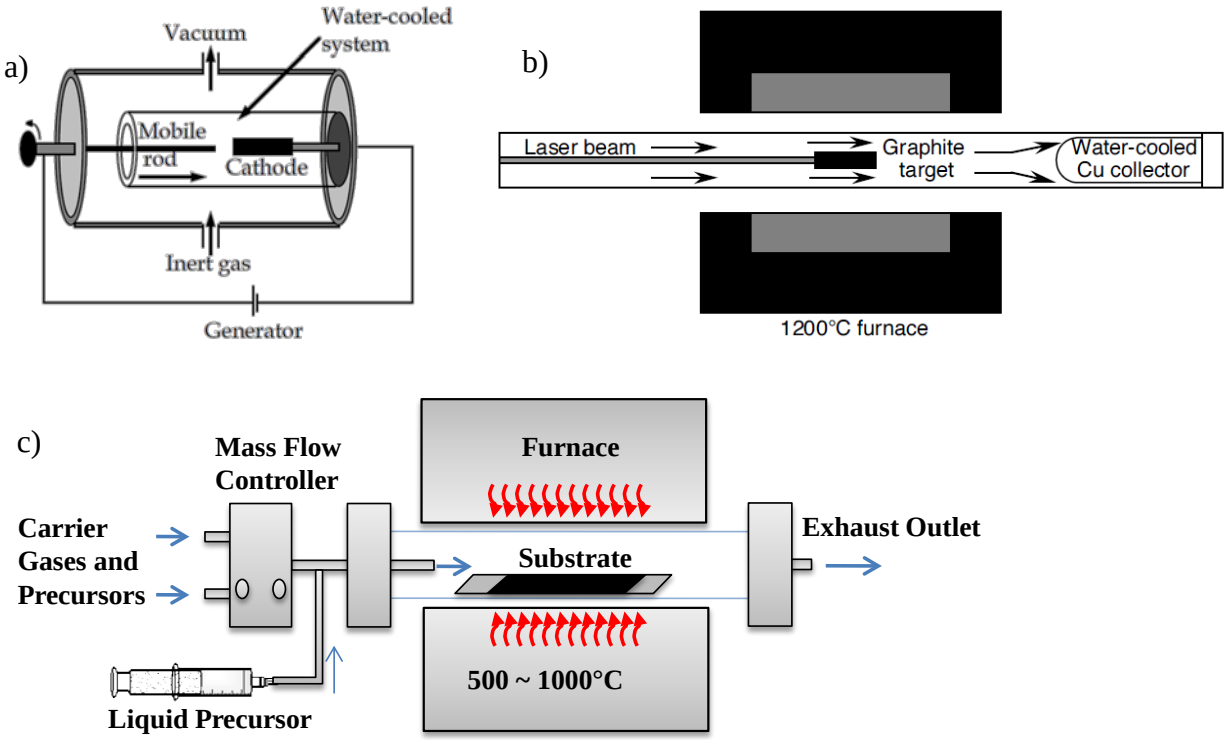

Figure 1-2. Schematic illustration of the apparatus for different synthesis techniques used for the production of carbon nanotubes (CNTs): a) arc discharge, b) laser ablation, c) chemical vapor deposition (CVD); d) Photograph of our current CVD system. Panel a and b adapted from ref 59.

Although both arc discharge and laser ablation techniques can produce CNTs with high quality and in large quantities, they still have some drawbacks: (i) they rely on evaporation of

carbon atoms from solid targets such as graphite at extremely high temperature and thus is economically unfavorable, and (ii) the CNTs are tangled and mixed randomly which complicates the purification process and their further applications.[58] So we will focus on the third and probably one of the most commonly used techniques for the synthesis of CNTs – chemical vapor deposition.

Chemical vapor deposition technique is a promising method which provides great feasibility for the controlled growth of CNTs compared to arc discharge and laser ablation.[63] Its basic principle involves the thermo decomposition of a flow of hydro-carbon precursors - typically with the aid of transition metal/metal alloy catalysts - in a tube furnace at relatively low temperatures (500 – 1000 °C) then the growth of CNTs over the catalysts upon cooling of the system.[59] The adoption of hydro-carbon rather than solid graphite as the precursor, combined with the use of catalysts significantly lowers the reaction temperature, making the reaction setup much simpler and the process more economical. Figure 1-2c shows a schematic illustration of a typical CVD apparatus. Figure 1-2d is the photograph of our own house-built atmospheric pressure thermo CVD system for illustrative purposes. Most of the CVD growth discussed in the dissertation is done with this system.

Another great advantage of CVD technique is its great versatility. Almost all key components in the growth can be varied,[59] for example: the precursor and catalyst status (liquid or gas), the choice of hydrocarbon and also catalyst species, reaction temperature and pressure, and the possibility of in situ doping other elements such as nitrogen into CNTs, which will be discussed in the following section. Among those variations, the most important one would be the catalyst. It can be in a liquid form as volatile metalorganic compounds[64] to allow in situ decomposition and possible better dispersion if liquid hydrocarbon is used,[65] or in solid state

loaded on high-surface-area support[66] to obtain larger scale synthesis, or in the form of thin film/nano particle to achieve aligned[67] or patterned[23] growth.

For the synthesis of graphene, typically four predominant techniques are employed: (i) mechanical cleavage of graphite, either by scotch tape method[68] or direct sonication of graphite;[69] (ii) epitaxial growth on SiC;[70] (iii) CVD on metal substrates;[71] (iv) reduction of graphite oxide.[72-73] Other methods are also reported such as unzipping of CNTs[74] or electrochemical exfoliating from graphite electrode.[75] Here we will focus on the chemical reduction of graphite oxide which is the most popular method for large-scale synthesis of graphene. This process basically involves two step: (i) the oxidation of graphite in the presence of strong acids and oxidants[39] and (ii) the conversion of graphite oxide to graphene through a variety of chemical,[72] thermo[73] or ultraviolet-assisted photocatalytic[76] reduction methods.

1.1.3 Nitrogen-doped Carbon Nanomaterials

In recent years, significant research effort has been devoted to the further manipulation of the structure and properties of carbon nanomaterials as the synthesis techniques get more and more mature. One effective yet relatively new route that draws much attention is the doping of the pure carbon structure with hetero atoms, such as nitrogen atoms.[77] Nitrogen atoms doped in carbon nanotubes or graphene result in the conjugation between their lone-pair electrons and the π-system of the graphitic surface, which may create nanomaterials with novel structures and tailored electronic, chemical/electrochemical and mechanical properties.[78-79] They have demonstrated good electrochemical catalytic activities towards oxygen reduction reaction (ORR) and are proposed to be great candidates for substituting the expensive Pt-based catalysts in the cathode of fuel cells.[30-31]

1.1.3.1 Synthesis of Nitrogen-doped Carbon Nanomaterials

For the doping of nitrogen into carbon nanomaterials, there are generally two routes: in situ doping during the synthesis process and post-synthesis doping/functionalization. In situ doping is mainly used for the synthesis of nitrogen-doped CNTs, where the general material synthetic methods are not significantly altered compared to regular CNTs. A nitrogen source, either small molecules such as acetonitrile or ammonia, or large molecules such as nitrogen containing ionic liquids or even polymers, is added during the CVD[31, 47, 80] or pyrolysis process[81-83] in order to achieve the desired nitrogen doping. For the post-synthesis doping, chemical[84-85] or electrochemical[86] reactions are performed to functionalize the pre-synthesized CNTs or graphene with nitrogen atoms.

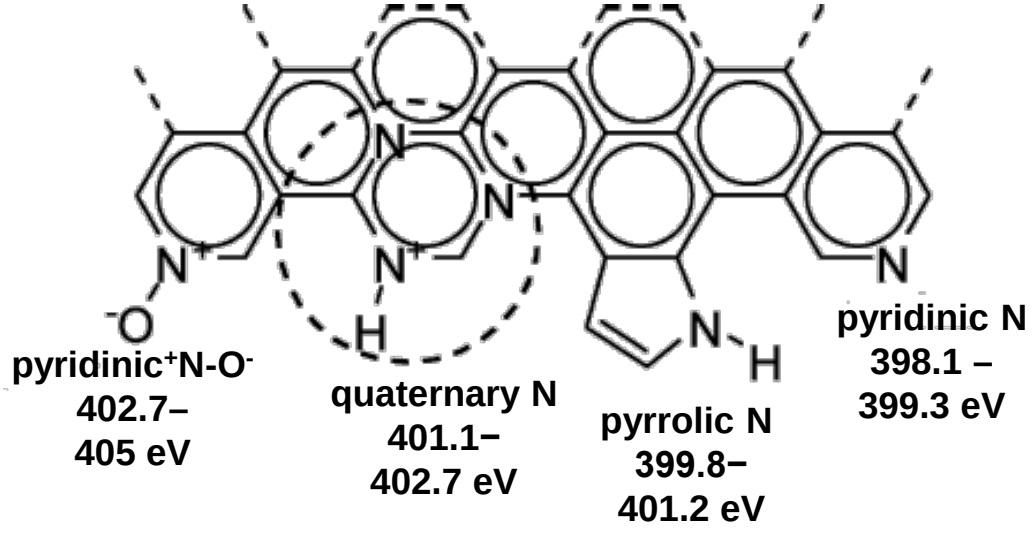

Figure 1-3. Various bonding configurations and their corresponding N1s XPS peak positions for nitrogen atoms in nitrogen-doped carbon nanomaterials, adapted from ref 77.

1.1.3.2 Different Nitrogen Functionalities

When nitrogen atoms are doped into carbon nanostructures, there are three primary structures that nitrogen usually exists in (Figure 1-3): (i) pyridine-like type, in which one p electron

contributes to the π-system; (ii) pyrrole-like type, with two p electrons in π-system; and (iii) graphitic (or quaternary) type, where the nitrogen atom takes the place of a graphitic sp^2 carbon atom and bonds to three carbon atoms.[32, 79, 87-88] Other types of nitrogen are also observed such as nitrogen oxides of pyridinic N or trapped nitrogen molecules (not shown). Furthermore, graphitic N could exist on both the edge and basal plane of graphitic surface while other types of nitrogen, especially pyridinic N, preferentially terminate the edge of graphitic surface[89-91].

A primary method to experimentally determine the various nitrogen functional groups is X-ray photoelectron spectroscopy (XPS). Based on the extensive study of nitrogen functionalities present in coals and chars by Pels el al[92] and also experimental[77] and theoretical[93] studies of others on nitrogen-doped carbon materials, the typical peak positions in N1s high-resolution spectrum for different nitrogen configurations are shown in Figure 1-3. It must be noted here that, unlike pure substance, such interpretation and assignment of different nitrogen functionalities is still relatively ambiguous and debatable due to the various local environments of nitrogen atoms incorporated into the graphitic structure and inhomogeneity of the nanomaterials. Large FWHM (full width at half maximum) is typically observed for the deconvoluted peaks. However we can still obtain important structural information from the fundamental principles of XPS. A peak with higher binding energy means a more positively charged atom which requires more energy to release an electron. The least positively charged nitrogen structure is pyridinic N at 398.1 – 399.3 eV, with a lone pair of electrons and only one p-electron contributing to the π-system; for pyrrolic N, two p-electrons contributing to the π-system makes the nitrogen more positively charged than pyridinic N and gives a high binding energy of 399.8 − 401.2 eV; graphitic/quaternary N demonstrates even higher peak position at 401.1 − 402.7 eV due to the bonding to three carbon atoms; and nitrogen functionalities with

even higher binding energies (402.7 – 405 eV) are typically attributed to nitrogen oxide (pyridinic-N^+–O^-) species.[77, 94-95]

Researchers suggested positive relationship between the ORR performance and the pyridine-like nitrogen.[87, 94] Some others believed graphitic nitrogen are primarily responsible for the ORR catalytic activity.[95-96] However the exact role of different nitrogen functionality towards the catalytic activity is still not quite clear yet.[94] The improved catalytic activity could be resulted from not only the nitrogen doping but also the catalysts residue during the synthesis of the nanomaterials,[97] or even a complex of C-N-metal structure.[98] Thus it would be necessary to investigate in depth the contribution of nitrogen doping, metal catalyst residue and also the possible C-N-metal hybrid structure. Details about nitrogen-doped carbon nanomaterials for ORR will be further covered in section 1.2.1.

1.1.4 Metal Nanoparticle and Carbon Nanomaterial Hybrid Structures

The study of metal nanoparticle (MNP) and carbon nanomaterial hybrid structures is another important aspect in nanotechnology. Carbon nanomaterials, especially CNTs and graphene, can provide an ideal graphitic surface/template for the physical absorption or chemical functionalization of zero-dimensional MNPs due to their large surface area, great structural stability and rich surface chemistry.[33] The resulted hybrid materials can demonstrate combined sometimes even synergistic properties,[99-100] thus have received considerable attentions in the syntheses, applications, as well as understanding of physical chemistry at the interfaces of such hybrid structures.[35]

Typical preparation routes of MNP-carbon nanomaterial hybrid structures could be divided into two major categories: physical methods and chemical methods.[34] Physical methods

typically involves sputtering[101], electron/ion beam evaporation[102], and laser ablation[103], and can provide excellent control over the size, shape, and uniformity of the MNPs.[104] Chemical methods can be further divided into two parts based on the origin of MNPs: (i) growing MNPs from precursors onto carbon nanomaterials or (ii) connecting pre-formed MNPs to carbon nanomaterials.[33] Salts of metals are commonly used as precursors for the growing of MNPs through various methods such as electrochemical deposition[105-106], electroless deposition,[107-108] or direct thermal/chemical reduction.[12, 109] These methods are most widely used for the synthesis of the hybrid structure due to the easy and versatile reaction conditions and scalability. The resulted MNPs would bind to CNTs or graphene either through van der Waals interactions or covalent interactions depending on the exact interface condition.[33, 35] On the other hand, connecting pre-formed MNPs could also achieve a diversity of linkage through covalent binding,[110] π-π interaction,[111-112] hydrophobic/hydrophilic interactions[113] or electrostatic interactions[10], with the advantage of being able to utilize the relative mature methodology of controlled synthesis of MNPs with well-defined structures and compositions.[35]

Among the numerous MNP-carbon nanomaterial hybrid structures,[114] platinum MNPs based ones are of particular interest here in this work because of their essential role in a broad area of heterogeneous[15]/electrochemical catalysis[115] and chemical[116]/electrochemical[117]/bio sensing.[118] The various synthetic routes are reported for PtNP-CNTs or PtNP-Graphene structures,[119] which are typical samples of the methods mentioned above. Details about the applications will be covered in section 1.2.

1.2 ELECTROCHEMICAL APPLICATIONS OF CARBON NANOMATERIALS

Carbon nanotubes and graphene are at the frontier of electrochemistry.[2, 13] With unique 1-D (CNTs) or 2-D structures (graphene), high surface area (1315 $m^2 g^{-1}$ for CNTs and 2630 $m^2 g^{-1}$ for graphene)[120], excellent electrical conductivity, outstanding stability and rich chemistry for further functionalization, they become crucial materials for various electrochemical applications, such as energy generation(fuel cells,[121-122] photovoltaic),[123-124] energy storage(batteries,[16] supercapacitors,[125] hydrogen storage),[126] field-effect transistors,[127-128] sensors[8] and biosensors.[9, 40] On the other hand, there are still a lot of uncertainties/drawbacks, such as the inhomogeneity of the materials,[7] lack of deep understanding of structure–property relationship,[63] and possible contamination from synthetic precursors/catalysts.[97, 129] These are great challenges but are also great opportunities. To solve the issues and obtain materials with improved electrochemical performance is one major driving force of our current research.

1.2.1 Fuel Cells

1.2.1.1 Fuel Cells

Among different energy storage/generation applications of carbon nanomaterials, we picked fuel cells as the research topic because they are an essential component of hydrogen economy[121] which would be a much cleaner and sustainable replacement of our current fossil fuel based economy in the future.

A fuel cell is an electrochemical device that can directly convert the chemical energy of fuels into electricity without combustion process.[130] As shown in Figure 1-3a, it is typically

composed of an anode, where fuels such as hydrogen or hydrocarbon get oxidized; a cathode, where oxidants such as oxygen or air get reduced; and an electrolyte, through which the ions can pass, while the electrons cannot.[131] Compared to heat engines, by directly converting the chemical energy into work and avoiding the thermal energy step, fuel cells are not limited by the Carnot's theorem thus they can have a much higher theoretical energy converting efficiency which exceeds the Carnot limit.[130] Aside from the high efficiency, fuel cells produce only water (if hydrogen is the fuel) as the oxidation product with low to zero CO_2 emissions, which also makes them a much greener choice as energy-conversion devices for mobile, stationary, and portable power.[132]

Fuel cells are categorized by their electrolyte types. Some commonly used/studied fuel cells are: alkaline fuel cell (AFC), direct methanol fuel cell (DMFC), proton exchange membrane fuel cell (PEMFC or polymer electrolyte membrane fuel cell), phosphoric acid fuel cell (PAFC), solid oxide fuel cell (SOFC), and molten carbonate fuel cell (MCFC).[121, 132] The latter two operate at high temperatures (500 – 1000 °C) and offer advantages for stationary power generation applications with high efficiency. While the other types are low-temperature fuel cells which attract more attentions in transportation and small portable power source applications.[121]

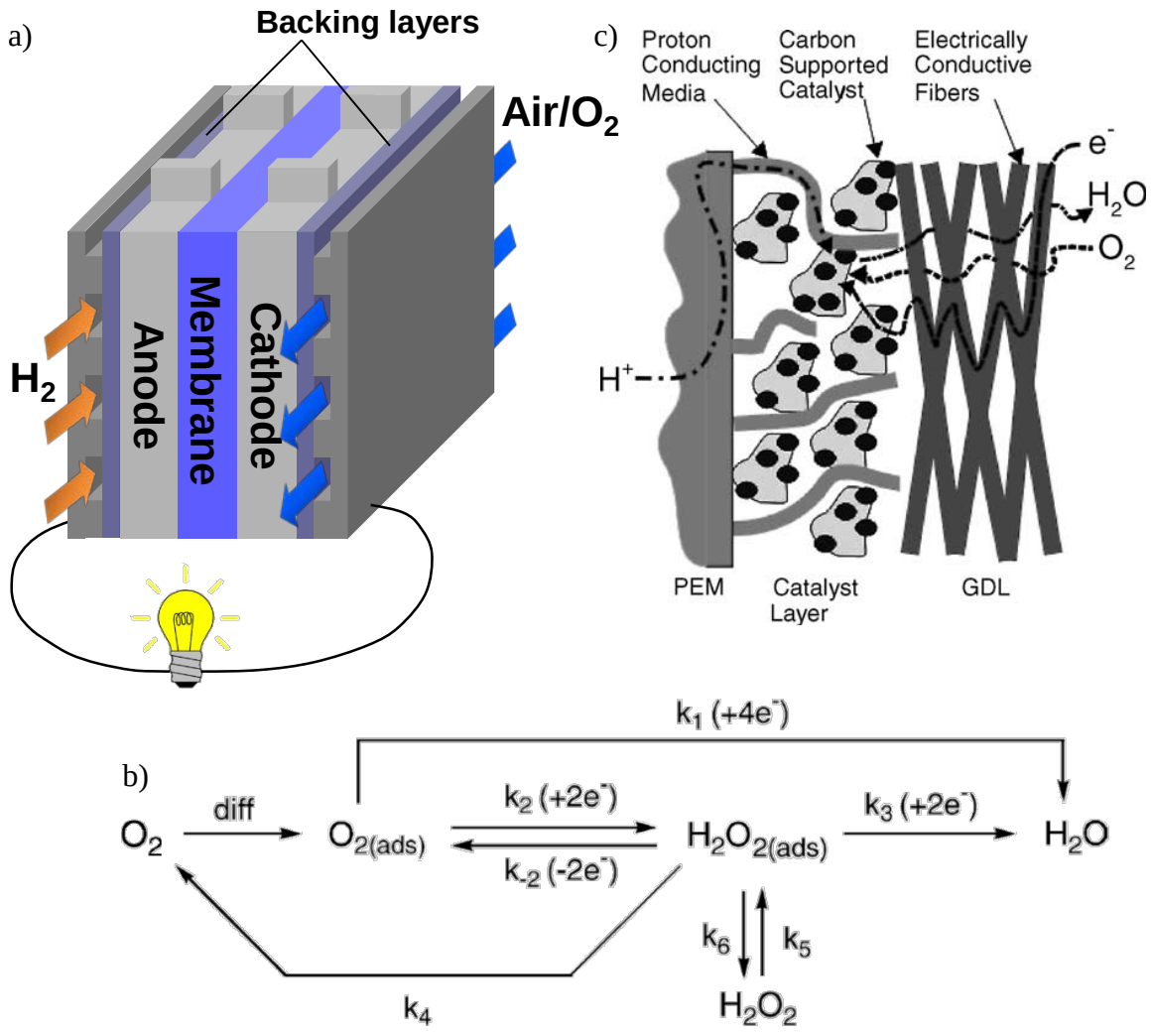

Figure 1-4. Schemes illustrating a) a simplified PEMFC; b) possible reaction processes for oxygen reduction reaction (ORR), adapted from ref 133; c) a close-up of the cathode, adapted from ref 131.

1.2.1.2 Oxygen Reduction Reaction

All low-temperature fuel cells share the same cathode reaction – oxygen reduction reaction (ORR). However, the slow ORR kinetics at the cathode is among the most limiting factors that affects the energy conversion efficiency of low-temperature fuel cells.[133] The ORR can proceed through two different pathways: (i) a four electron reduction process to directly produce water as the product; (ii) a less efficient two-step pathway, where hydrogen peroxide is formed via a two-

electron reduction process as the intermediate product and then subsequently reduced to water by another two-electron reduction process (Figure 1-3b). Platinum-based catalysts are currently the most active materials for low-temperature fuel cells.[132] However the expensive cost, limited abundance in earth crust, relative poor stability and short life time during operation severely limits the broad commercialization of fuel cells.[130]

One direction to solve the issue of Pt based catalyst at fuel cell cathode is to reduce the loading of expensive Pt. It could be achieved by either using alloys[134-135] or manipulating the morphology of Pt[136-137] or optimization of the catalyst support.[115, 138] Catalyst support plays a crucial role in conducting electricity, stabilizing metal catalyst particles, and facilitating mass transport during the fuel cell operation (Figure 1-3c).[131] Compared to common carbon black support, CNTs offer great opportunities due to their high conductivity, high specific surface area and better chemical resistance in both acidic and basic media against corrosion.[104]

Another more thorough yet less mature method is to completely replace the Pt-based catalysts with non-precious-metal catalysts, such as transition metal chalcogenides,[139] heat treated transition metal nitrogen containing complexes (macrocyclic complexes),[140] enzymatic electrocatalytic systems[141] or conducting polymer membrane.[142] Specifically, nitrogen containing transition metal complexes[98] or nitrogen-doped carbon nanomaterials[30] demonstrated great potential as ORR catalysts with additional advantages such as insensitive to CO poison and methanol cross-over effect[143] compared to traditional Pt-based ORR catalysts.

1.2.1.3 Nitrogen-doped Carbon Nanomaterials for ORR

Almost half a century ago Jasinski reported for the first time the ORR activity of transition metal porphyrins and phthalocyanines.[144] Recently, following Dai's discovery in 2009 of the excellent ORR catalytic activity of vertically-aligned nitrogen-doped carbon nanotubes synthesized from

the pyrolysis of iron phthalocyanine,[30] numerous efforts have been devoted to the study of nitrogen-doped carbon nanomaterials for ORR.[145-149] These nanomaterials have been demonstrated to have low over-potential, comparable to or even better than commercial Pt-carbon black catalyst. Other great advantages of such non-precious metal catalysts are their excellent long-term stability as well as their insensitivity towards CO poisoning and methanol cross-over effect.

On the other hand, the origin of such improved ORR catalytic activity compared to un-doped materials is also of great interest to the scientific society. A number of experimental and theoretical studies have been done trying to elucidate the origins of the catalytic activity and to obtain in-depth understanding on the structure-property relationship of the material. In Dai's original paper[30] and following work on polyelectrolyte-functionalized graphene[150] and carbon nanotubes,[151] the ORR activity was attributed to the high positively charged C atoms, which could effectively bind O_2 through a side-on configuration. Such positive charge on C atoms was either due to the strong electronic affinity of doped N atoms or from an intermolecular charge-transfer with a nitrogen-containing electron acceptor poly(diallyldimethylammonium chloride) (PDDA).[30, 150-151] However, further studies showed conflicting results when trying to correlate the ORR activity to specific nitrogen functionalities (pyridinic, pyrrolic or graphitic N, as discussed in Section 1.1.3.2). Theoretical calculations showed that graphitic N atoms decrease the energy barrier more efficiently than pyridinic N,[152] and are selective towards four electron reduction.[95] And this is consistent with experimental results on nitrogen-doped graphene[91] or mesoporous graphitic arrays.[153] On the contrary, other research has also found that pyridinic N atoms are the main active sites for ORR. Rao's study on vertical aligned nitrogen-doped CNTs showed that the electrocatalytic activity for ORR increases with the pyridinic-type nitrogen

functionalities,[154] while Anderson demonstrated theoretical calculations for ORR at pyridinic N edge sites.[155] However, as pyridinic nitrogen preferentially terminated at the edge of graphitic surface,[89-90] there is still another possibility that the ORR activity is merely enhanced by the higher active surface area, which naturally leads to the observed higher pyridinic N concentration. The abovementioned conflicting results may be due to the limited number of studies in the field and the variation in experimental conditions, especially the XPS peak assignment for different nitrogen functionalities as we discussed in the previous section.[156] Moreover, it is also possible that both graphitic N and pyridinic N participate in ORR. Ruoff's study on graphene and polymer functionalized graphene annealed in NH_3 demonstrated that the graphitic N content determined the limiting current density, while the pyridinic N content improved the onset potential for ORR.[157] And such conclusion was also supported by Wågberg's research on nitrogen-doped carbon nanotubes.[158]

Another controversial topic on the mechanism of ORR using nitrogen-doped carbon nanomaterials is the role of metal, which either presented as the catalyst for the synthesis of nitrogen-doped carbon nanomaterials or added into the structure deliberately. Although absolute metal-free nitrogen-doped carbon nanomaterials have been obtained and demonstrated improved ORR activities,[143, 150, 159-161] transition-metal-containing structures have shown excellent ORR catalytic activities[98, 162-165]. There are mainly two explanations for the roles of metal: (i) metals are not the active center but rather facilitate the incorporation of nitrogen into graphitic structure to form defect/edge sites, increasing the density of N/C active centers which are truly responsible for ORR;[96, 166-168] (ii) metals, possibly together with the N/C sites are the active center. In the latter case, transition metals can be either in the form of nanoparticles[169-170](such as Fe nanoparticle - nitrogen-doped graphene composite[169] and 3D nitrogen-doped graphene aerogel-

supported Fe_3O_4 nanoparticle[170]) or metal-nitrogen-carbon complex structures (such as metalloporphyrin or Fe-$N_{4)}$.[140, 171-172] It would be worth mentioning here that more recently direct HRTEM and EELS imaging results were obtained by Dai et al which established a close spatial relation between iron and nitrogen atoms.[172] Together with electrochemical testing, especially a KCN passivation comparison, their results strongly suggested Fe-porphyrin-like active sites are responsible for the enhanced ORR activity.

1.2.1.4 Other Heteroatom-doped and Binary/Ternary doped Carbon Nanomaterials for ORR

The attracting performance of nitrogen-doped carbon nanomaterials has triggered investigation into other heteroatom-doped carbon nanomaterials for ORR. Boron[173-174] and phosphorus,[175-176] which both have smaller electronegativity than carbon as opposed to nitrogen (which has larger electronegativity than carbon), were all successfully doped into carbon nanomaterials and achieved enhanced ORR activity. Due to the difference in electronegativity, it was suggested that breaking the electroneutrality of graphitic materials to create charged sites favorable for O_2 adsorption is a key factor in enhancing ORR activity, regardless of whether the dopants are N or B atoms.[174] However, the discovery of the improved ORR performance of sulfur[177-178] and selenium[179] doped structures might suggest different mechanism since both S and Se have similar electronegativity to carbon. It was suggested that tailoring the π electronic system of graphitic structure, either by the effect of electronegativity or by the conjugation of lone pair electrons with the π system may be a preferred factor.

More recently, as the individual heteroatom-doped carbon nanomaterials demonstrated promising ORR activity, research progressed to include materials doped with two or multiple heteroatoms. Boron with nitrogen,[180-185] phosphorous with nitrogen,[185-186] sulfur with nitrogen[187]

as well as ternary (N, B, P)[188] doped carbon nanomaterials for ORR have been reported. Such research effort on binary and ternary doping not only creates new structures for ORR, some even in acidic media[184-185], but also provides some deeper understanding on the ORR mechanism. Hu et al has found that for boron and nitrogen co-doped carbon nanotubes, when B and N atoms are bonded together, they can hardly break the inertness of CNTs; while when B and N atoms are separated, one can turn CNTs into excellent ORR electrocatalysts.[181] Furthermore, studies on (B,N),[182, 185] (P,N)[185] and (S,N)[187] co-doping suggested that both the charge density and spin density of the dopant atoms can affect the catalytic activity of the resulting nanomaterials, while the latter plays a more important role than the former.[189-190]

1.2.1.5 Limitation and Prospects for Nitrogen-doped Carbon Nanomaterials for ORR

Nitrogen-doped carbon nanomaterials have attracted considerable attention as potential low-cost replacement for fuel cell cathode catalysts in recent years. However, there are still problems as well as great opportunities. First, from the materials science point of view, the controllable synthesis of nitrogen-doped carbon nanomaterials with well-defined structure and with specific nitrogen functional groups is far from satisfactory. Such inhomogeneity of the samples is possibly the common issue for most carbon-based nanomaterials. This lack of control on the structure of the materials results in the second problem on the chemistry side: the mechanism of the enhanced ORR activity is still not quite clear. Although efforts have been made to investigate the correlation between the detailed functionalities of nitrogen species (and other heteroatom species), the metal catalyst residues and the ORR performance, conflicting results are often reported. Such lack of an in-depth understanding on the detailed ORR mechanism would be a barrier for future design and engineering of better nitrogen-doped carbon nanomaterials as fuel cell catalysts. From the application point of view, a third issue for nitrogen-doped (or

heteroatoms-doped) carbon nanomaterials is their applicability in acidic media. Most of the research right now still focuses on their performance in basic media, which avoids the protonation problem of the nitrogen sites. However, most low temperature fuel cells, especially proton exchange membrane fuel cells (or polymer electrolyte membrane fuel cells, PEMFC) usually require acidic electrolytes. Thus it is necessary to further develop nitrogen-doped carbon nanomaterials which could retain their activity and stability for ORR in acidic environment.

In this dissertation, major effort would be placed on the synthesis of a novel material - nitrogen-doped carbon nanotube cups – and the study of their ORR activity, as well as the effect of metal catalyst residue and nitrogen doping on the catalytic activity.

1.2.2 Electrochemical Sensors and Biosensors

Electrochemical sensors and biosensors are analytical devices that convert an electrochemical or biological response into a quantifiable and processable signal, typically in the form of the measurement of some electrical parameters (Figure 1-4a).[5, 191] Its key component is a recognition element and a transducer device that produces a signal with selectivity towards a particular analyte or a group of analytes, thus minimizing interferences from other species in the sample.[9] Other components include an electronic system that collects, amplifies, and displays the signal.[191]

Typically electrochemical sensors/biosensors can be divided in to several categories based on their sensing mechanism. Commonly used types are: (i) amperometric, which is based on the current measurement; (ii) potentiometric, which is based on the measurement of potential or charge accumulation; (iii) conductometric, which is based on the change of conductive properties of a medium between electrodes.[5, 191] Other modern types of electrochemical

sensor/biosensor are also being developed such as impedimetric sensors which measure the impedance through the electrode, and field-effect transistor sensors which use transistor technology to measure the source-drain current as a result of a changing of gate voltage.[191]

The era of electrochemical biosensors began in 1962 with the introduction of the first glucose biosensor based on glucose oxidase (GOx) by Clark and Lyons.[192] Half a century later, while diabetes remains as a worldwide public health problem, millions of diabetics monitor their blood glucose levels daily to ensure it remains in the normal range of 80-120 mg/dL (4.4-6.6 mM).[193] And glucose monitors are the most widely used biosensors which account for about 85% of the entire biosensor market and are still attracting tremendous attention due to the increasing demand on reliable devices for diabetes control.[193-194]

The detection of glucose concentration is achieved through the amperometric type electrochemical sensors. There are three generations of glucose biosensors based on the different mechanisms of electron transfer during the glucose oxidation on GOx (Figure 1-4b). The first generation is based on the use of the natural oxygen co-substrate and generation and detection of hydrogen peroxide.[195-196] The second generation is based on artificial redox mediators such as ferrocene derivatives,[197] or modification of GOx[198] and the linkage to the electrode.[199] And the third generation is based on direct electron transfer between GOx and the electrode.[200-201]

On the other hand, hydrogen peroxide is another analyte of great interest to many fields and particularly in electrochemical sensing/biosensing because it is released during the oxidation of the substrate by a pertinent oxidoreductase in the presence of oxygen and is related to various bio-processes.[202]

Carbon nanotubes and graphene are promising materials for electrochemical sensors/biosensors with good selectivity, fast response and high sensitivity.[10, 203] Compared to

conventional macroscopic materials, they offer significant advantages such as their good electrical and electrochemical properties, high chemical stability, and also the ability to mediate electron transfer when used as the electrode material.[7, 120, 204] Their unique 1D or 2D nanometer-sized structure also allows them to be used as nanometer-size electrodes,[6, 205-206] which might achieve the recognition of single biomolecule events.[207] There are tremendous effort and passion people devoted to the fabrication of CNTs and graphene-based electrochemical sensors/biosensors; we were also interested in the differences between CNTs and graphene, given the fact that they have identical composition but rather significant differences in dimensions. Understanding of the similarity and differences by comparison of such ideal 1D and 2D structures would be able to provide more insight of the structure-property relationship of carbon nanomaterials and also help further improving the performance of graphene and CNTs based electrochemical sensors/biosensors.

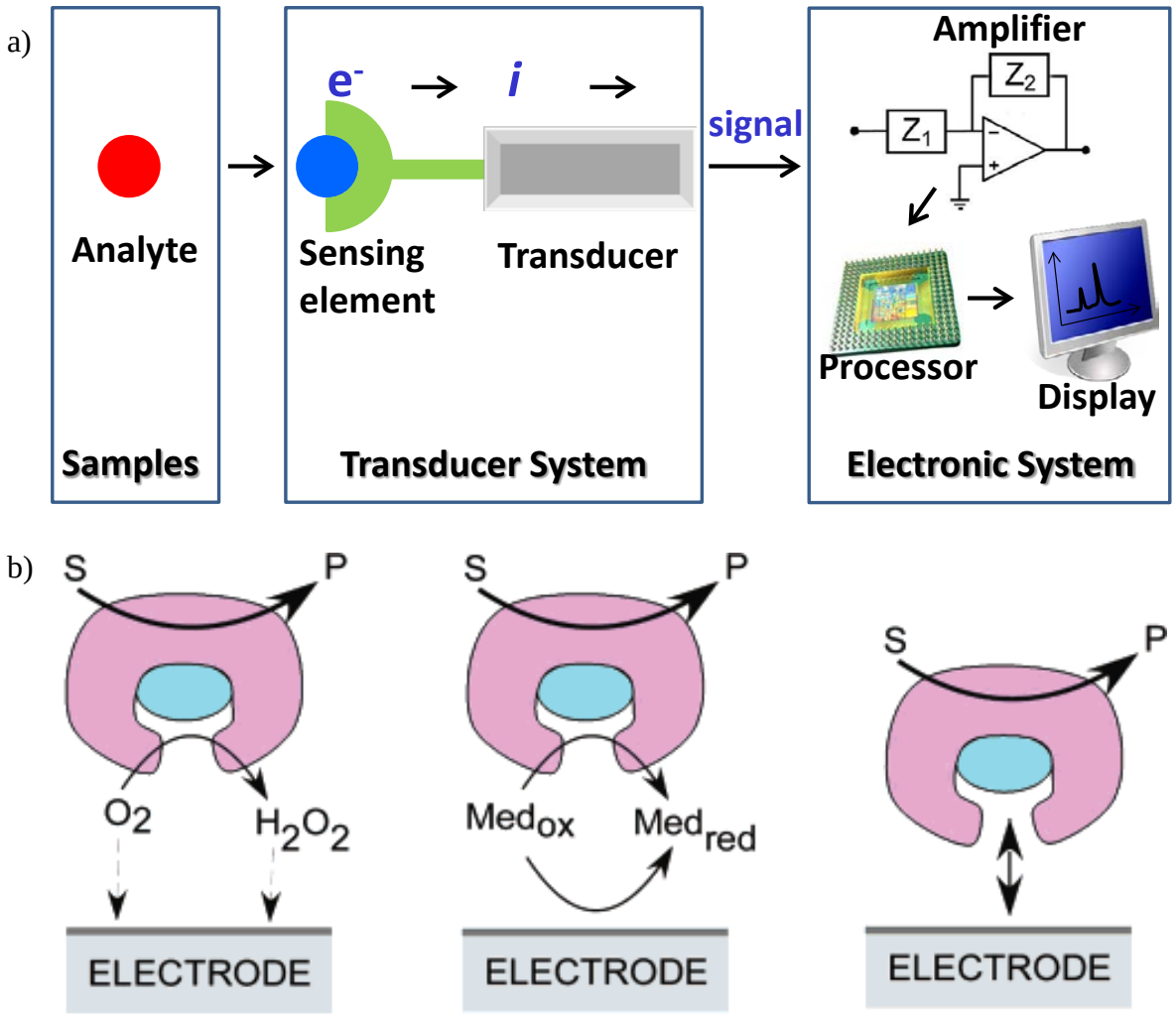

Figure 1-5. a) schematic illustration of the structure of an electrochemical sensor/biosensor; b) Three generations of amperometric enzyme electrodes for glucose based on the use of: left - natural oxygen cofactor, middle - artificial redox mediators, right - direct electron transfer between GOx and the electrode; adapted from reference 193.

2.0 ELECTROCHEMICAL DETECTION WITH PLATINUM DECORATED CARBON NANOMATERIALS

2.1 CHAPTER PREFACE

The aim of this work was to investigate the structure-property relationship between 1D nanomaterial and 2D nanomaterial as the sensing platform. Specifically, hybrid structures of Pt Pt nanoparticles (NPs) with both single-walled carbon nanotubes (SWNTs) and graphene were synthesized as the sensing material, and characterized for the detection of hydrogen peroxide using various electrochemical techniques.

Here we performed amperometric detection of hydrogen peroxide (H_2O_2) using single-walled carbon nanotubes (SWNTs), chemically converted graphene (CCG) and sulfonated CCG (CCG-S) decorated with Pt nanoparticles (NPs). Although all three systems demonstrated similar detection limits for H_2O_2, compared to the other two nanomaterials, Pt-SWNTs provided a higher sensitivity with only half of the Pt amount. This result was consistent with cyclic voltammetry, electrochemical impedance spectroscopy, and field-effect transistor measurements. We attribute the higher sensitivity of Pt-SWNTs to both the surface roughness of the electrode and the intimate contact between Pt NPs and one-dimensional nanostructures (SWNTs) versus two-dimensional nanostructures (graphene).

The material contained in this chapter was published as a research paper in the journal *Electroanalysis* and have been reprinted (adapted) with permission from *Electroanalysis* **2011,** *23*, 870-877 under license number 3165201501640, Copyright © 2011 WILEY-VCH Verlag GmbH & Co. KGaA, Weinheim. The full citation is listed as reference [208] in the bibliography section.

List of Authors: Yifan Tang, Gregg P. Kotchey, Harindra Vedala and Alexander Star

Author contributions: All authors contributed to the design of experiments and writing of the paper. Chemically converted graphene (CCG) synthesis and FT-IR characterization were performed by GPK. Sulfonated CCG was synthesized by GPK and YT. Field effect transistor fabrication and measures were performed by HV. YT synthesized the Pt-SWNTs, Pt-CCG, Pt-CCGs materials, performed the electron microscopy, EDX spectroscopy and electrochemical characterizations.

2.2 INTRODUCTION

Over the past decade, one-dimensional (1-D) carbon nanotubes have epitomized the utility of carbon nanomaterials for both electronic[8, 21, 127, 209] and electrochemical[14, 31, 203, 210] sensor-based applications. Beginning in 2004,[37] a new two-dimensional (2-D) carbon nanomaterial, graphene, has excited the scientific community. Graphene is a one-atom-thick flat sheet of carbon atoms tightly packed into a 2D honeycomb lattice.[1] It possesses unique electronic properties[1] and

mechanical strength,[38] which may make graphene ideal for integration in electronics, batteries, sensors, and composites.[1, 42, 211-212] While the field of sensing employing graphene is far from maturation, steady progress has been made in terms of both electronic[212] and electrochemical[10, 40] sensors.

Since 2004,[202] single-walled carbon nanotubes (SWNTs) decorated with Pt nanoparticles (NPs) have been studied for the detection of hydrogen peroxide (H_2O_2), which is one of the most important medically relevant analytes in the biosensing area.[193, 202] The combination of the zero-dimensional (0-D) and 1-D nanostructures provided good selectivity, a low detection limit, and a large dynamic range for the detection of H_2O_2. Recently, after large quantities of graphene became available through improved production methods[213] such as chemical exfoliation/ reduction, considerable investigation of the graphene systems has been undertaken following a pattern of research similar to CNTs. Therefore, like SWNTs, graphene decorated with Pt NPs has been also studied for H_2O_2 detection;[117-118] a detailed comparison between Pt-SWNT and Pt-graphene for the electrochemical detection of H_2O_2, however, was not performed. In this work, we conducted a systematic study of SWNTs, chemically converted graphene (CCG), and sulfonated CCG (CCG-S), which were all decorated with Pt NP catalysts for the electrochemical detection of H_2O_2. After being modified on a glassy carbon electrode, all three systems demonstrated comparable electrochemical detection limits for H_2O_2; Pt-SWNTs, however, exhibited a higher sensitivity than Pt-CCG and Pt-CCG-S. In addition to the amperometric measurements, we have performed cyclic voltammetry, electrochemical impedance spectroscopy, and field-effect transistor (FET) measurements to characterize these three catalytic systems. From our experimental results, we hypothesized that both the surface roughness of the electrode

and the intimate contact between Pt NPs and 1-D nanostructures (SWNTs) versus 2-D nanostructures (graphene) could be attributed to the higher sensitivity of Pt-SWNT.

2.3 EXPERIMENTAL SECTION

2.3.1 Material synthesis

Graphite oxide was prepared utilizing a modified Hummers' method on graphite flakes that underwent a preoxidation step.[214] Graphene oxide (GO) (~ 0.125 wt%) was subsequently formed from graphite oxide that was diluted 1:4 with double distilled water and exfoliated for 45 minutes by ultrasonication followed by 30 minutes of centrifugation at 3400 revolutions per minute (r.p.m.) to remove unexfoliated graphite oxide. GO was reduced to chemically converted graphene (CCG) by two different methods. In the first method, sulfonated CCG (CCG-S) was prepared following a published procedure.[215] The pH of a 75 g dispersion of GO in water was adjusted to approximately pH = 9 with sodium carbonate (Na_2CO_3), the GO was partially reduced through the addition of 600 mg of sodium borohydride ($NaBH_4$), and the mixture was kept at 80 °C for 1 hour under constant stirring. After four sequential washing/centrifugation cycles, the partially reduced GO was dispersed in water via mild sonication for a final mass of 75 g. The sulfonation step employed an aryl diazonium salt solution of sulfanilic acid. In 10 g of double distilled water, 46 mg of sulfanilic acid, 18 mg of sodium nitrite ($NaNO_2$), and 0.5 g of 1 M HCl solution were dissolved, and this solution was added to the dispersion of partially reduced graphene oxide. After the dispersion was stirred on an ice bath for two hours, the sulfonated/partially reduced GO was washed and dispersed in water for a final mass of 75 g.

Finally, to form CCG-S, the dispersion of sulfonated/partially reduced GO was reduced by hydrazine (N_2H_4). To this end, 4 g of 50 wt% hydrazine hydrate was added to the dispersion of sulfonated/partially reduced GO, which was subsequently refluxed at 100 °C for 24 hours under constant stirring, followed by washing with centrifugation. In the second method, CCG was synthesized by a procedure that mirrored the synthesis of CCG-S with the exclusion of the sulfonation step; therefore, GO was reduced with $NaBH_4$ followed by N_2H_4 reduction.

SWNTs (P2-SWNT, Carbon Solutions, Inc.), CCG, and CCG-S were decorated with Pt NPs by chemical reduction following a published procedure.[216] About 5 mg of H_2PtCl_6 was dissolved in 1.2 mg of double distilled water, and the pH value of the solution was subsequently adjusted to pH = 7 using 5% Na_2CO_3 solution. SWNTs, CCG, or CCG-S (5 mg) were dissolved in 5 mL of double distilled water via sonication followed by mixing with H_2PtCl_6 solution. The measured pH of the solution was adjusted to neutral using 5% Na_2CO_3 solution. The surfactant N-Dodecyl-N,N-dimethyl-3-ammonio-1-propanesulfonate (SB12) (5 mg) was dissolved in 2.5 mL of methanol. The reduction of H_2PtCl_6 was accomplished by heating the dispersion of carbon nanomaterials and H_2PtCl_6 in a water bath at 80 °C under constant stirring while adding the SB12/methanol solution drop-wise. After the addition, the dispersion was kept at 80 °C for 1 hr. The resulting Pt NP decorated nanomaterials were washed thoroughly with double distilled water and ethanol for three times each and finally dried under vacuum.

2.3.2 Characterization

To confirm sulfonation, Fourier transform infrared (FTIR) spectroscopy was implemented. CCG-S and CCG were isolated using TefSep Teflon laminated filters (0.22 μm hole size). Each sample was mixed with KBr and ground into a fine powder using a mortar and pestle. A KBr

pellet was formed from the powder using a press, and the transmittance spectrum of the pellet was taken employing an Avatar 360 FTIR. In contrast to CCG, CCG-S demonstrated unique peaks at 1165 cm^{-1} and 1122 cm^{-1} that corresponded to presence of S–O bond ($\nu_{S\text{-}O}$).

For the transmission electron microscopy (TEM) imaging, 10 μL of suspended Pt-SWNTs, Pt-CCG, or Pt-CCG-S were placed on a lacey carbon grid (Pacific-Grid Tech) and allowed to dry under ambient conditions for 2 hours prior to TEM imaging (FEI Morgagni, 80 keV or JEOL 2100F, 200 keV).

Scanning electron microscopy (SEM) and energy-dispersive X-ray (EDX) spectroscopy were performed with a Phillips XL30 FEG microscope equipped with an EDAX assembly at 10 keV.

2.3.3 Electrode Preparation

A glassy carbon (GC) electrode (CHI 104, GC area 0.0707cm^2, total area 0.196 cm^2) was carefully polished with gamma alumina powder (0.05 micron, CH Instruments) until a mirror finish was obtained. Then the electrode was sonicated and rinsed with plenty of double distilled water to remove any alumina residues, and dried in air. Catalyst ink was made by dissolving 1 mg of Pt-SWNTs, Pt-CCG or Pt-CCG-S in a mixture of 1 mL of ethanol and 8 μL of 5% Nafion by sonication for 30 minutes to give a concentration of 1 mg/mL and 0.04% Nafion. 20 μL of catalyst ink was then dropcasted on the GC electrode surface and allowed to dry in the air.

2.3.4 Electrochemical characterization.

Cyclic voltammetry (CV), amperometric measurements, and electrochemical impedance spectroscopy (EIS) were performed using CHI 7042 Potentiostat (CH Instruments, Austin, TX). A typical three electrode system was used with the Pt-SWNT, Pt- CCG or Pt-CCG-S modified GC electrode as the working electrode, a Pt-wire (CHI 115) as the counter electrode, and a Ag/AgCl electrode (CHI 111, 1M KCl) as the reference electrode. All potentials are reported versus the reference electrode.

The hydrogen evolution reaction was tested in N_2 saturated 0.5 M H_2SO_4 solution. Continuous scans were performed until the resulting CV curves were stable. H_2O_2 detection was implemented in N_2 saturated 50 mM PBS after the solution with the working electrode held at +0.5 V. EIS was also conducted in N_2 saturated 50 mM PBS with a DC at +0.5 V and AC excitation signal at 10 mV. The spectra were recorded in the frequency range of 0.1 Hz to 10^5 Hz.

SWNT or graphene field-effect transistor (FET) devices were fabricated by patterning interdigitated microelectrodes (source-drain spacing of 5 μm) on top of a 200 nm oxide layer on Si substrates using photolithography and e-beam evaporation of 30 nm Ti and 100 nm of Au. SWNTs or graphene were used as conducting channels in these FETs. The alternating current dielectrophoresis (DEP) technique was used for selective deposition of SWNT networks from a *N*,*N*-dimethylformamide (DMF) suspension onto each interdigitated microelectrodes pattern.[217] The dielectrophoresis parameters namely AC frequency (10MHz), bias voltage (8 V_{pp}) and bias duration (60 s) were used to yield SWNT network devices (NTFET) with similar electrical conductance (0.01 – 1 mS). Applying a frequency (300 kHz), bias voltage (8 V_{pp}) and bias duration (120 – 240 s) yielded CCG and CCG-S devices with similar electrical conductance from

a suspension in water. Platinum decorated SWNT, CCG and CCG-S samples were obtained in ethanol solution, and the device fabrication procedure was similar to that of bare devices. Each Si chip comprising of multiple FET devices was then placed onto a standard ceramic dual in-line package (CERDIP) and wirebonded. Two Keithley 2400 sourcemeters were used for FET measurements. The electrical performance of each device was investigated employing an electrolyte gated FET device configuration, where the conductance of the NTFET device was tuned using the electrolyte as a highly effective gate. To this end, a small fluid chamber (1 mL) was placed over the NTFET device to control the liquid environment using phosphate buffer saline (PBS) (20μM) at pH 7. A liquid gate potential (− 0.75 V to + 0.75 V) with respect to the grounded drain electrode was applied using an Ag/AgCl (3 M KCl) reference electrode submerged in the electrolyte. The drain current of the device was measured at a constant source-drain voltage of 50 mV. Transfer characteristics (i.e., conductance (G) versus gate voltage (V_g)) of the bare and Pt NPs decorated samples were measured to investigate the effect of Pt nanoparticle decoration on transport properties.

2.4 RESULTS AND DISCUSSION

Pt-SWNT, Pt-CCG, and Pt-CCG-S nanomaterials were prepared following published procedure[216] and were characterized using TEM and FTIR. The FTIR data confirmed that bare CCG-S was successfully functionalized with sulfonic groups during the sulfonation step. Si *et al.* demonstrated[215] that with a zeta potential between –60 to –70 mV, CCG-S was well dispersed in water as a result of the sulfonic groups. After platinum decoration, Pt-CCG-S, in large part, remained dispersed in water (Figure 2-1C inset); this is in contrast to Pt-CCG and Pt-SWNTs,

which had a tendency to aggregate (Figure 2-1A and B inset). The TEM micrographs indicated that the Pt-SWNTs existed as bundles with diameters ranging from 50 to 100 nm and were decorated with Pt nanoparticles of approximately 4 to 6 nm in diameter (Figure 2-1A). Pt-CCG and Pt-CCG-S had flakes of comparable dimensions (0.5 to 1.5 μm), and both were uniformly decorated with Pt nanoparticles that were approximately 4 to 6 nm in size (Figure 2-1B, C).

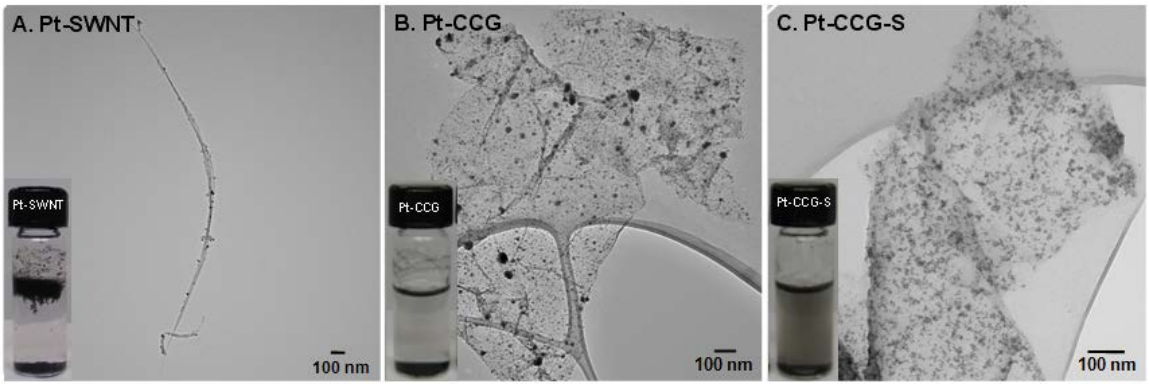

Figure 2-1. Transmission electron microscopy (TEM) images of A) Pt-SWNT, B) Pt-CCG and C) Pt-CCG-S. Insets: Optical images showing the materials dispersed in water by sonication. Compared to Pt-SWNT and Pt-CCG, the Pt-CCG-S suspension showed negligible precipitation after 24 hrs.

We prepared GC electrodes modified with all three nano-materials. Figure 2 shows the SEM images for all three catalyst materials on the elecotrodes surfaces. The Pt-SWNT electrode surface showed a porous morphology with the bundles of SWNTs forming networks (Figure 2-2A). The surface of the Pt-CCG modified electrode (Figure 2-2B) also had higher surface roughness and had more edge structures than that of Pt-CCG-S (Figure 2-2C). This would result in more available edge planes for CCG, which has faster electrode kinetics than the basal planes.[218] The smooth surface of Pt-CCG-S could be attributed to the highly dispersed nature of the catalyst ink during the drying process. While the enhanced dispersibility of CCG-S might be

desirable for chemical functionalization during solution processing, the resulting denser catalyst layer may not be favored in electrochemical application since the surface area of the catalyst becomes less accessable.

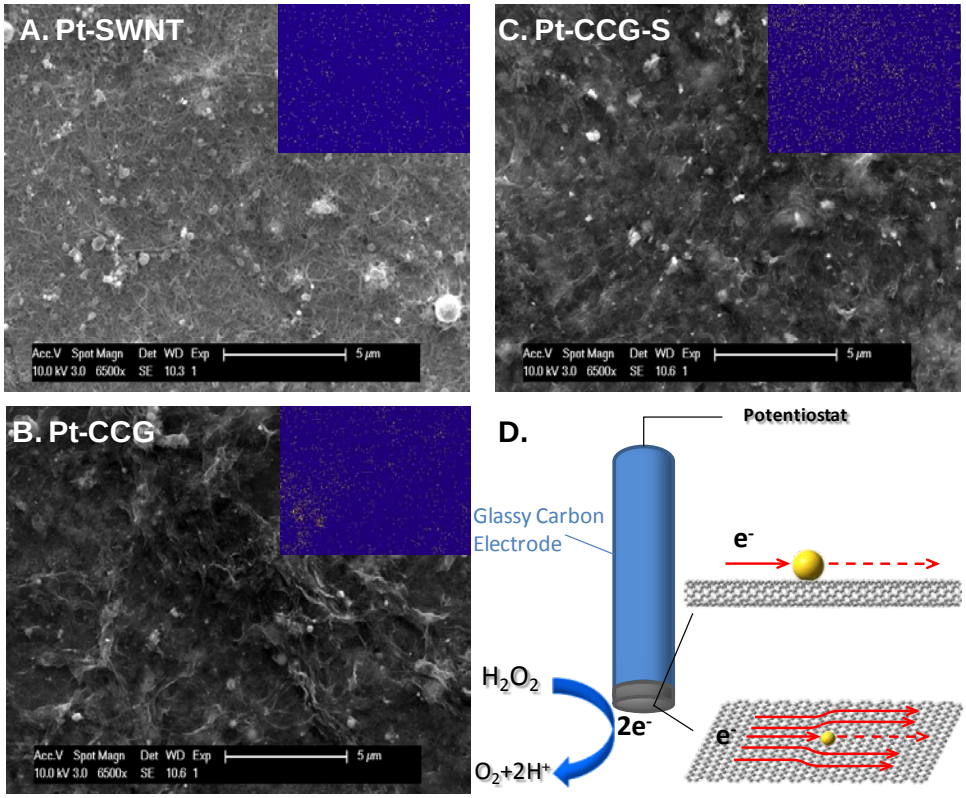

Figure 2-2. Scanning electron microscopy (SEM) images of A) Pt-SWNT, B) Pt-CCG and C) Pt-CCG-S. Inset figures show the Pt distribution measured using energy-dispersive X-ray (EDX) spectroscopy; D) Schematic illustration for H_2O_2 electrochemical detection at modified glassy carbon electrode showing Pt NP having larger effect on the electrical conductivity through 1-D SWNT than 2-D graphene nanostructure.

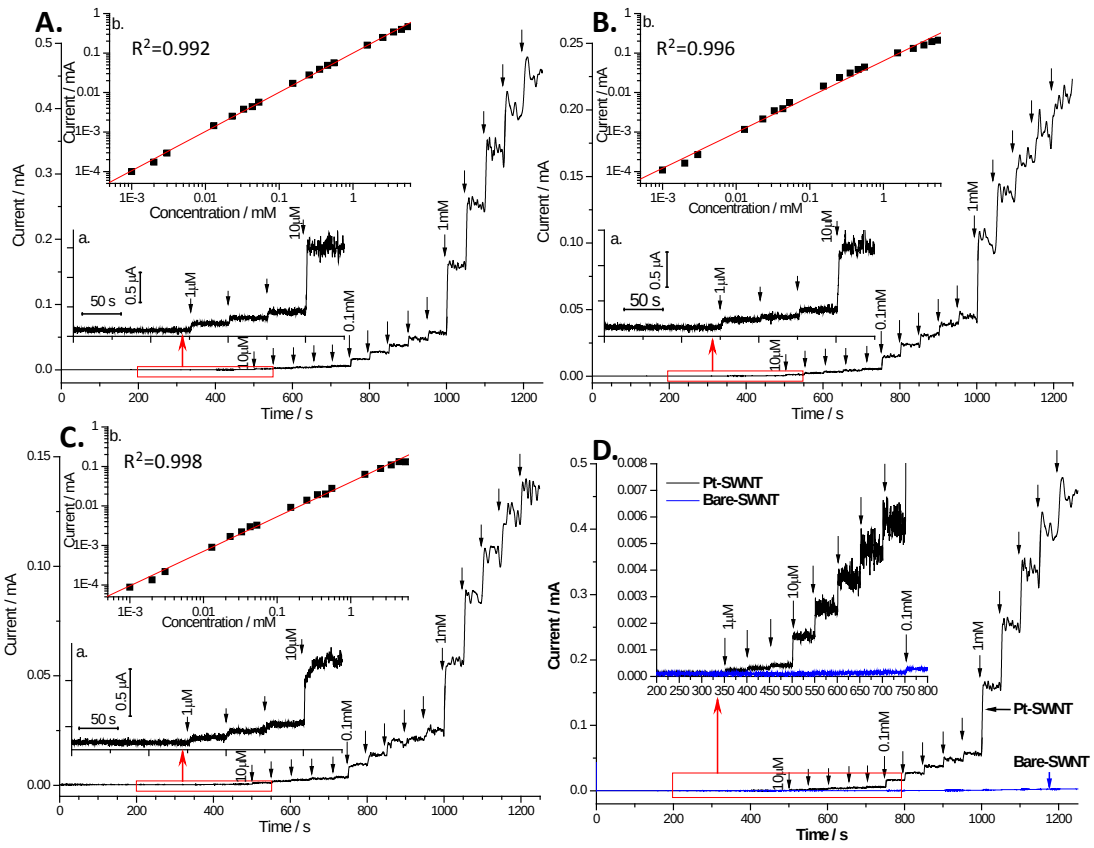

Figure 2-3. Amperometric response of A) Pt-SWNT, B) Pt-CCG and C) Pt-CCG-S catalysts modified glassy carbon (GC) electrodes towards successive addition of H_2O_2 (indicated by arrows with marked concentrations) to 50 mM PBS (pH = 7.2) at + 0.50 V (vs Ag/AgCl). Inset of each panel: a: Amplification of current-time curve marked out in red square (time from 200 s to 550 s). b: Calibration curve for H_2O_2 detection. D) Comparison of amperometric response for Pt-SWNT vs. bare SWNT. Inset: Amplification of current-time curve marked out in red square.

All three nanomaterials demonstrated comparable performance towards the oxidation of H_2O_2 as reported in the literature.[117-118, 202] The amperometric response of each catalyst towards successive addition of H_2O_2 (indicated by arrows with marked concentrations) in 50 mM PBS (pH = 7.2) and +0.50 V is depicted in Figure 2-3. A linear relationship between H_2O_2 concentration and current was observed for the concentration range from 1 μM to about 5 mM with R^2 value that ranged from 0.992 to 0.998. For H_2O_2 concentrations above 5 mM, the signal

became saturated, and the calibration curve deviated from linearity. All three nanomaterials had comparable detection limits of around 0.15 μM, which was almost three orders lower than the detection limit of bare SWNTs (around 0.1 mM, Figure 3D). This suggests that even though we cannot completely rule out the effect of iron-based impurities in SWNTs for its peroxide behavior,[97] Pt NPs and their interaction with SWNTs or graphenes were primarily responsible for the H_2O_2 sensitivity in our experiment. However, it should be emphasized that half as much Pt was used in Pt-SWNT (10 wt %) compared to Pt-CCG (21 wt %) and Pt-CCG-S (27 wt %) (Table 2-1). Also, Pt-SWNT had the highest slope (0.992) for the H_2O_2 detection calibration curve followed by Pt-CCG (0.907) (Table 2-1). This indicated a higher current response towards the same analyte concentration, which translated into higher signal for sensor application.

Table 2-1. Data summary for Pt-SWNT, Pt-CCG, Pt-CCG-S

	Pt wt %[a]	ECSA m^2/g_{Pt}[b]	H_2O_2 Calibration Curve Slope[c]	Charge Transfer Resistance /Ω[d]
Pt-SWNT	10	111	0.992	87.2
Pt-CCG	21	100	0.907	130.7
Pt-CCG-S	27	53	0.875	162.7

a. The weight % of Pt is calculated from EDX data; b. The electro-chemical surface area (ECSA) is calculated from CVs in Figure 4A; c. The H_2O_2 calibration curve slope is calculated from the amperometric response in Figure 3. d. The charge transfer resistance is obtained by fitting the EIS data in Figure 4B to the equivalent circuit shown in the inset.

This difference in sensor performance between Pt-SWNT, Pt-CCG, and Pt-CCG-S can also be observed from the electrochemical surface area (ECSA) calculations (Table 2-1). ECSA

was calculated by first integrating the charge (area under the reverse CV scan) for the hydrogen evolution reaction (Figure 2-4A) from ~0.1 V to – 0.2 V and following the equation:[219]

$$\mathrm{ECSA}_{\mathrm{Pt,cat}}(\mathrm{m^2 g_{Pt}^{-1}}) = \left[\frac{Q_{H-dasorption}(\mathrm{C})}{210\,\mu\mathrm{C\,cm_{Pt}^{-2}} L_{Pt}(\mathrm{mg_{Pt}cm^{-2}}) A_g(cm^2)}\right] 10^5 \qquad (2\text{-}1)$$

Although Pt-SWNT had the lowest Pt weight percentage, this nanomaterial showed an ECSA that was 11% and 109% higher than Pt-CCG and Pt-CCG-S, respectively, which indicated that the Pt NPs on SWNT were more active and accessible to the electrolytes.

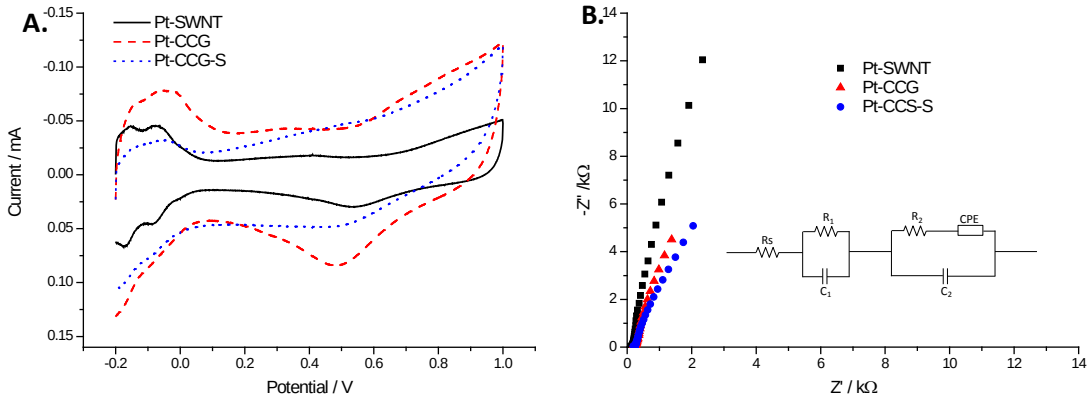

Figure 2-4. A) Cyclic voltammograms (CV) of Pt-SWNT (solid line), Pt-CCG (dashed line) and Pt-CCG-S (dot line) catalysts modified GC electrodes for hydrogen evolution reaction in N_2 purged 0.5 M H_2SO_4 solution; B) Impedance spectra of Pt-SWNT (squares), Pt-CCG (triangles) and Pt-CCG-S (circles) catalysts modified GC electrodes in 50 mM PBS (pH = 7.2) at DC=+0.50 V, AC=0.01V, 0.1 Hz~10^5 Hz. Inset: equivalent circuits for EIS data fitting.

Figure 2-4B showed the electrochemical impedance spectra (EIS) of all three catalyst materials conducted under the same conditions as the H_2O_2 detection. By fitting the EIS data to equivalent circuits (Figure 2-4B inset and Table 2-1), it was observed that Pt-SWNT showed the smallest charge transfer resistance (high frequency region, R_1) (87.2 Ω), followed by Pt-CCG (130.7 Ω), and Pt-CCG-S (162.7 Ω). This was consistent with the ECSA and amperometric measurements. The smaller charge transfer resistance indicates less opposition to the passage of

an electric current. This could be understood by looking at the schematic illustration in Figure 2D, where a 1-D system (Pt-SWNT) and a 2-D system (Pt-CCG or Pt-CCG-S) were compared. While the Pt NP would have intimate contact with both SWNT and graphene, the change in electrical conductance (either by electron or hole charge carriers) as a result of the NP on the 1-D system's surface would be more significant than on the 2-D system. In order to understand this mechanism, we studied the performance of these three systems in an electrolyte gated FET configuration since electrolyte-gated nanostructured FETs (SWNT and graphene) have demonstrated good electrical characteristics as thin top-gate insulators with high dielectric constants in ionic solutions.[128, 220-222]

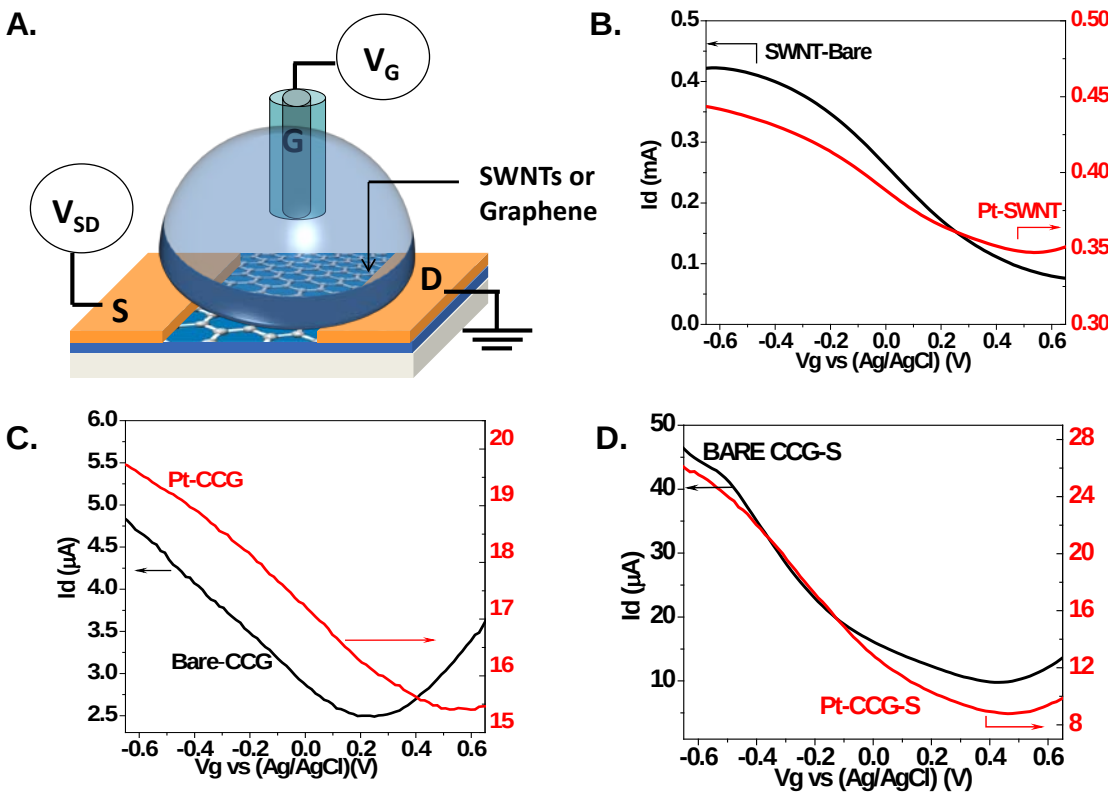

Figure 2-5. A) Schematic illustration of liquid gate FET setup for electrical characterization of SWNTs or graphene. Transfer characteristics of bare and platinum decorated B) SWNT, C) CCG, and D) CCG-S.

The illustration of the experimental setup used for electrolyte gated FET measurements is depicted in Figure 2-5A. Figure 2-5B, C, and D shows the transfer characteristics (i.e., conductance (G) versus gate voltage (V_g)) curves for SWNTs, CCG, and CCG-S respectively. Pristine SWNT network FETs exhibited a p-type behavior with an on/off ratio of around 10. The low on/off ratio of the SWNT can be attributed to the presence of metallic SWNT in the network. When SWNTs were decorated with Pt nanoparticles a decrease in gate modulation was observed with an on/off ratio of around 2.

For pristine CCG devices (Figure 2-5C), ambipolar characteristics were observed with the Dirac point at 0.2 V and the on/off ratio was around 2. In the case of Pt decorated CCG, a slight change in on/off ratio and a shift in the curve towards more positive gate voltage was observed. This indicated hole doping. For pristine CCG-S devices (Figure 2-5D), a p-type behavior was observed; the dominate hole transport may be attributed to the presence of sulfonic groups on the basal plane of the CCG-S. However, no significant change in on/off ratio or shift in the curve was observed for the CCG-S samples upon decoration with Pt nanoparticles. Since the pristine and Pt decorated FET devices were fabricated from different samples, for all the three structures (i.e. SWNT, CCG, CCG-S), a quantitative comparison between absolute values of conductance before and after Pt decoration was not possible. However it can be clearly observed that compared to graphene nanostructures, SWNT network FETs underwent significant change in transfer characteristics when decorated with Pt nanoparticles.

It has been reported that SWNT-supported metal nanoparticles experience charge redistribution, and the formation of a depletion layer surrounding the metal can create localized depletion regions in the semiconducting SWNT.[223-225] These charge depletion regions act as charge scattering sites that would act as pseudo-Schottky barriers. The result would be a change

in charge mobility through the SWNT network, which caused the observed tilt in the transfer characteristics of Pt NPs decorated SWNT devices (Figure 2-5B). However, such a tilt was not observed in graphene system, which might indicate that the scattering effect was localized near the Pt NPs and does not affect the charge transport in the basal plane of graphene-Pt system to the same degree. We believe that this large effect of the Pt NPs in Pt-SWNT manifested in its increased electrochemical performance. Also, it has been reported that different metals NPs, such as Ag, Au, Pd and Pt NPs, all showed significant effects on SWNTs' transfer characteristics.[223, 226] It is possible that other metal NPs would have different influences on the 1-D SWNT system compared to on the 2-D graphene system.

2.5 CONCLUSIONS

In summary, we compared the amperometric detection of H_2O_2 using Pt-SWNT, Pt-CCG and Pt-CCG-S and showed that Pt-SWNT had the highest sensitivity and ECSA while Pt-CCG-S had the lowest. Electrochemical and FET characterization explained such trend of decreasing sensitivities and ECSA for Pt-SWNT, Pt-CCG and Pt-CCG-S as (1) the Pt NP has a larger influence on the 1-D SWNT system than on the 2-D graphene system, which made the composite material more conductive; (2) the bundle structure of SWNTs and relatively low solubility of CCG resulted in a more porous electrode surface structure. Our findings on H_2O_2 system might be further related to other analytical/non-analytical systems, and also energy-related applications such as oxygen reduction, where materials decorated with Pt nanoparticles function as the catalysts.

2.6 ACKNOWLEDGEMENT

Y.T. acknowledges a graduate student fellowship through Bayer MaterialScience. G.P.K. acknowledges an EPA STAR Graduate Fellowship FP-91713801. We thank the Department of Biological Sciences and the Department of Materials Science and Engineering at the University of Pittsburgh for access to the TEM and SEM instrumentation.

3.0 LONG-TERM PERFORMANCE OF PLATINUM DECORATED CARBON NANOTUBES FOR FUEL CELL CATHODES

3.1 CHAPTER PREFACE

The aim of this work was to investigate Pt-CNTs hybrid structures as fuel cell catalysts, targeting at a better alternative for commercial Pt/C catalyst with improved performance (life-time) but less Pt materials. Specifically, both electrochemical characterizations for ORR and long-term performance evaluation in phosphoric acid fuel cell (PAFC) condition were carried out for two Pt-CNTs materials obtained in the laboratory. And such performance was compared to that of commercial Pt/C materials in PAFC.

Here we report the electrochemical properties and performance of Pt-decorated carbon nanotube (Pt-CNT) catalysts for long-term operation in phosphoric acid fuel cells (PAFCs). Electrochemical measurements of Pt-CNT catalysts including cyclic voltammetry, rotating ring disk electrode voltammetry, and electrochemical impedance spectroscopy were conducted to evaluate the catalyzed oxygen reduction reaction (ORR). Furthermore, we tested the long-term performance of the Pt-CNT catalysts in 2” × 2” PAFC cathodes operating at 190 °C in 85% H_3PO_4 for extended periods (up to 240 days). Lifetime studies show that electrodes containing the Pt-CNT catalysts were approximately 20 times more stable than conventional Pt-C catalyst materials, even with a substantially thinner catalyst layer. This finding of the enhanced Pt-CNT

catalyst stability bodes well for possible personal electronics or automotive applications, where catalyst longevity is an essential requirement.

The material contained in this chapter was published as a research paper in the journal *Energy and Fuels* and has been reprinted (adapted) with permission from *Energy and Fuels* **2010,** *24*, 1877–1881, Copyright © 2010, American Chemical Society. The full citation is listed as reference [122] in the bibliography section.

List of Authors: Douglas R. Kauffman, Yifan Tang, Padmakar D. Kichambare, John F. Jackovitz and Alexander Star

Author contributions: All authors contributed to the design of experiments and writing of the paper. Synthesis of Pt-CNTs was carried out by DRK, YT and PDK. Fabrication of 2" × 2" PAFC electrode was done by DRK and YT. Electron microscopy, EDX XRD spectroscopy were performed by DRK. Electrochemical testing was performed by DRK and YT. PAFC assembly and testing were done in collaboration with Hydrogen LLC with the contribution of PDK and JFJ.

3.2 INTRODUCTION

Recent years have witnessed increased interest in the development and application of carbon-based nanomaterials for energy production.[227-229] For example, carbon nanotubes (CNTs) decorated with appropriate nanoparticle (NP) species show exquisite catalytic activity,[33-34, 230-232] and they have been incorporated into a variety of fuel cell platforms, including polymer

electrolyte fuel cells,[18-19, 27, 138, 233-234] alcohol oxidation fuel cells,[53, 235-239] and phosphoric acid fuel cells (PAFCs).[240] So much excitement surrounds CNT-based fuel cell catalysts because they show greater electrochemical stability than conventional carbon-based catalyst supports,[241-242] and this characteristic of CNT-based fuel cell electrodes affords the possibility of designing platforms with higher power density per unit volume and extended operational lifetimes.

Here, we present data detailing the long-term operation of PAFC cathodes composed of Pt NP-decorated CNTs (Pt-CNTs). We observed stable power densities between 50 and 75 mW cm^{-2} for 2" × 2" (25.8 cm^2) electrodes operating at 190 °C in 85% H_3PO_4 for up to 240 days. With a minimal decrease in the measured power density, we demonstrate that Pt-CNT-based fuel cell electrodes can show extended operational lifetimes as compared to conventional catalyst materials.

3.3 EXPERIMENTAL SECTION

3.3.1 CNT Decoration and Electrochemical Measurement

CNTs were obtained from the Columbia Chemicals Company. Catalyst 1 was prepared through the reduction of aqueous H_2PtCl_6 onto the CNTs with $NaBH_4$,[243] and catalyst 2 was prepared by impregnating the CNTs with 1,5-cyclooctadiene dimethyl platinum [$Pt(COD)Me_2$] in supercritical CO_2 followed by reduction with H_2.[244] The resulting Pt-CNTs were suspended in ethanol at a concentration of 0.25 mg/mL. Scanning electron microscopy (SEM) and energy-dispersive X-ray (EDX) spectroscopy were performed with a Phillips XL30 FEG microscope equipped with an EDAX assembly. X-ray diffraction (XRD) patterns were collected on a Phillips

MPD-1880 multi-purpose diffractometer system. Transmission electron microscopy (TEM) was performed with a JEOL 200CX microscope. The percent weight Pt was determined by weighing the samples before and after heating to 900 °C in air or with a Q500 thermogravimetric analysis (TGA) system ramped to 900 °C in air.[31] Electrochemical measurements, including cyclic voltammetry (CV), electrochemical impedance spectroscopy (EIS), and rotating ring disk electrode (RRDE) voltammetry were performed using CH Instruments electrochemical analyzers at room temperature in N_2 or O_2 saturated 0.5 M H_3PO_4 with Ag/AgCl reference and Pt wire counter electrodes. All electrochemical measurements were conducted with 1:9 (v/v) mixtures of 5% Nafion and the ethanol-suspended Pt-CNTs dropcast onto the electrode surface. The potentials are reported versus the reference electrode. The RRD electrode (Pine electrodes, model E7R9; reported collection efficiency, N = 0.37) contained a glassy carbon (GC) disk and Pt ring electrode. The ring portion of the RRDE was polarized at 1.0 V, and rotation speeds were controlled with a Pine Instruments rotating electrode speed controller.

3.3.2 Electrode Fabrication and Measurement

Electrode substrates were composed of graphite paper coated with a wetproofing layer of carbon powder and Teflon. The electrodes were heated to 100 °C, and ethanol-suspended Pt-CNTs were spray-casted onto the surface with a commercial airbrush (Iwata) to obtain a total Pt loading of 0.3 mg/cm^2. The electrodes were cut into 2" × 2" (25.8 cm^2) squares and passed through a temperature profile in a Grieve belt furnace to sinter the underlying wet-proofing layer and permanently bind the Pt-CNT material to the electrode surface (Figure 3-5 in section 3.8 Supporting Information). Testing was performed in custom-built fixtures composed of stainless-steel blocks, graphite seals, and Teflon feed tubes (Figure 3-6 in section 3.8 Supporting

Information). The cell fixtures were insulated with fiberglass wool to maintain an operating temperature of 190 °C, and acid additions were performed manually at specific intervals. Fuel cell anodes were composed of commercially available Pt-decorated carbon black from Columbian Chemicals Company or Johnson Matthey (~2 nm Pt NPs, 10-15% Pt) on identically prepared graphite paper substrates, with a total Pt loading of 0.5 mg/cm^2 (Figure 3-7 in section 3.8 Supporting Information). Cathodes composed of commercially available catalyst were prepared in an identical manner. The supporting electrolyte was 85% H_3PO_4 maintained at a temperature of 190 °C. Air and H_2 were passed over the cathode and anode at a typical flow rate of 28 L/min at a pressure of 2.0 atm. The electrode current and voltage output were sampled with computer-interfaced GW Instek model GDM-8246 multimeters.

3.4 RESULTS AND DISCUSSION

TEM and TGA revealed that catalyst 1 contained ~10 nm Pt NPs and had a total Pt loading of 20% (wt%), whereas catalyst 2 had ~2 nm Pt NPs and a total Pt loading of 11.5% (wt%). Figure 3-1 contains TEM images of the two Pt-CNT catalyst materials, where smaller and better dispersed Pt NPs are visible on catalyst 2. XRD patterns of catalysts 1 (black curve) and 2 (red curve) are presented in Figure 3-1c, and samples show signatures of polycrystalline Pt species; the XRD patterns have been offset for clarity. Using the Scherrer equation to estimate the Pt NP size from the Pt (220) peak in the XRD patterns,[53] we calculated~8 nm Pt NPs in catalyst 1 and ~3 nm NPs in catalyst 2, agreeing reasonably well with the particle size estimate from TEM imaging.

Mixtures (1:9, v/v) of 5% Nafion and ethanol-suspended Pt-CNT catalysts were dropcast onto GC electrodes to evaluate the electrocatalytic activity toward the oxygen reduction reaction (ORR) using CV. For example, Figure 3-2a presents the cathodic sweep for the stabilized (10th scan) CV of catalysts 1 (black curves) and 2 (red curves) in 0.5 M H_3PO_4 saturated with N_2 (- - -) or O_2 (---). Only the cathodic sweeps have been shown for clarity; however, full CVs are shown in Figure 3-8 in Section 3.8 Supporting Information. In N_2-saturated H_3PO_4 neither material showed significant oxidation or reduction peaks in the experimental potential window, but we observed a peak corresponding to the catalyzed ORR after saturating the solution with O_2.[19, 30] Moreover, we found that the ORR followed diffusion-limited behavior, such that the peak current scaled linearly with the square root of the scan rate (Figure 3-2b).[245] We observed a more positive ORR onset potential and larger peak current for catalyst 2, indicating that catalyst 2 demonstrated a higher catalytic activity toward the ORR presumably from the smaller and more well-dispersed Pt NPs.[246-247]

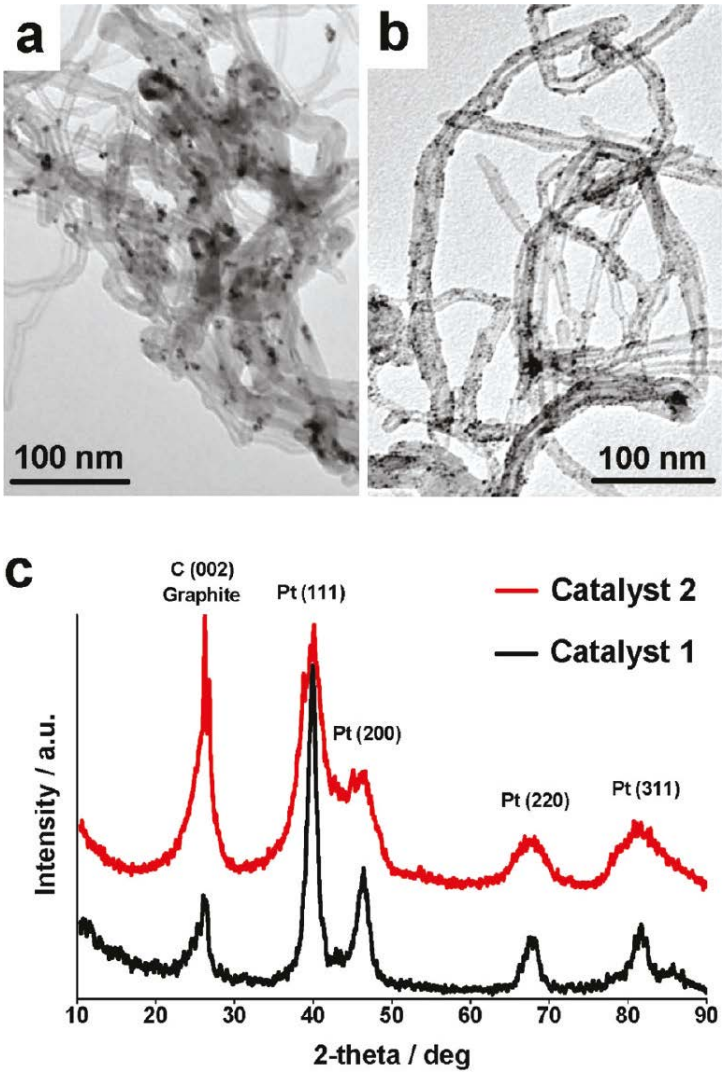

Figure 3-1. TEM images of (a) catalyst 1 and (b) catalyst 2. (c) XRD patterns of Pt-CNT catalysts 1 (lower black curve) and 2 (upper red curve); the XRD patterns have been offset for clarity.

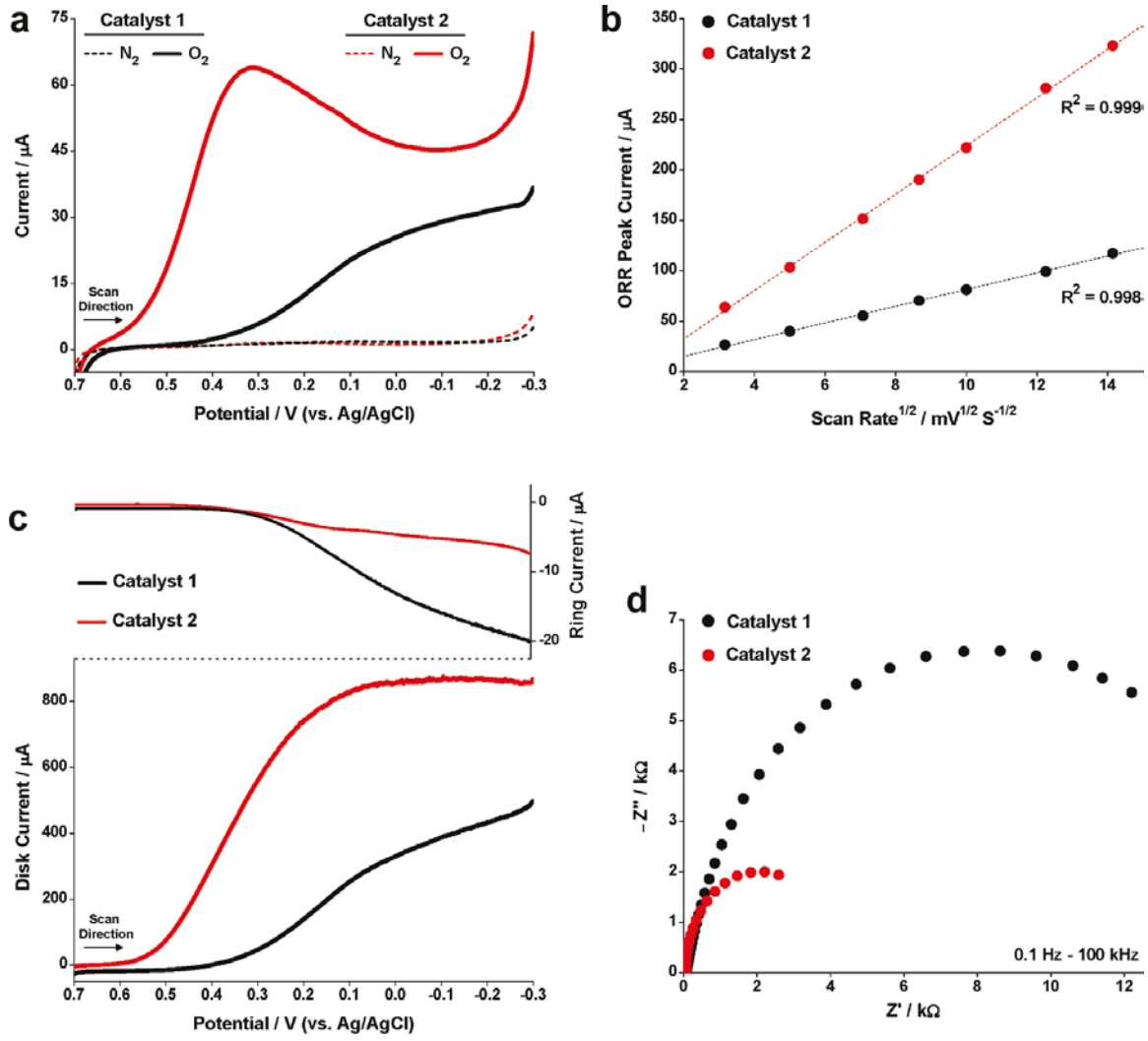

Figure 3-2. (a) Cathodic scans of the stabilized cyclic voltammograms of catalyst 1 (black curves) and catalyst 2 (red curves) in N_2 (- - -) and O_2 (——) saturated 0.5 M H_3PO_4 showing the catalyzed ORR. Cyclic voltammograms were measured at room temperature with a scan rate of 10mV s-1. (b) Plot of the ORR peak current versus the square root of the scan rate. (c) RDDE voltammograms of catalysts 1 and 2 in O_2-saturated 0.5 M H_3PO_4. The bottom segment corresponds to the ORR occurring at the disk electrode, while the top segment corresponds to the ring current and represents the oxidation of intermediate species produced at the disk electrode through incomplete O_2 reduction. The ring electrode was polarized at 1.0 V, and the voltammograms were collected by scanning the disk electrode in the cathodic direction at a rate of 10 mV s^{-1} at room temperature. (d) Nyquist plots of EIS of catalysts 1 and 2 in O_2-saturated 0.5 M H_3PO_4. A frequency range from 0.1 Hz to 100 kHz was used at an excitation signal of 10 mV, and the different catalysts were held at their respective peak ORR potential, as shown in panel a.

RRDE voltammetry was used to further study the Pt-CNT catalyzed ORR. Figure 3-2c presents the RRDE curves for catalysts 1 (black curves) and 2 (red curves) in O_2-saturated H_3PO_4 at a rotational speed of 1000 rpm. The bottom segment shows the current collected from the disk portion of the electrode and indicates a one-step O_2 reduction process.[30-31] Similar to the CV measurements, the RRDE curves show more positive ORR onset potential and a larger current for catalyst 2. The upper segment of Figure 3-2c displays the Pt ring current and corresponds to the oxidation of intermediate species produced at the surface of the disk electrode. In this experimental setup, a larger ring current indicates the production of more intermediate species and ultimately points toward less efficient ORR catalysis. Catalyst 2 demonstrated a smaller ring current, which agrees with the more positive ORR onset potential and larger disk current to indicate higher efficiency ORR catalysis.

Using equation 3-1, we were able to calculate the number of electrons (n) transferred per O_2 molecule during the ORR. [30-31]

$$n = 4I_D / (I_D + I_R / N) \quad (3\text{-}1)$$

Here, n is the number of electrons transferred; I_D and I_R are the measured disk and ring electrode currents, respectively; and N is the collection efficiency (0.37). On the basis of our calculations, at -0.15 V, the n values for catalysts 1 and 2 were 3.60 and 3.93, respectively. These values reflect the expected four electron transfer that occurs at Pt-based catalysts during the ORR,[30] and the more ideal (i.e., closer to 4.0) electron-transfer number for catalyst 2 points toward more efficient catalysis.

EIS provides valuable insight into the charge transfer of the catalyst material. For example, Figure 3-2d presents the EIS curves for catalysts 1 (black labels) and 2 (red labels) in in O_2-saturated 0.5 M H_3PO_4. For measurement of the different catalysts, the electrode was held at

the respective ORR peak potential, as shown in Figure 3-2a. Here, the real (Z') and imaginary (Z") parts of the impedance are displayed as a Nyquist plot in the frequency range from 0.1Hz to 100 kHz at an excitation signal of 10 mV. The semi-circular nature of the EIS curves indicates a kinetically controlled system, where the width of the semi-circle is proportional to the charge-transfer resistance of the catalyst material.[245, 248] The larger width of the catalyst 1 EIS curve points toward higher charge-transfer resistance and slower charge-transfer kinetics. The EIS results combined with the CV and RRDE experiments lead to the conclusion that catalyst 2 demonstrates higher overall catalytic activity toward the ORR in H_3PO_4.

We tested the performance of both Pt-CNT materials as PAFC cathodes using 2" × 2" (25.8 cm^2) wet-proofed graphite paper electrodes. Figure 3-3 shows SEM images of a typical cathode containing the Pt-CNT catalysts. Panel a contains a cross-sectional SEM image of the cathode. While the entire electrode is several hundred micrometers thick, the actual Pt-CNT catalyst layer is relatively thin (~50 μm). This method of thin CNT-based electrode fabrication is advantageous because it can help avoid mass-transfer losses at the electrode surface1c and it presents the opportunity to create platforms with higher power density per volume of electrode.[249] Panels b and c are higher magnification SEM images of the electrode surface. We observed that the surface of the electrode is quite uneven, but the spray-casting method produces uniform Pt-CNT networks across the electrode surface. Moreover, the porous nature of the CNT network is favorable for diffusion of gas and electrolyte at the electrode surface.[229] Lastly, panel d is an EDX spectrum of the electrode, and EDX mapping shows even elemental distribution across the electrode surface (Figure 3-9 in Section 3.8 Supporting Information).

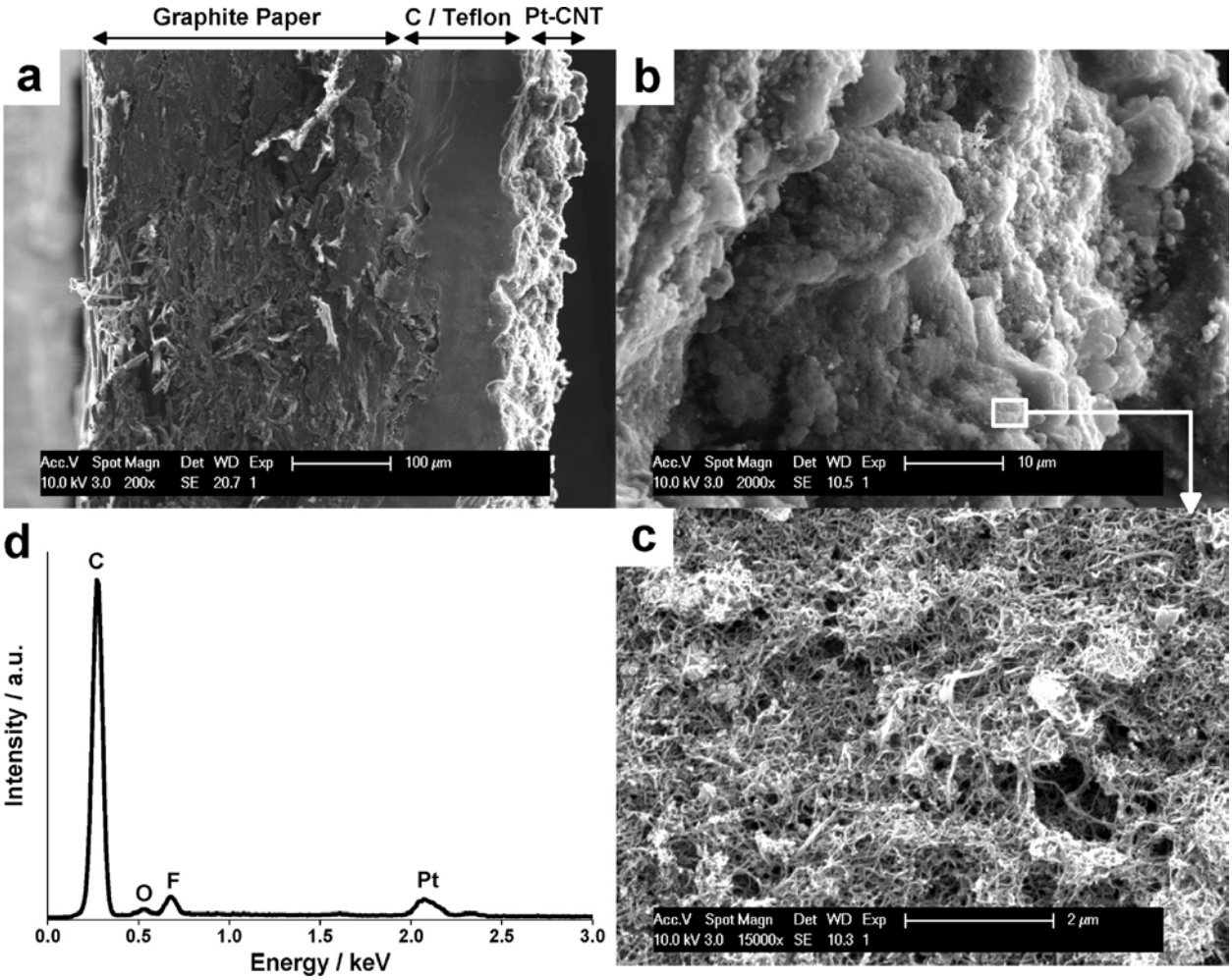

Figure 3-3. SEM images and EDX spectroscopy of a Pt-CNT catalyst network spray cast onto a wet-proofed graphite paper electrode. (a) Cross-sectional SEM of the electrode showing the graphite paper, carbon, and Teflon wet-proofing layer and the Pt-CNT network. (b and c) SEM images of the electrode surface showing the morphology of the Pt-CNT layer. (d) EDX spectrum of the electrode, where the F signal comes from the Teflon coating underneath the Pt-CNT layer.

Cathodes were placed into custom-built PAFC-testing fixtures, and panels a and b of Figure 3-4 present the long-term power density (mW cm^{-2}) of cathodes containing catalysts 1 and 2, respectively. The cathode-containing catalyst 1 operated for 240 days (~5760 h) and showed a stable power density of ~52 mW cm^{-2} while operating at 3.0 A and 450 mV. During testing, a

power outage disrupted the operation of the fuel cell at day 45 and resulted in the cell being held at open circuit voltage (OCV) for approximately 2.5 days. After resuming operation, we observed an increased cell current of 5.0 A, but a decreasing cell voltage decreased the overall power density. After the cell current was manually reset to 3.0 A, the power density returned to a stable value that was nearly identical to what it was before the power outage. This unintended experiment demonstrates that the cell can continue to function at a stable level even if it is left at OCV for extended periods. As shown in Figure 3-4b, the cell containing a cathode with catalyst 2 operated for 27 days (~650 h) and achieved a higher overall power density of ~74 mW cm^{-2} operating at 4.0 A and 460 mV, which is comparable to the catalytic activity of Pt-decorated single-wall nanotubes (SWNTs) and conventional Pt-C catalysts operating at high temperature as PAFC.[240, 250-252] Because the CNTs were identical in both Pt-CNT samples, we attribute the higher cell performance to the smaller size and better distribution of the Pt NPs in catalyst 2.

Dividing the electrode current density by Faraday's constant will give the number of electrons transferred per unit area of electrode per second.11c For example, we calculated that the electrodes containing catalysts 1 and 2 had respective rates of 1.8×10^{17} and 2.42×10^{17} cm^{-2} s^{-1} for the four electron ORR. Moreover, we can estimate the turnover frequency (TOF) per active surface site from the total Pt loading on the electrode surface and the fraction of exposed (FE) Pt atoms, where the FE is calculated from the total number of Pt atoms in a NP (on the basis of the particle size) and the surface area of the Pt NPs; the FE is approximately equal to 1.1 nm/d, where d is the particle diameter in nanometers. On the basis of the calculated ORR reaction rates and FE values, the TOF values (per surface atom site per second; $atom^{-1}$ s^{-1}) for the electrodes containing catalysts 1 and 2 were 1.6 and 0.59 $atom^{-1}$ s^{-1}, respectively, which are comparable to other carbon-supported Pt catalysts.[253]

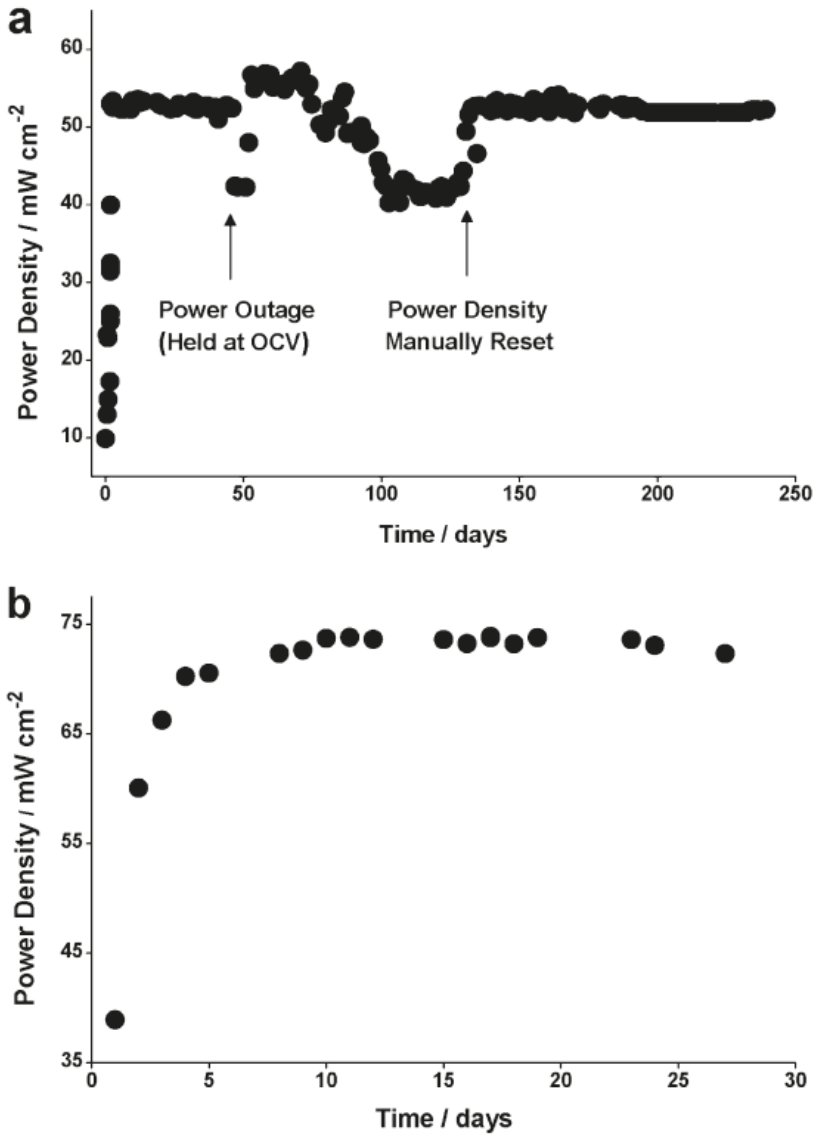

Figure 3-4. Long-term performance of PAFC cathodes containing (a) catalyst 1 and (b) catalyst 2.

For comparison, we also tested cathodes containing a ~400 μm thick catalyst layer of commercially available Pt-decorated carbon black (Figure 3-7 in Section 3.8 Supporting Information). Operating at 5.0 A, these cells typically experienced a decay in power density of ~2 $mWcm^{-2}$ per 1000 h of operation. In the case of the Pt-CNT cathodes, we observed a much

smaller decay for the same 1000 h operational period. Specifically, we observed a 0.09 $mWcm^{-2}$ decay in cell power density for both cathodes containing Pt-CNT catalysts. However, we should note that, for the cathode containing catalyst 2, we had to extrapolate this value based on the stabilized power density of the cell. These results show that, in the experimental time frame, the Pt-CNT cathode power densities were more than an order of magnitude more stable than those prepared with a much thicker layer (~400 versus ~50 μm) of commercially available catalyst material.

3.5 CONCLUSIONS

In conclusion, we have shown that one can accurately relate the performance of 2" × 2" PAFC cathodes to the electrochemical characteristics of Nafion/ethanol-suspended Pt-CNTs. Specifically, the electrochemical characterization of the two materials suggested that catalyst 2 possessed a higher catalytic activity toward the ORR that we attributed to the smaller and more well-dispersed Pt NPs.[246-247] This observation translates directly to the fuel cell cathodes, where we observed an approximately 44% higher power density from the cell with a cathode containing catalyst 2. Finally, we have shown that cathodes composed of a thin Pt-CNT layer can operate for extended periods (240 days, ~5760 h) in the harsh working environment of a PAFC (190 °C, 85% H_3PO_4) with much less degradation in cell performance than much thicker layers of conventional catalyst materials. This suggests that CNT based electrodes have the potential for operating in fuel cell platforms for general energy production, automotive, or personal electronic applications, where catalyst longevity is an essential requirement.

3.6 ACKNOWLEDGMENT

D.R.K. acknowledges a graduate student fellowship through Bayer MaterialScience. This work was supported by the Pennsylvania NanoMaterials Commercialization Center through funding provided by the Department of Community and EconomicDevelopment (DCED). We also thank the technical staff of Hydrogen, LLC for performing the fuel cell lifetime measurements and the Department of Materials Science and Engineering at the University of Pittsburgh for access to the SEM, TEM, and XRD instrumentation.

3.7 SUPPORTING INFORMATION

This supporting information contains PAFC electrode sintering parameters (Figure 3-5), PAFC testing equipment (Figure 3-6), XRD and TEM characterization of commercial Pt-C catalyst materials (Figure 3-7), full cyclic voltammograms for Pt-CNTs (Figure 3-8) and EDX elemental mapping of typical Pt-CNT cathode surface (Figure 3-9).

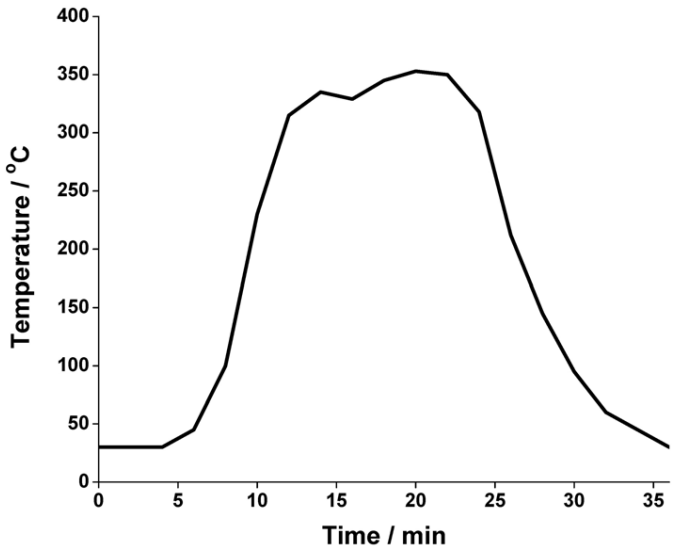

Figure 3-5. Belt furnace temperature profile used for electrode sintering in air.

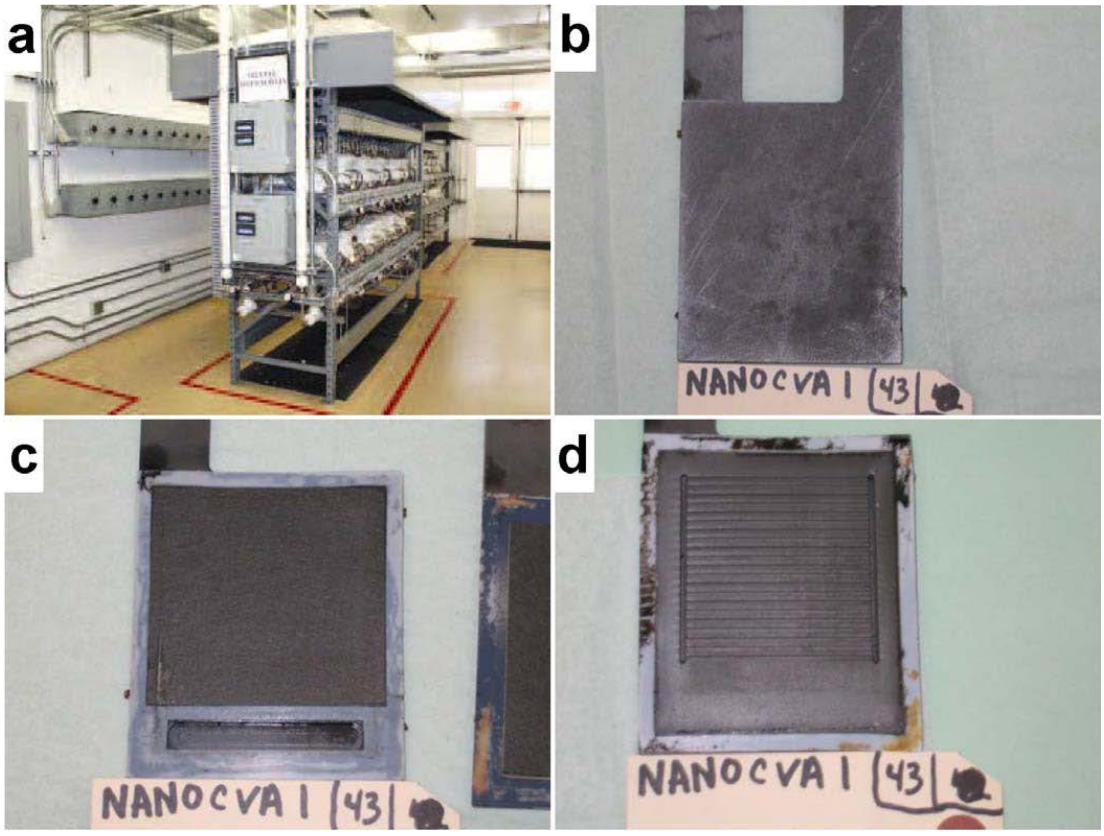

Figure 3-6. (a) Fuel cell testing apparatus at Hydrogen LLC containing 36 individual stations each maintained at 190 ± 5 °C and allowing separate electrical measurements during operating; (b) Completed PAFC cell. (c) PAFC half-cell with the Pt-CNT cathode face down. (d) Empty PAFC half-cell with interstitial channels for gas and electrolyte delivery to the electrode surface.

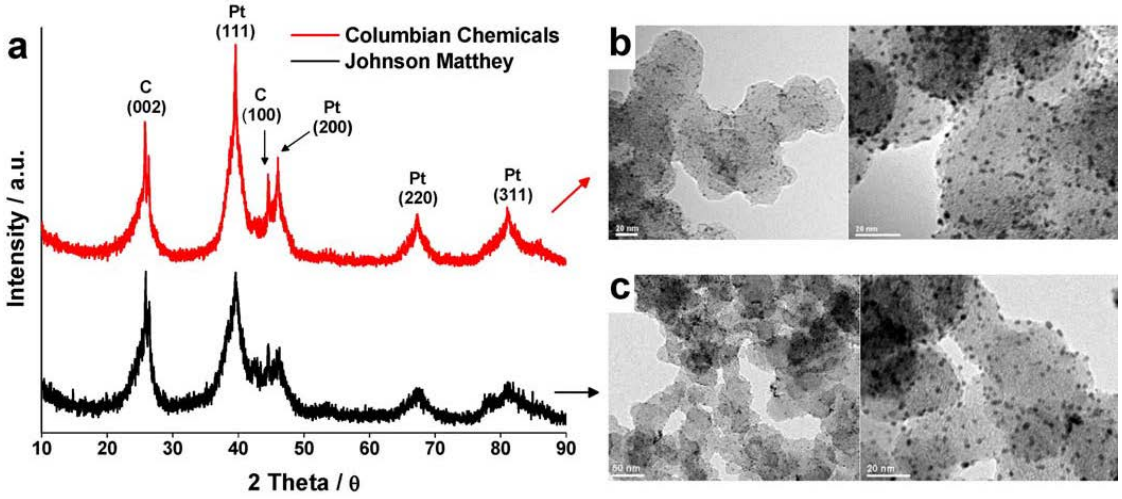

Figure 3-7. (a) X-Ray diffraction patterns of the commercially available Pt-decorated carbon black obtained from Columbian Chemicals Company (red curve) and Johnson Matthey (black curve). Transmission electron micrographs of the catalyst material obtained from (b) Columbian Chemicals Company and (c) Johnson Matthey.

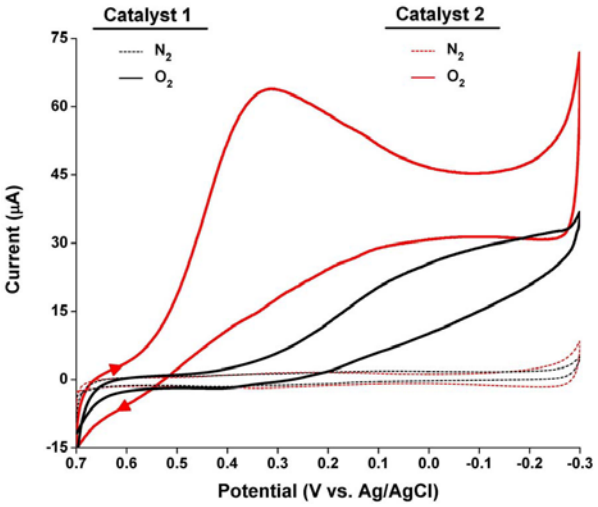

Figure 3-8. Stabilized (10^{th} scan) cyclic voltammograms (CVs) of catalyst 1 (black curves) and 2 (red curves) in N_2 (dashed lines) and O_2 (solid lines) saturated 0.5 M H_3PO_4 showing the catalyzed oxygen reduction reaction (ORR); CVs were measured at room temperature with a scan rate of 10 mV s^{-1}. For further details please see Figure 3-2a and accompanying description in chapter 3.

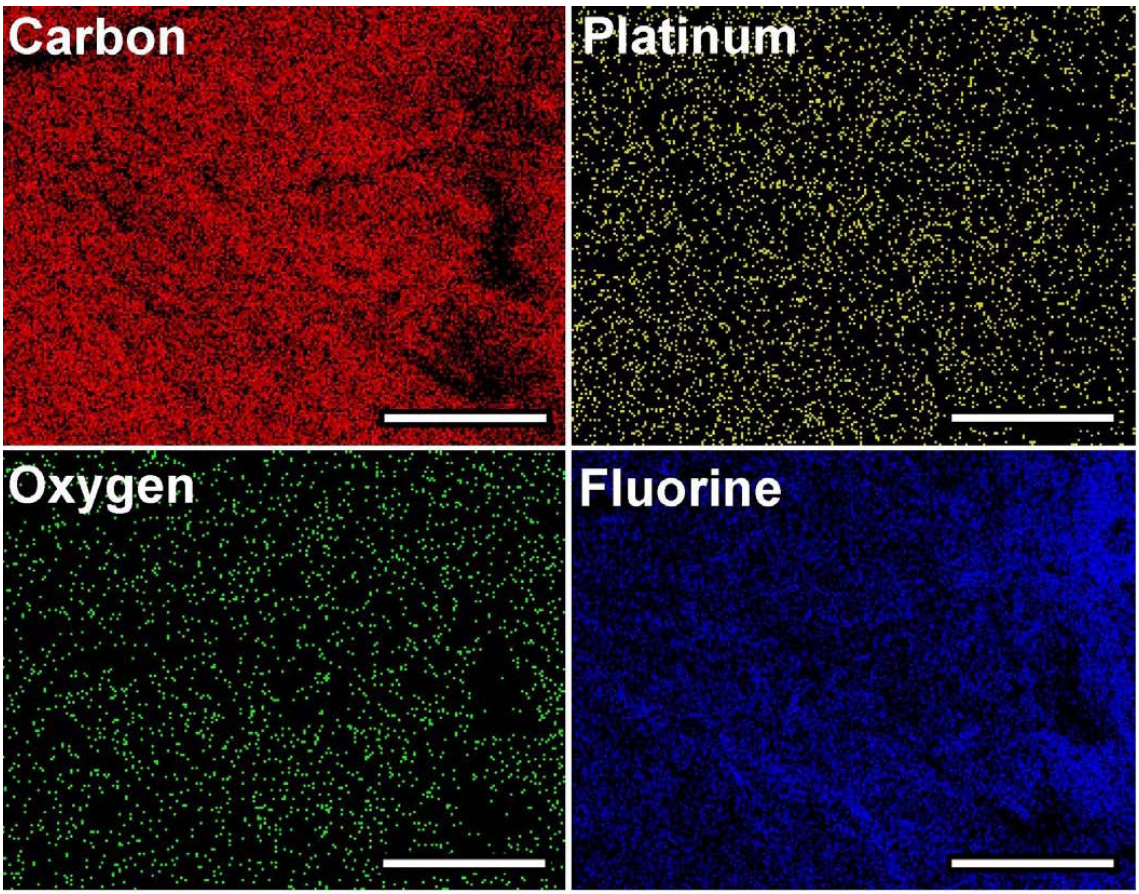

Figure 3-9. Energy dispersive X-ray (EDX) elemental mapping of a typical Pt-CNT cathode surface (please see Figure 3-3d for an EDX spectrum). Scale bars correspond to 10 μm.

4.0 ELECTROCHEMICAL APPLICATIONS OF NITROGEN-DOPED CARBON NANOTUBE CUPS

4.1 CHAPTER PREFACE

As we demonstrated in Chapter 2 and 3, Pt-CNTs were good candidates for fuel cell cathodes for ORR and H_2O_2 sensors. However they still require expensive Pt as the catalyst materials. The aim of this work was to investigate the possibility of using non-precious-metal based materials, in this case, nitrogen-doped carbon nanotube cups (NCNCs) for both fuel cells and biosensor applications. Specifically, NCNCs were synthesized, characterized and tested for ORR using various electrochemical techniques and further fabricated in to a glucose sensor to demonstrate the feasibility of using NCNCs for biosensor applications.

In this chapter, the electrochemical activity of stacked nitrogen-doped carbon nanotube cups (NCNCs) has been explored in comparison to commercial Pt-decorated carbon nanotubes. The nanocup catalyst has demonstrated comparable performance to Pt catalyst in oxygen reduction reaction. In addition to effectively catalyzing oxygen reduction, the NCNC electrodes have been used for hydrogen peroxide oxidation and consequently for glucose detection when NCNCs were functionalized with glucose oxidase (GOx). Creating the catalysts entirely free of precious metals is of great importance for low-cost fuel cells and biosensors.

The material contained in this chapter was published as a research paper in the *Journal of the American Chemical Society* and has been reprinted (adapted) with permission from the *Journal of the American Chemical Society* **2009,** *131*, 13200-13201, Copyright © 2009, American Chemical Society. The full citation is listed as reference [31] in the bibliography section.

List of Authors: Yifan Tang, Brett L. Allen, Douglas R. Kauffman and Alexander Star

Author contributions: All authors contributed to the design of experiments and writing of the paper. Material synthesis and electrochemical characterization were performed by YT. YT, BLA and DRK contributed to the TEM characterization. The TGA and XPS analysis were carried out by DRK.

4.2 INTRODUCTION

Carbon-based nanomaterials, such as nanotubes[254] and graphene,[255] are currently at the forefront of materials research because they show outstanding electrocatalytic activity due to their unique electrical and chemical properties. Furthermore, the doping of these carbon nanostructures with nitrogen atoms has drawn much attention because conjugation between the nitrogen lone-pair electrons and the graphene π-system[79, 256-257] may create nanomaterials with tailored electronic and mechanical properties. Recently, Dai and co-workers reported that nitrogen-doped carbon nanotube arrays demonstrate high electrocatalytic activity for the oxygen reduction reaction (ORR),[30] with a great potential for low-cost non-platinum catalysts for fuel cell cathodes. However, the exact extent of the electrocatalytic activity of these nanomaterials and their

application for other electrochemical reactions remained unknown. In this work we compare nitrogen-doped carbon nanotube cups (NCNCs) to commercial Pt-decorated multiwall carbon nanotubes (Pt-CNTs) as catalysts in ORR and demonstrate their applications for electrochemical detection of hydrogen peroxide and glucose.

4.3 EXPERIMENTAL SECTION

4.3.1 Materials

Nafion®117 solution (5 wt%), GOx (type: X-S, *Aspergillus niger*, 147,000 units/g) were obtained from Aldrich-Sigma (St. Louis, MO). H_2O_2 (3% aqueous solution) was obtained from J. T. Baker (Phillipsburg, NJ). Pt-CNTs sample was received from Columbia Chemical Company. All gases were purchased from Valley National Gases.

4.3.2 Preparation of Nitrogen-doped Carbon Nanotube Cups (NCNCs)

NCNCs were synthesized via chemical vapor deposition (CVD) in a Lindberg/Blue tube furnace, on a quartz substrate placed in a quartz tube (1" dia.) inside the furnace. The growth was carried at 950 °C for 1 hour. A liquid precursor consisting 5.0 g of MeCN, 1.25 g of ferrocene, and 93.75 g of EtOH was injected into the furnace at a rate of 5 mL/h for 1 hour with carrier gases of Ar at 422 sccm and H_2 at 125 sccm. After the growth, the system was then allowed to cool down to room temperature under an Ar atmosphere. NCNCs product was collect using a razor blade from the quartz substrate in the formed as a black coating.

4.3.3 Characterization

Low-resolution transmission electron microscopy (TEM) images were obtained with a Philips/FEI Morgagni microscope. The electron beam accelerating voltage of the TEM was held at 80.0 keV for all imaging. All nanocup samples were prepared by suspension in DMF or EtOH and drop-casting on a lacey carbon TEM grid (Pacific Grid-Tech) and by allowing the solvent to evaporate completely.

Thermogravimetric analysis (TGA) was performed using TGA Q500 thermal analysis system in air at a temperature ramp rate of 125 °C/min.

X-ray photoelectron spectroscopy (XPS) was performed using a PHI 5600ci spectrometer employing Al Kα X-rays with a base pressure better than 1 x 10^{-8} torr. XPS samples were prepared by briefly sonicating the NCNCs in ethanol and dropcasting them onto a quartz substrate heated to 100 °C. Because quartz was used as a substrate, an electron flood gun was used to neutralize surface charging. XPS binding energies were corrected using the Si 2p peak of the quartz substrate at a binding energy 103.4 eV as an internal standard, and the reported spectrum is the average of 20 individual scans.

4.3.4 Electrode Preparation

Glassy carbon (GC) electrode (CHI 104, GC area 0.0707cm^2, total area 0.196 cm^2) was carefully polished with gamma alumina powder (0.05 micron, CH Instruments) until a mirror finish was obtained. Then the electrode was rinsed and sonicated with plenty of double distilled water to remove any alumina residues and finally dried in vacuum. A sample of stacked NCNCs (1 mg) was dissolved in 1 mL solvent mixture of Nafion (5%) and EtOH (V: V ratio = 1:9) by

sonication. For ORR and H_2O_2 detection, 20 μL of the NCNC solution was dropcasted on the glassy carbon electrode surface and dried in air.

For rotating ring-disk electrode (RRDE) voltammograms, a GC-disk-Pt-ring electrode modified with 10 μL of 0.5 mg/mL NCNC solution on the GC disk part (disk area 0.2475 cm^2) was used as the working electrode. The collection efficiency of the rotating ring-disk electrode was 37% as reported by the manufacturer.

For glucose detection, 20 μL of 12 mg/mL GOx was dissolved in 50 mM pH=7.2 PBS and was dropcasted on the GC electrode which was already modified with NCNCs. After the GOx solution was dried, 10 μL of Nafion solution (2.5 %, diluted with EtOH) was added and dried in air.

For Pt catalyst control experiments, 1mg/mL Pt-CNTs in a solution of Nafion (5%) and EtOH (V: V ratio = 1:9) was used in the above procedure.

All electrodes were kept in 50 mM pH=7.2 PBS at 4 °C and tested at room temperature.

4.3.5 Electrochemical Charazterization

Cyclic voltammetry (CV), amperometric measurements and RRDE voltammetry were performed using an electrochemical analyzer (CHI 604C, CH Instruments, Austin, TX). The RRDE experiments were carried out on a MSR Electrode Rotator (Pine Instrument Co.) and another electrochemical analyzer (CHI 600C) was used to record the ring current under floating gate configuration. A Pt wire electrode (CHI 115) and an Ag/AgCl, 3 M KCl (CHI 111) electrode were used as counter and reference electrodes, respectively. Modified GC or GC-disk-Pt-ring electrodes were used as the working electrode. Except for the GC-disk-Pt-ring electrode (AFE7R9GCPT), which was purchased from Pine Instrument Co (Grove City, PA), all other

electrodes were purchased from CH Instruments, Austin, TX. All potentials are reported versus the reference electrode.

4.4 RESULTS AND DISCUSSION

NCNCs, also known as nanobells,[258] have been synthesized via chemical vapor deposition (CVD) as we reported previously[47] using MeCN, EtOH, and ferrocene as liquid precursors and Ar and H2 as carrier gases. Transmission electron microscopy (TEM) images of NCNCs reveal that the nanomaterial is composed of individual nanocups stacked together to form long nanofibers (Figure 4-1a). Each nanocup has a proportional length and diameter of 12-40 nm, with a mean distribution of ~20 nm. The nitrogen content of the nanocups was determined at 2-7% by electron energy loss spectroscopy (EELS).[47] For electrochemical comparison, we used commercial Pt-CNTs with a tube diameter of 10 to 15 nm with a Pt particle size of ~1.5 nm (Figure 4-1b). The platinum content in Pt-CNTs was measured at 11.5% by thermogravimetric analysis (TGA) (Figure 4-5, Section 4.8 Supporting Information). Analogous to the previous study,[30] we have conducted cyclic voltammetry (CV) of stacked nanocups and Pt-CNTs in O_2 saturated 0.1 M KOH aqueous solutions (Figure 4-1c). We observed ORR peaks for NCNCs and Pt-CNTs at -0.438 and -0.386 V, respectively. These peaks were absent in N_2 saturated solutions (Figure 4-6, Section 4.8 Supporting Information).

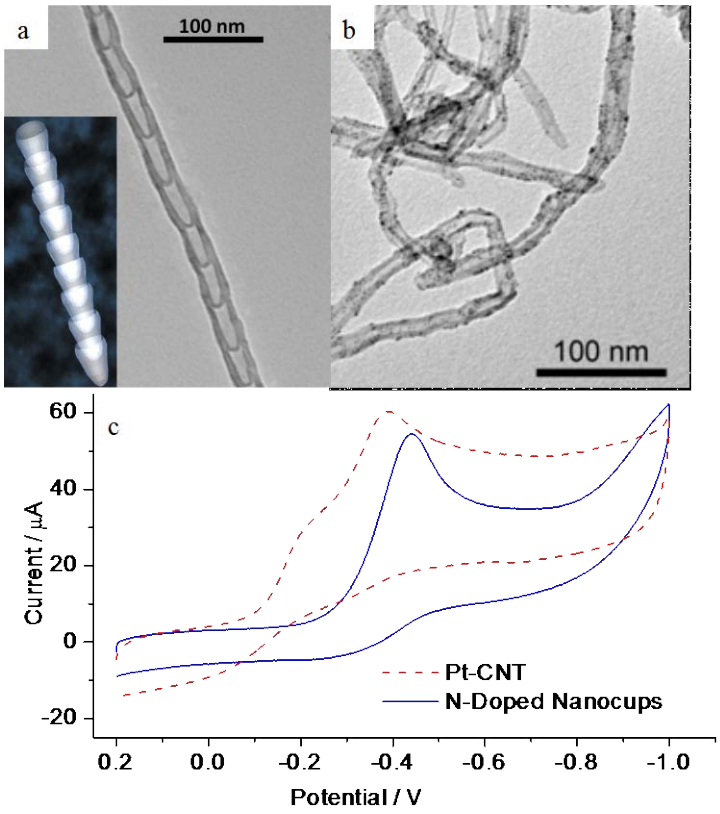

Figure 4-1. (a) Transmission electron microscopy (TEM) image of stacked nitrogen-doped carbon nanotube cups (NCNCs). Inset: cartoon illustrating orientation of the nanocups in stacked NCNC. (b) TEM image of commercial Pt-CNTs. (c) Cyclic voltammograms (CV) of stacked NCNCs versus commercial Pt-CNTs in oxygen saturated 0.1 M KOH aqueous solution both showing the oxygen reduction reaction (ORR) peaks.

Comparison of the ORR CVs reveals that NCNCs and Pt-CNTs have similar peak shapes, intensities, and positions. This similarity indicates that NCNCs have electrochemical activity for ORR comparable to that of Pt catalyst. To rule out the possibility that traces of Pt metal (from glassware or Pt-counter electrode) might be responsible for the observed electrocatalytic activity of NCNCs, we have confirmed these CV results using brand new glassware and Cu foil as the counter electrode (Figure 4-7, Section 4.8 Supporting Information). NCNCs showed similar

durability (~1/3 current loss after 20000 s) to Pt-CNTs in ORR when tested under constant cathode potential (Figure 4-2a).

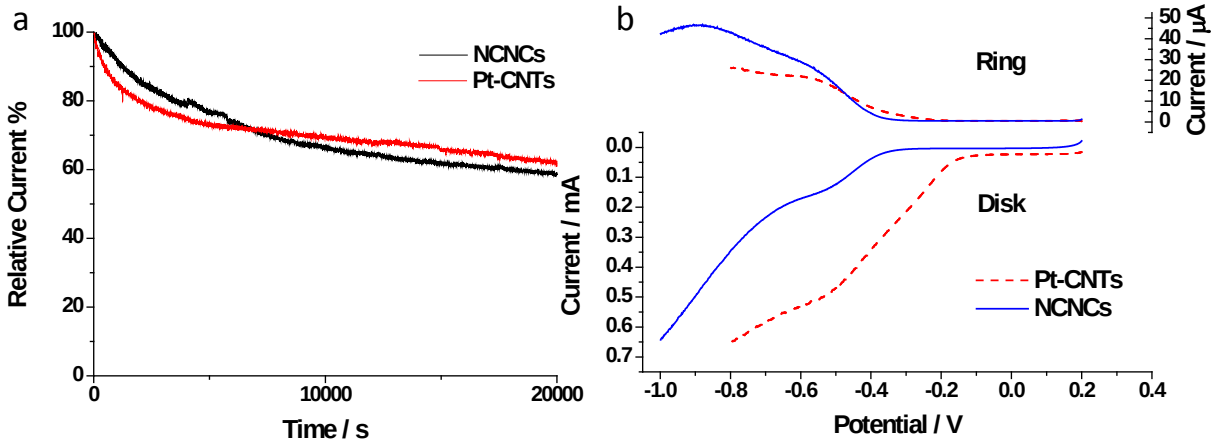

Figure 4-2. (a) i-t chronoamperometric response of stacked NCNCs(black) and Pt-CNTs(red) modified GC electrode in 0.1M KOH, saturated with O_2 under magnetic stir (1000 rpm); (b) RRDE voltammograms of stacked NCNCs (blue solid line) and Pt-CNTs (red dash line) in 0.1M KOH solution saturated with O_2. The ring-disk electrode rotation rate was 1400 revolutions per minute (rpm), and the Pt ring electrode was held at 0.5 V.

Furthermore, rotating ring disk electrode (RRDE) voltammetry was performed to study oxygen reduction under steady-state conditions. Transferred electron number (*n*) per oxygen molecule was calculated using Equation 3-1. At -0.53 V, the *n* for NCNCs and Pt-CNTs were 2.82 and 3.63, respectively. This suggested that while Pt-CNTs follow a four-electron pathway, the NCNCs' reduction process is a combination of two-electron and four-electron pathways (Figure 4-2b).

Based on the electrocatalytic performance of N-doped nanocups in ORR, it is worthwhile to investigate if NCNCs can catalyze other electrochemical reactions where Pt catalyst is

currently used. Electrochemical detection of H_2O_2 is a basis for detection of many medically important analytes[202] including glucose, which currently dominates the biosensor market.[259]

Figure 4-3 shows the amperometric response of a stacked NCNC modified glassy carbon (GC) electrode upon successive addition of different concentrations of H_2O_2 in 50 mM phosphate buffer solution (PBS) (pH = 7.2) at 500 mV vs Ag/AgCl reference electrode. The NCNC-modified GC electrode exhibits a linear range from 0.1 to 10 mM (R = 0.9936) with a sensitivity of 0.19 μA/mM. Above 10 mM H_2O_2, the electrode response deviates from linearity as it saturates.

The detection of glucose was performed by further modification of the NCNC-GC electrode with glucose oxidase (GOx) and Nafion. The amperometric response upon successive addition of glucose in 50 mM PBS (pH = 7.2) at 500 mV vs Ag/AgCl is shown in Figure 4-4. The response was proportional to the glucose concentration in a range from 0.3 to 7 mM with a sensitivity of 0.033 μA/ mM and a correlation coefficient of 0.9999. The limit of detection was estimated from the slope to be 0.3 mM at a signal-to-noise ratio of 3. Above 10 mM glucose the electrode is saturated and we observed a sluggish response with further addition. The results from this unoptimized glucose sensor were inferior to the performance of Pt-CNT electrodes (Figure 4-8, Section 4.8 Supporting Information). In our setup, electrodes modified with Nafion-GOx-Pt-CNTs showed a response to glucose with a lower detection limit of 0.01 mM and deviation from linearity at ~10 mM, which is comparable to the literature values.[202]

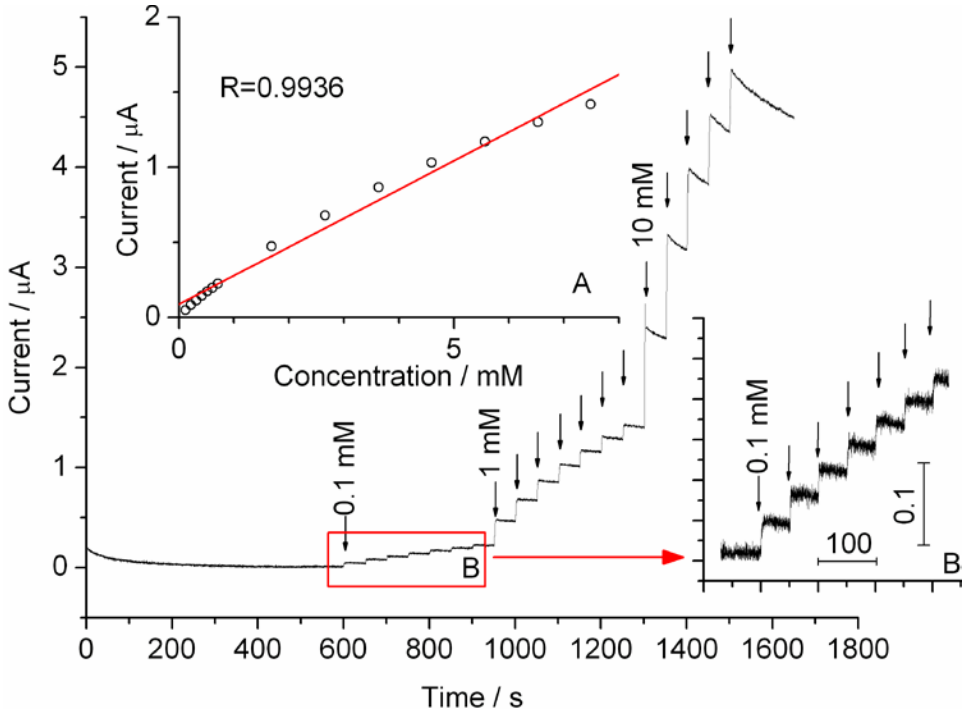

Figure 4-3. Current versus time curve of the stacked NCNCs modified GC electrode for successive addition of H_2O_2 (indicated by arrows with marked concentrations) to 50 mM pH=7.2 PBS at 0.50 V vs. Ag/AgCl. Inset A: calibration curve for H_2O_2. Inset B: amplification of curve B.

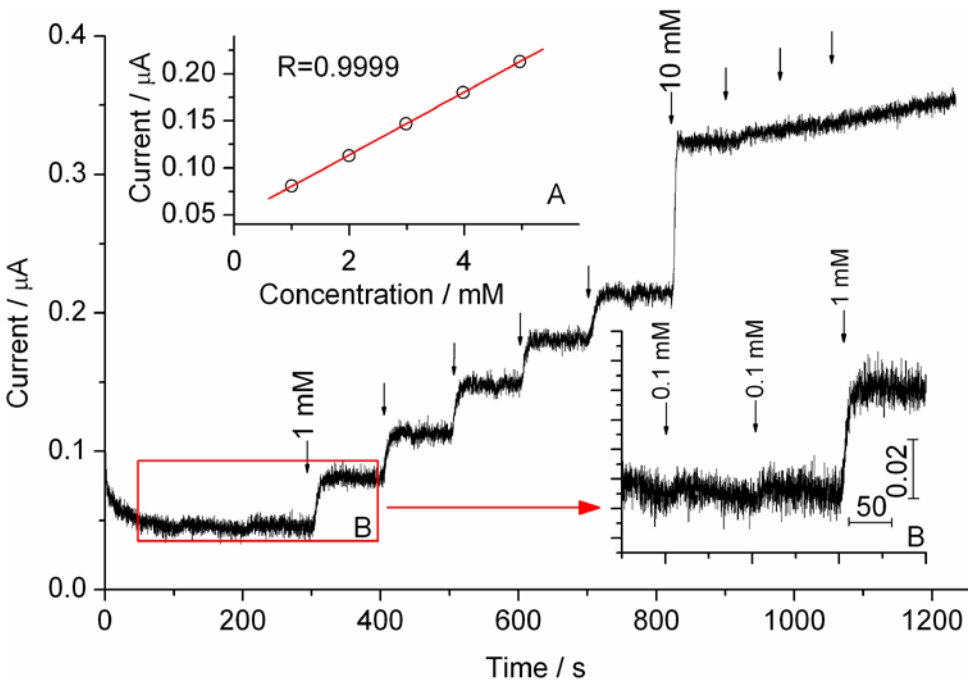

Figure 4-4. Current-time curve of Nafion-GOx-NCNCs modified GC electrode for successive addition of glucose (indicated by arrows with marked concentrations) to 50 mM pH=7.2 PBS at 0.50 V vs. Ag/AgCl. Inset A: calibration curve for glucose. Inset B: amplification of curve B.

The observed catalytic activity of NCNCs toward oxidation of H_2O_2, which is a reversed process to ORR where O_2 is reduced to H_2O_2, can be explained by the strong electronic affinity of the nitrogen atoms and the substantially high positive charge density on the adjacent carbon atoms.[30] These sites are favorable for the side-on O_2 adsorption, which could effectively weaken O-O bonding to facilitate ORR.[30] Furthermore, the unique structure of NCNCs can also contribute to the catalytic activity. Unlike N-doped carbon nanotubes or N-doped graphene, where N atoms are distributed along the whole surface, in NCNCs the nitrogen atoms are concentrated primarily on the basal edges of individual cups within the stacked fiber.[47] Such nitrogen enrichment might provide a higher density of catalytically active centers with low stereo hindrance for binding redox species. It has been recently proposed[155] that binding of the

reduction intermediate, OOH, on pyridinic edge sites in nitrogen-treated graphite is optimal for two-electron reduction of O_2 to H_2O_2.

Another possible explanation for the catalytic activity of NCNCs could be related to the presence of residual Fe catalyst in nanocups remaining from their CVD synthesis (Figure 4-9, Section 4.8 Supporting Information). Although we have observed no Fe peak in the CV of stacked NCNCs (Figure 4-1c), Fe was evident in the nanocups after they were physically separated and electrochemically purified (Figure 4-10a, Section 4.8 Supporting Information). We hypothesize that the residual iron can interact with nitrogen atoms, to form iron-porphyrin-like structures,[260] and such Fe/N/C electrocatalysts[171] can be responsible for ORR and H_2O_2 oxidation. The remained catalytic activity of separated nanocups toward ORR (Figure 4-10b, Section 4.8 Supporting Information) suggests that such activity should be the intrinsic catalytic property of NCNCs, no matter in separated or stacked forms. It has been previously shown[261] that the Fe species in N-doped carbon nanotubes could be dissolved and/or passivated during electrochemical potential cycling and were not the primary catalytically active site for ORR. However, similar treatment of NCNCs resulted in only a slight dissolution/passivation of the Fe (Figure 4-11 , Section 4.8 Supporting Information), indicating that Fe is bound more strongly in NCNCs and results in improved stability and catalytic activity as the Fe/N/C structure. Without completely ruling out the possible effect of Fe species,[129] both mechanisms might explain the electrocatalytic activity of NCNCs. Further studies are needed to reveal the exact mechanism of the catalytic activity of nitrogen-doped carbon nanomaterials.

4.5 CONCLUSIONS

In conclusion, we demonstrated that the stacked NCNCs have similar catalytic ability in ORR as Pt-CNTs and also could be used in the electrochemical detection of H_2O_2 and glucose. By comparison with commercial Pt-CNTs catalyst, the N-doped nanocups have shown the potential to replace the costly Pt-based catalyst in fuel cells and sensors.

4.6 ACKNOWLEGEMENT

This work was supported by the Pennsylvania NanoMaterials Commercialization Center through funding provided by DCED. We thank John Baltrus at the National Energy Technology Laboratory for access to the XPS instrumentation and Shigeru Amemiya for access to RRDE.

4.7 SUPPORTING INFORMATION

This supporting information contains Thermogravimetric Analysis (TGA) of commercial Pt-CNTs from Columbia Chemical Company (Figure 4-5), CVs of stacked NCNCs and Pt-CNTs (Figure 4-6), CV of stacked NCNCs to rule out Pt contamination (Figure 4-7), Amperometric response of Nafion-GOx-Pt-CNTs modified GC electrode for glucose detection (Figure 4-8), X-ray photoelectron spectroscopy of Fe high-res scan for NCNCs (Figure 4-9), CVs of separated NCNCs (Figure 4-10) and CVs of electrochemical treatment of separated NCNCs (Figure 4-11).

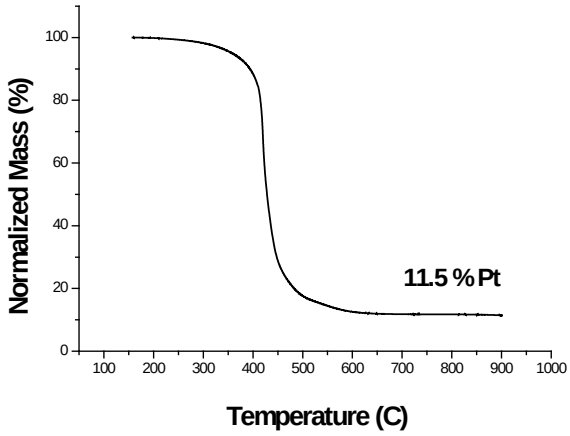

Figure 4-5. Thermogravimetric Analysis (TGA) of commercial Pt-CNTs from Columbia Chemical Company shows 11.5% Pt content.

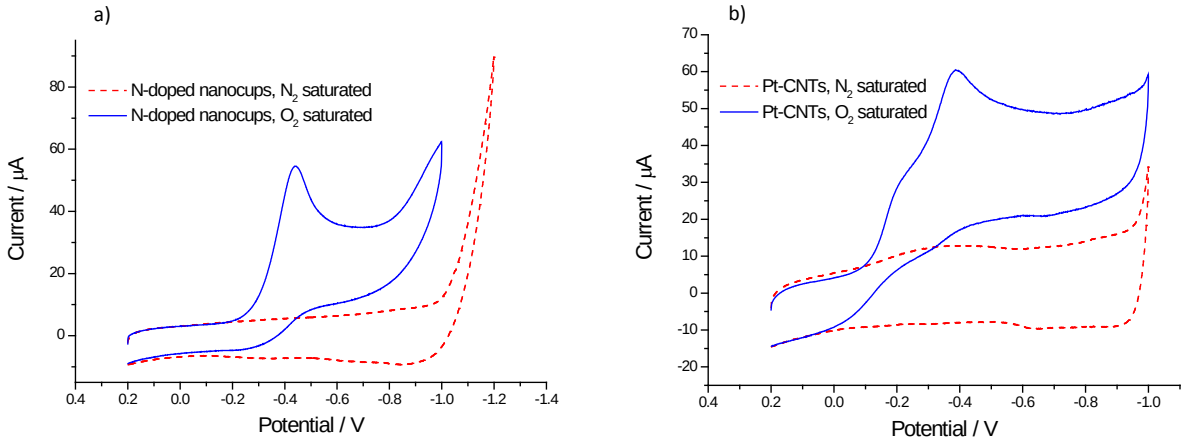

Figure 4-6. Cyclic voltammograms of (a) stacked NCNCs and (b) Pt-CNTs in 0.1M KOH solution saturated with N_2 (red, dash line) or O_2 (blue, solid line). The appearance of peaks around −0.4 V in O_2 saturated solution was attributed to oxygen reduction reaction (ORR).

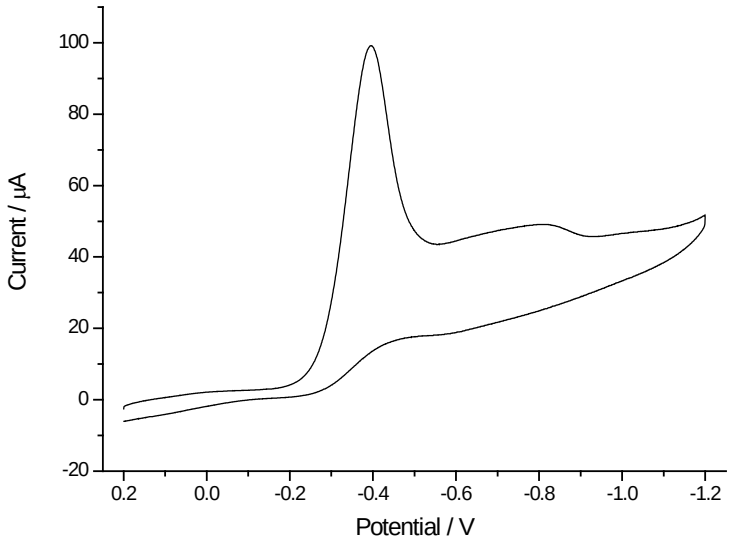

Figure 4-7. Cyclic voltammograms of stacked NCNCs in 0.1M KOH solution saturated with O_2 with a Cu foil as the counter electrode.

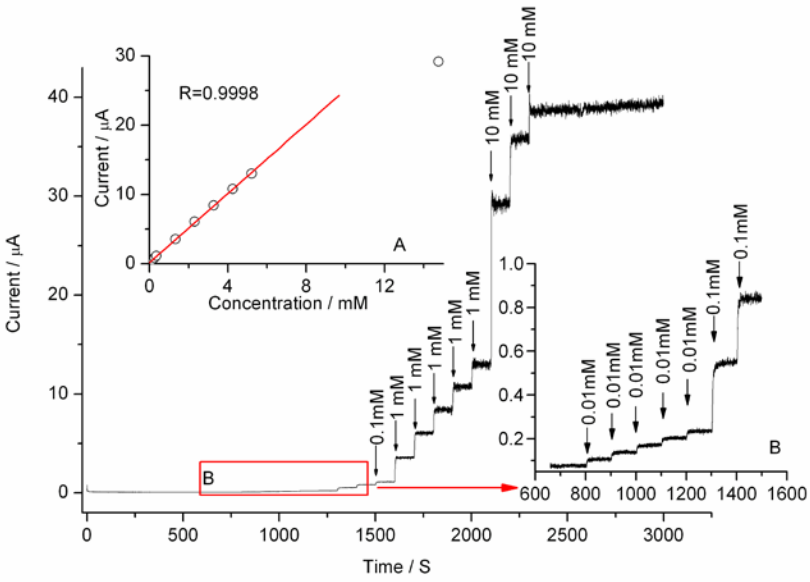

Figure 4-8. Current response of the Nafion-GOx-Pt-CNTs modified GC electrode for successive additions of glucose, indicated by arrows with marked concentrations to 50 mM pH=7.2 PBS at 0.50 V. Inset A: calibration curve for glucose. Inset B: expansion of the low concentration range.

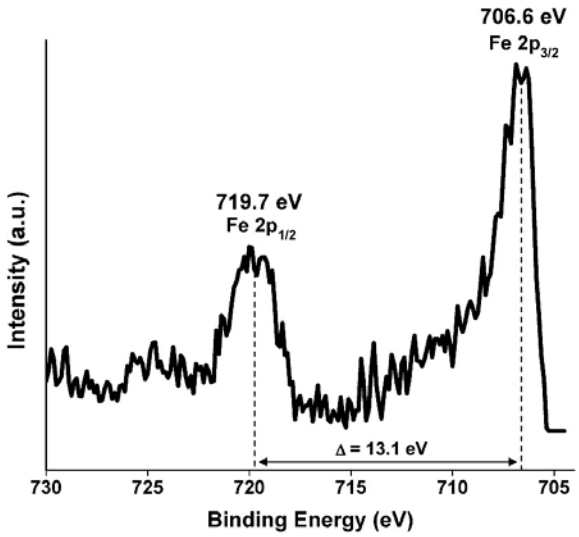

Figure 4-9. X-ray photoelectron spectroscopy (XPS) of the Fe 2p region of the NCNCs before electrochemical treatment, confirming the presence of Fe in the sample; binding energy was corrected using the Si 2p peak of the quartz substrate ate 103.4 eV as an internal standard and the reported spectrum is the average of 20 individual scans.

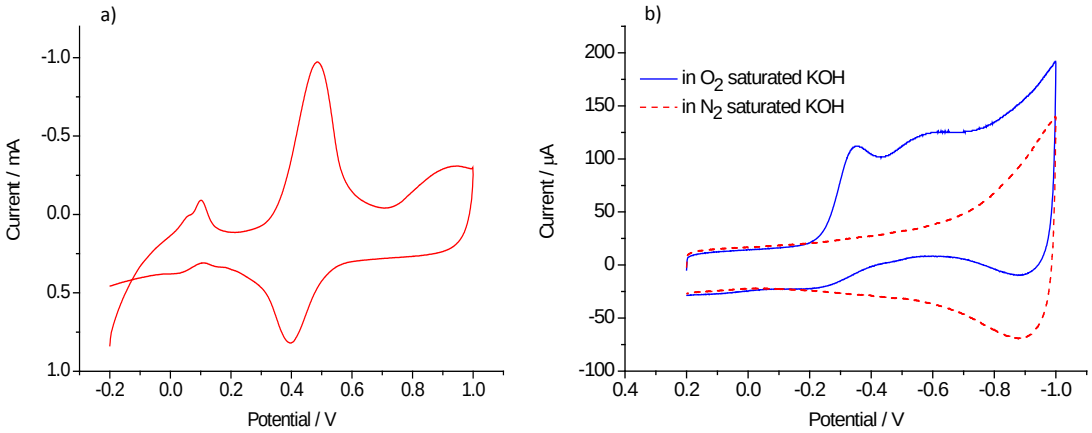

Figure 4-10. a) CV of separated NCNCs after bulk electrolysis in 0.5 M H_2SO_4; b) CVs of separated NCNCs in 0.1 M KOH saturated with O_2 (blue solid line) versus N_2 (red dashed line).

Stacked NCNCs were separated by grinding with a mortar and pestle in EtOH as described previously.[8] Then 1 mg of separated NCNCs was dissolved in 1 mL solvent mixture of Nafion (5%) and EtOH (V: V ratio = 1:9). After sonication for 0.5 h, 20 µL resulting solution

was drop-casted on a GC electrode. The modified GC electrode was then bulk electrolyzed in 0.5 M H_2SO_4 at 1.2 V for 500 sec in order to remove residual Fe catalyst. After the bulk electrolysis, the electrode was rinsed thoroughly with water and then CVs were measured in fresh 0.5 M H_2SO_4 at a scanning rate of 50 mV/s. Despite bulk electrolysis treatment, Fe^{3+}/Fe^{2+} redox pair at 0.486 V and 0.397 V was clearly observed. (The small peak around 0.1 V might be attributed to Fe^{2+}/Fe.) This observation indicates that Fe is strongly bound within NCNC. The separated nanocups still demonstrate electrocatalytic activity in ORR as evident from the appearance of broad peaks around −0.4 V under O_2 saturated condition in 0.1 M KOH solution versus N_2.

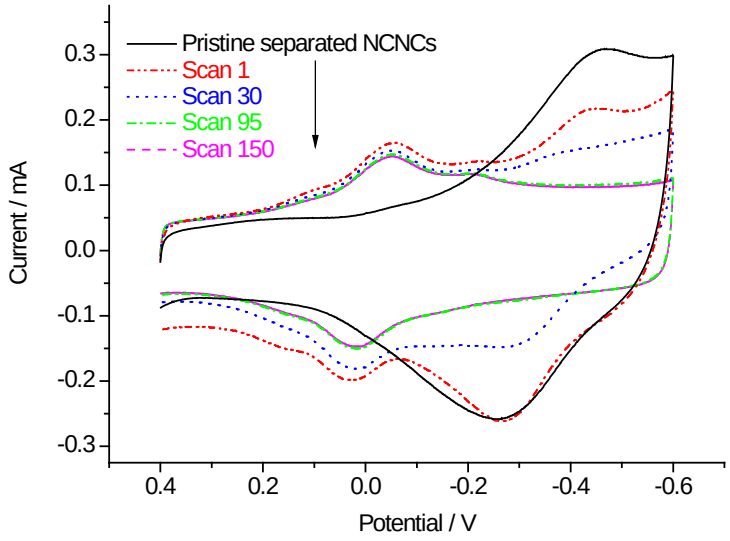

Figure 4-11. CVs of separated NCNCs before and after passivation treatment in 50 mM PBS. Black solid line: CV of pristine separated NCNCs before any treatment. Red dashed line: the first CV scan of sepatated NCNCs in PBS after bulk electrolysis at 1.2 V in 0.5 M H for 450s. Blue dotted line: the 30th scan. Greened line: the 95th scan. Magenta dashed line: the 150th scan.

The electrochemical treatment was done by first bulk electrolysis of the separated NCNCs modified GC electrode at 1.2 V in 0.5 M H_2SO_4 for 450 s, trying to oxidize the Fe species and dissolve them in acid. After complete rinse of the electrode with double distilled water, repeated cycling in 50 mM PBS was applied to dissolve/passivate the Fe. However, the bulk electrolysis only resulted in a decrease of reduction peak at −0.46V. Moreover, another redox peak pair appeared at −0.05V/+0.03V. After repeated CV scans, the peaks at −0.46V/−0.26 V further decreased and the newly appeared peaks stabilized after many scans. Such change of curve shape rather than complete passivation of Fe species as reported in literature[261] could be explained by the unique structure of NCNCs which makes the Fe species more strongly bound compared to nanotubes.

5.0 THE EFFECT OF METAL CATALYST ON THE ELECTROCATALYTIC ACTIVITY OF NITROGEN-DOPED CARBON NANOTUBE CUPS

5.1 CHAPTER PREFACE

We now learned in Chapter 4 that nitrogen-doped carbon nanotube cups demonstrated promising electrochemical catalytic activity towards ORR as compared to traditional Pt-based catalyst materials. However, the origin of the improved catalytic activity is still not quite clear. Nitrogen-doping, catalyst residue, complex of metal-N-C were all proposed as possible explanations. The aim of this chapter was to investigate the catalytic activity of NCNCs synthesized from different catalysts in order to gain some deeper understanding of such materials. Specifically, three NCNCs materials and their corresponding MWCNTs controls were synthesized from Fe, Ni or Co catalysts via CVD and their electrochemical performance for ORR were compared with each other and also the non-doped MWCNTs controls.

In this chapter, nitrogen-doped and un-doped carbon nanotubes (CNTs) were synthesized from ferrocene, nickelocene, and cobaltocene metal catalysts. Electrochemical testing for oxygen reduction reaction (ORR) showed that nitrogen-doped CNTs synthesized from ferrocene had improved catalytic activity while nanotubes synthesized from nickelocene and cobaltocene, doped with a comparable amount of nitrogen and having similar stacked-cups structure as nitrogen doped carbon nanotubes from ferrocene, had a performance only slightly better than that

of un-doped CNTs. Ferrocene-based nitrogen doped CNTs also demonstrated similar long term stability and higher CO tolerance compared to Pt/C catalyst. Detailed ORR mechanisms were also studied and carbon nanomaterials showed different ORR processes as a result of the metal catalyst utilized in the chemical synthesis. Nitrogen-doped and un-doped CNTs synthesized from nickelocene show a preferential 4-electron process as compared to materials synthesized from ferrocene and cobaltocene. We believe that the metal used in the growth process regulates the mechanism of oxygen reduction and can be used to develop improved nitrogen-doped carbon nanomaterials as non-precious-metal catalysts for fuel cells.

The material contained in this chapter was submitted as a research paper to the *Journal of Physical Chemistry C*.

List of Authors: Yifan Tang, Seth C. Burkert, Yong Zhao, and Alexander Star

Author contributions: All authors contributed to the design of experiments and writing of the paper. YT, SCB, YZ synthesized the NCNCs and MWCNTs materials using CVD. YT and SCB performed the TEM characterization. YT and YZ performed the SEM microscopic and EDX spectroscopic characterizations. YZ did the Raman spectroscopy characterization. YT and SCB carried out the electrochemical characterizations.

5.2 INTRODUCTION

Nitrogen-doped carbon nanomaterials have attracted a lot of attention in recent years because of their tailored electrical and electrochemical properties.[78-79, 256] They have been shown to be great candidates for substituting the expensive Pt-based catalysts in fuel cells for oxygen reduction reaction (ORR).[80, 143, 262] The doping of nitrogen into carbon nanomaterials, such as carbon nanotubes (CNTs) and graphene, was achieved through either in situ doping during the synthesis by introducing a nitrogen source in chemical vapor deposition (CVD)[31, 47, 80, 263-264] / pyrolysis[11, 30, 81-83, 265] process, or post-synthesis doping by chemical[84-85, 172] / electrochemical[86] functionalization. Among these different synthetic routes, some techniques such as CVD and pyrolysis may involve using transition metals,[266-270] which have well-known catalytic activity on their own[129] and might affect the electrochemical catalytic activity at above middle parts per million (ppm) range[97]. Although nitrogen-doped carbon nanomaterials prepared without using transition metals have shown some improved ORR performance,[143, 151, 154, 271-273] the best ORR catalysts reported to date in the literature in both acidic (half-wave potential: + 0.81 V)[98] and basic (half-wave potential: − 0.1V)[30] media were those synthesized using transition metal catalysts.

The debated effects of residual metal on the electrocatalytic activity of carbon nanomaterials have prompted the development of new metal-free electrocatalysts. Recent nitrogen-doped carbon nanomaterials prepared without the incorporation of transition metals have shown improved ORR performance, confirming the necessity of nitrogen doping for improved ORR catalytic activity in the absence of transition metals.[274-275] Graphitic[91, 95, 152-153] and pyridinic[154-155] nitrogen species are commonly recognized to be responsible for the ORR activity,[157-158] although sometimes the results are conflicting which might be due to the limited

number of studies in this field and the variation in experimental conditions.[276] Metal-free nitrogen-doped carbon nanomaterials have been further improved through co-doping with boron[180-181] or phosphorous,[175] which have lower electronegativities than both nitrogen and carbon. A similar conjugation of less electronegative transition metals with nitrogen functionalities could be used to explain the superior ORR catalytic activity of transition metal electrocatalysts as compared to metal-free electrocatalysts. Studies have shown that residual metal is often found bound to nitrogen species causing a metalloporphyrin-like active site,[11, 265] and subsequent removal of the metal causes a drop in catalytic activity and deviation from the preferred 4-electron ORR mechanism.[172] While the availability of nitrogen active sites is correlated to the potential of the material[277] the effects of different metals on the ORR mechanism that occurs at the active site have not previously been determined.

In this work, we synthesized nitrogen-doped CNTs using ferrocene, nickelocene or cobaltocene as catalysts which have a unique stacked cup structure previously reported as nitrogen containing nanotube cups (NCNCs)[47]. Unlike previous work, where only Fe catalyzed nitrogen doped CNTs created the stacked-cups structure,[278] all three synthesized nitrogen doped CNTs nanotubes formed the unique stacked-cups structure and will be denoted as NCNC[Fe], NCNC[Ni], and NCNC[Co] respectively. For comparison un-doped multi-walled carbon nanotubes (MWCNTs) were synthesized using ferrocene, nickelocene, or cobaltocene as catalysts (denoted as MWCNT[Fe], MWCNT[Ni], and MWCNT[Co] respectively). The stacked-cups structure achieved for all NCNCs allows for more accurate comparison of materials allowing for the effect of metal on the electrocatalytic activity to be accurately characterized. Electrochemical testing results demonstrated that NCNCs synthesized from ferrocene had improved ORR activity over un-doped MWCNTs synthesized from ferrocene and NCNCs

synthesized from nickelocene or cobaltocene in terms of the reduction half-wave potential and the current. On the other hand, NCNC[Ni] and NCNC[Co] only showed some improved catalytic activity compared to MWCNT[Ni] and MWCNT[Co]. The detailed ORR mechanisms for the abovementioned materials were also different: NCNC[Ni] and MWCNT[Ni] demonstrated almost a four-electron reduction ORR pathway, while NCNC[Fe], MWCNT[Fe], NCNC[Co], and MWCNT[Co] showed a combination of two-electron and four-electron mechanisms. The observed difference in their performance supports the hypothesis that through changing the metal catalyst utilized during material synthesis the mechanism for the ORR can be controlled. Such understanding is of great importance to the future design of non-precious-metal catalysts for low-cost fuel cells and other electrocatalytic applications.

5.3 EXPERIMENTAL SECTION

5.3.1 Materials

Pt/C sample was received from Columbia Chemical Company. All other chemicals of analytical grade or better were purchased from Aldrich-Sigma or Fisher Scientific and were used as received. All gases were purchased from Valley National Gases.

5.3.2 Preparation of Nitrogen-doped Carbon Nanotube Cups (NCNCs)

NCNCs were prepared using a slightly modified Chemical Vapor Deposition (CVD) method described in our previous report[47] using a three-zone Lindberg/Blue furnace and a 1” quartz tube.

Briefly, NCNCs were synthesized via CVD by injecting a liquid precursor consisting 0.75 wt% of metallocenes (ferrocene or nickelocene or cobaltocene, respectively), 10 wt% of acetonitrile, and 89.25 wt% of xylenes at a rate of 1 mL/h with carrier gases of Ar at 127 sccm and H_2 at 38 sccm. The first-zone of the furnace was used for metallocene evaporation at temperatures between 250 and 300°C and the growth was carried out in the second and third zone for 60 min at 800 °C for NCNC[Fe] and NCNC[Co], and 750°C for NCNC[Ni]. The NCNCs synthesized during different CVD runs were collected from a quartz plate placed in the quartz tube. As a control, un-doped MWCNTs were also synthesized with the same method using ferrocene, nickelocene, or cobaltocene as the catalyst without adding acetonitrile in the liquid precursor.

5.3.3 Characterization

Transmission electron microscopy (TEM) images were obtained with a Philips/FEI Morgagni microscope. The electron beam accelerating voltage of the TEM was held at 80.0 keV for all imaging. All NCNCs and MWCNTs samples were prepared by suspension in EtOH and drop-casted on a lacey carbon TEM grid (Pacific Grid-Tech) and by allowing the solvent to evaporate completely.

Scanning electron microscopy (SEM) and energy-dispersive X-ray (EDX) spectroscopy were performed with a Phillips XL30 FEG microscope equipped with an EDAX assembly.

X-ray photoelectron spectroscopy (XPS) was obtained with a Thermo Scientific K-Alpha X-ray photoelectron spectrometer using monochromated Al Ka x-rays as the source. The sample spot size was 400 μm. Charge compensation was provided by a low energy electron source and Ar^+ ions. Survey scans were collected using a pass energy of 200 eV and high resolution scans had a pass energy of 50 eV.

Raman spectra were taken on Reinshaw inVia Raman microsope with an excitation wavelength of 633 nm. NCNC and MWCNT samples were drop-casted on a quartz slide and dried. Spectra were scanned from 800 to 2000 cm^{-1} at 10% laser intensity with 10 s exposure time.

5.3.4 Electrode Preparation

Glassy carbon (GC) electrode (CHI 104, GC area 0.0707cm^2, total area 0.196 cm^2) or rotating ring-disk electrode (Pine AFE7R9GCPT, GC disk area 0.2475 cm^2) were carefully polished with gamma alumina powder (0.05 micron, CH Instruments) until a mirror finish was obtained. Then the electrode was rinsed and sonicated with plenty of double distilled water to remove any alumina residues and finally dried under N_2. Catalyst ink was made by dissolving 1 mg of NCNCs or MWNTs or Pt/C sample in a solvent mixture of 992 μL of ethanol and 8 μL of 5% Nafion by sonication for at least 30 minutes to give a concentration of 1 mg/mL and 0.04 % Nafion. 20 μL of catalyst ink was then dropcasted on the GC electrode or the GC part of RRDE and allowed to air dry.

5.3.5 Electrochemical Characterization

Cyclic voltammetry (CV), rotating ring-disk electrode (RRDE) voltammetry, linear sweep voltammetry (LSV) and chronoamperometry measurements were performed using a CHI 7042 Bipotentiostat (CH Instruments, Austin, TX). A Pt wire electrode (CHI 115) and an Ag/AgCl (CHI 111, 1 M KCl) electrode were used as the counter and reference electrode, respectively. All potentials are reported versus the reference electrode. The electrodes were purchased from CH

Instruments, Austin, TX. The RRDE was purchased from Pine Instrument Company (AFE7R9GCPT; reported collection efficiency, N = 0.37) contained a GC disk and Pt ring electrode. The RRDE experiments were carried out on a MSR Electrode Rotator.

Before electrochemical testing, the working electrodes were first treated by bulk electrolysis in 50 mM phosphate buffer solution (pH = 7.2) at 1.7 V to remove any bulk metal catalyst residue and activate the electrode materials, followed by thoroughly rinsing with double distilled water. Double layer capacitance measurements were conducted after the activation in PBS. For RRDE voltammetry, LSV was performed using modified RRDE in O_2 saturated 0.1 M KOH solution at a scan rate of 0.05 V/s and rotating speed of 1400 revolutions per minute (rpm) while the Pt ring was polarized at 0.5 V for oxidizing H_2O_2. The tests were repeated at least three times to confirm the reproducibility of the process. The collection efficiency of RRDE was confirmed by testing in 10 mM $K_3Fe(CN)_6$ solution with 0.5 M KNO_3 as the supporting electrolyte.

Chronoamperometric measurements were done using a three-electrode configuration in O_2 saturated 0.1 M KOH solution with the catalyst ink modified rotating electrode held at −0.5 V with a rotating speed of 1000 rpm. CO poisoning effect tests were performed in a three-electrode configuration, while a 112 sccm O_2 flow was continuously bubbled into the solution and a 26 sccm CO flow (19%) was introduced into the O_2 flow at 200 s.

5.4 RESULTS AND DISCUSSION

NCNCs, also named nanobells,[258] have been synthesized using a slightly modified CVD method according to previously published procedure.[47] Briefly, as depicted in Figure 5-1a, floating

catalyst CVD was performed at 800 °C or 750 °C under the carrier gases of Ar and H_2 with xylenes as the carbon source and 10% acetonitrile as the nitrogen source. It should be noted that the difference in CVD temperature for NCNC[Ni] was due to quality and quantity of the resulting structure. NCNC[Ni] grown at 800°C did not readily form the stacked-cups structure ultimately resulting in a low yield of product (Figure 5-5, in Section 5.8 Supporting Information). Ferrocene, nickelocene or cobaltocene were used as catalysts to synthesize NCNCs from the corresponding transition metals. The products were denoted as NCNC[Fe], NCNC[Ni] and NCNC[Co], respectively. We chose metallocenes as metal catalysts to achieve consistent CVD synthesis conditions in order to compare the effect of the metal on the ORR performance of NCNCs.

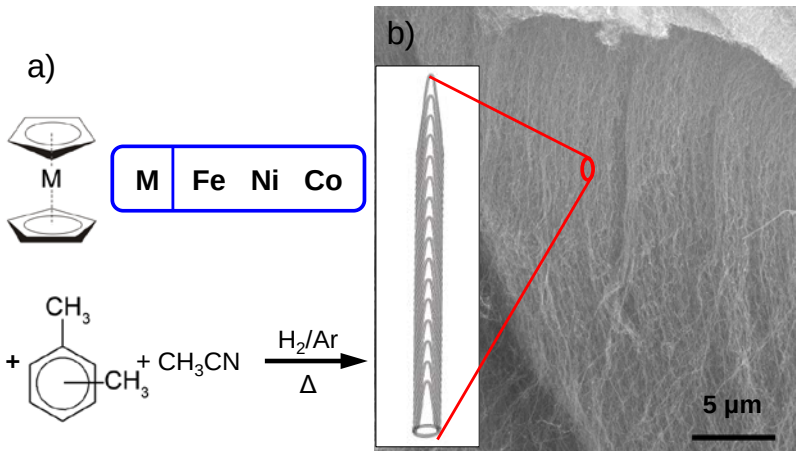

Figure 5-1. a) Chemical vapor deposition (CVD) synthesis of nitrogen-doped carbon nanotube cups (NCNCs) from a mixture of xylenes and acetonitrile with ferrocene or nickelocene or cobaltocene catalysts; b) a scanning electron microscopy (SEM) image for the as-grow vertically aligned NCNCs from ferrocene catalyst; inset: a schematic illustration depicting the structure of NCNCs.

A few publications[82, 278] focused on the different catalysts for nitrogen-doped CNTs and their effects on ORR. Unlike the previous report,[278] stating that only Fe catalyst tends to form

bamboo or stacked-cups structure whereas Co or Ni catalysts form straight hollow tube structure, in our synthesis all three catalysts produced NCNCs with well-defined stacked-cups structure as observed by transmission electron microscopy (TEM) (Figure 5-2 b,d,f). The well-defined stacked-cups structure for all three materials can be attributed to the floating catalyst CVD method by liquid injection as compared to the fixed-bed CVD in the above mentioned report. Previous reports[82, 278] rely on transition metal catalyst deposited on alumina or silica substrate, where the stacked-cups structure can only occur with Fe catalysts due to the formation of stable metal carbides at the Fe particle surface. The formation of iron carbides around the surface of the Fe particle produces a graphitic envelope which eventually slides off the particle revealing a fresh Fe surface for the graphitic envelope to reform. This subsequent reforming of the graphitic envelope causes a sputtered growth resulting in the stacked-cups structure.[278] Nickel and cobalt however do not form stable metal carbides and the graphitic envelope is not produced in their solid substrate synthesis. However, the CVD results would be quite sensitive to the growth conditions. Similar bamboo-like growth results for CNT were also observed on Ni nanoparticles by Foo and others.[279] In our experiment, through liquid injection the catalyst particles are more evenly dispersed throughout the carbon source allowing for graphitic envelope formation resulting in the stacked-cups structure. As shown in Figure 5-2, all NCNCs from different catalysts had similar structure with a diameter around 25-50 nm and a length in μm range. X-ray photoelectron spectroscopy (XPS) analyses (Figure 5-6, in Section 5.8 Supporting Information) were done for all three samples, showing similar nitrogen content showing similar nitrogen content around 1.0 at% (Table 5-1). The quality of NCNC[Co] was relatively low as we can observe some hollow structures in the TEM image (Figure 5-2f). Non-doped MWCNTs were also synthesized using ferrocene, nickelocene, and cobaltocene as the catalyst (denoted as

MWCNT[Fe], MWCNT[Ni], and MWCNT[Co] respectively), keeping all other parameters constant except not using the nitrogen source (acetonitrile). The TEM images in Figure 5-2a,c,e show hollow tube structures with similar diameter to the NCNCs. MWCNTs synthesized from the same metal catalyst as the NCNCs act as a better control than commercial MWCNTs which typically contain different metal catalyst residues and are synthesized via different methods. NCNCs will be compared to their MWCNTs counterparts to more accurately depict the effect of nitrogen doping and metal catalysts on the ORR catalytic activity.

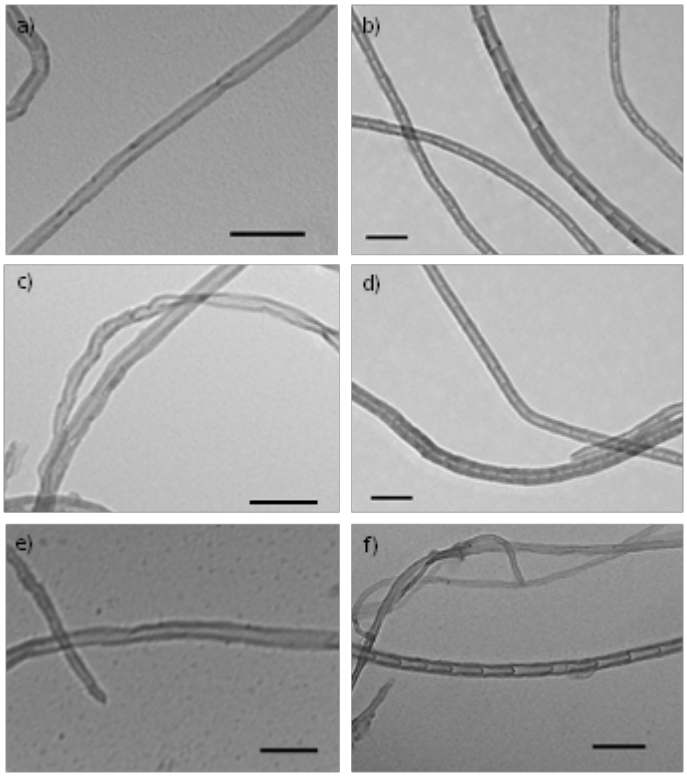

Figure 5-2. Transmission electron microscopy (TEM) images of a) MWCNT[Fe], b) NCNC[Fe], c) MWCNT[Ni], d) NCNC[Ni], e) MWCNT[Co], f) NCNC[Co]. All scale bars are 100 nm.

Although all NCNCs exhibited similar structures, it is necessary to mention that there were differences in the yield of products. When using ferrocene, we can achieve dense, vertically aligned growth, forming a thick (>30 μm) mat of NCNCs as demonstrated by scanning electron microscopy (SEM) in Figure 5-1b. The yields of NCNC[Ni] and NCNC[Co] (~0.5 mg) were less

than that of NCNC[Fe] (>5 mg) because of the relative instability of nickelocene and cobaltocene[280] in the precursor. The relative instability of nickelocene and cobaltocene also affected the growth process of MWCNTs causing lower yields of MWCNT[Ni] and MWCNT[Co] than that of MWCNT[Fe].

Table 5-1. Nanomaterials catalytic activity towards oxygen reduction reaction (ORR).

	n[a]	Half-wave Potential / V[b]
NCNC[Fe]	**2.6 ± 0.1**	**-0.297 ± 0.006**
NCNC[Ni]	**3.9 ± 0.1**	**-0.334 ± 0.003**
NCNC[Co]	**3.1 ± 0.2**	**-0.316 ± 0.008**
MWCNT[Fe]	**2.6 ± 0.1**	**-0.358 ± 0.026**
MWCNT[Ni]	**3.8 ± 0.1**	**-0.351 ± 0.002**
MWCNT[Co]	**2.7 ± 0.1**	**-0.343 ± 0.004**
Pt/C	**4.0 ± 0.1**	**-0.174 ± 0.006**

a) transferred electron number (n) per oxygen molecule was calculated, from RRDE, according to equation 1 at −0.5 V; b) half-wave potential was calculated based on the ORR current at –0.5V during RRDE versus a 1.0 M Ag/AgCl reference electrode (+0.235 versus the Standard Hydrogen Electrode). All trials were done in triplicates with the mean and standard deviation reported in the table.

The above-mentioned materials were made into a catalyst ink and drop-casted on the glassy carbon electrode as shown in the SEM images (Figure 5-7, in Section 5.8 Supporting Information). The corresponding energy-dispersive X-ray spectroscopy (EDX) results of the films right after drop-casting demonstrated the presence of metal residue in NCNCs and MWNTs from the CVD synthesis process. All NCNC and MWCNT samples had a metal/carbon atomic ratio between 0.1% and 0.3% (Figure 5-7, in Section 5.8 Supporting Information),

indicating similar residual metal between all samples. The metal/carbon atomic ratio of Co in MWCNT[Co] was significantly higher than all the other materials, this is most likely a result of metal aggregation once again tied to instability of the precursor. The electrochemical activation process would remove a large quantity of the bulk metal catalyst not incorporated into the MWCNT[Co]. The removal of bulk metal residue has been shown previously not to affect the intrinsic catalytic activity of carbon nanomaterials.[281] Raman spectroscopy was performed in order to determine the D/G ratio and relative defect density of the samples. MWCNTs all had a D/G ratio between 0.6 and 0.8 while NCNCs saw a higher D/G ratio between 1.1 and 1.2 (Figure 5-8, in Section 5.8 Supporting Information). This increase in D/G ratio is expected as the incorporation of nitrogen into the tube structure allows for more defect sites which also act as the active sites for the material. After the electrochemical activation process (Figure 5-9, in Section 5.8 Supporting Information, also showing the reproducibility), the peak potential for ORR of NCNCs was substantially enhanced compared to the pristine materials. The amount of metal residue is low and cannot be detected by EDX or XPS after the activation, but there were obvious differences in the ORR performance of the activated NCNCs, and we should not neglect the possible effect of metal catalysts residues as they might still affect the electrochemical catalytic activity at above middle-ppm range.[97]

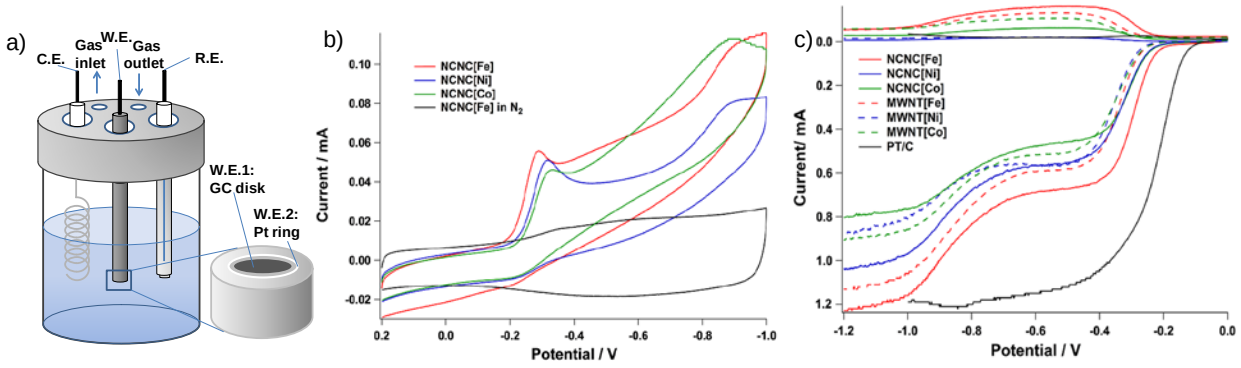

Figure 5-3. a) Schematic illustration of electrochemical cell used in ORR measurements; W.E.: working electrode, C.E.: counter electrode, R.E.: reference electrode, GC: glassy carbon. b) Cyclic voltammograms of NCNC[Fe] (black), NCNC[Ni] (red) and NCNC[Co] (blue) in O_2 saturated 0.1 M KOH solution and NCNC[Fe] (grey) in N_2 saturated 0.1 M KOH solution demonstration the oxygen reduction reaction (ORR) peaks; c) Rotating ring-disk electrode (RRDE) voltammograms of NCNC[Fe] (black), NCNC[Ni] (red), NCNC[Co] (blue), MWNTs (pink), Pt/C (green) for ORR in 0.1 M KOH at the rotating speed of 1400 rpm. The Pt ring electrode was held at + 0.5 V.

The electrochemistry testing set-up is shown in Figure 5-3a. ORR was studied using the above-mentioned materials as catalysts via cyclic voltammetry and rotating ring-disk electrode (RRDE) voltammetry in O_2 saturated 0.1 M KOH solution. Figure 5-3b showed the cyclic voltammograms of the NCNC[Fe], NCNC[Ni] and NCNC[Co] for ORR in 0.1M KOH solution. Comparing to the CV curve of NCNC[Fe] in N_2 saturated solution, clearly ORR peaks were demonstrated in the O_2 saturated solution. We can also observe a trend of different performance of the electrocatalysts in ORR: NCNC[Fe] > NCNC[Ni] > NCNC[Co], in terms of both peak potentials and peak current. The relative electrochemical active surface areas of the materials were estimated by comparing the double layer capacitance values from CV results in PBS (Figure 5-10, in Section 5.8 Supporting Information). The obtained relative surface areas (Table 5-2, in Section 5.8 Supporting Information) followed the same trend of NCNC[Fe] > NCNC[Ni]

> NCNC[Co]. Although for the resulting normalized current per active surface area, NCNC[Fe] was smaller than the other two materials, it is the current (density) per electrode geometry surface area or per mass that is more important for the material performance in fuel cells.

To further study the ORR process, we then conducted RRDE voltammetry to test all the materials. As shown in Figure 5-3c, though not as good as commercial Pt/C catalyst, NCNC[Fe] has an improved catalytic activity towards ORR compared to NCNC[Ni], NCNC[Co] and MWNTs in terms of both half-wave potential (Table 5-1) and reduction current. This relative performance agrees with the aforementioned CV results. Although all three NCNCs samples had similar nitrogen content (Table 5-1), compared to NCNC[Fe], NCNC[Ni] and NCNC[Co] were only slightly better than their un-doped controls - MWCNT[Ni] and MWCNT[Co] for the ORR half-wave potential. Due to the similar nitrogen content, metal catalyst/carbon ratio, and defect densities in NCNC[Fe], NCNC[Ni] and NCNC[Co] the difference in half wave potential must originate from the identity of the metal catalyst used in the synthesis procedure and not strictly the doping of nitrogen into the sp^2 carbon lattice structure.

It is highly possible that the active transition metal and nitrogen can form complex structures[98, 171, 282] analogous to metal porphyrins which account for the improved ORR activity. Among different metalloporphyrin-based materials tested as ORR catalysts, iron-porphyrins are more active than nickel-porphyrins.[283] And more recently, direct HRTEM and EELS imaging results suggested a positive correlation on the close spatial relations between iron and nitrogen atoms, which could be the Fe-porphyrins like active sites.[172] Although similar imaging studies with Ni and Co have not been performed, we can hypothesize that Ni and Co would also readily form Ni-porphyrin like and Co-porphyrin like active sites. These proposed structures may

explain our results for NCNCs and could be also supported by theoretical calculations[284-285] demonstrating that the nitrogen doped structures have higher binding energy towards Fe. Changes in oxidation state of metals incorporated in a metal-porphyrin structures has been known to alter the binding energy of the active site[286] thus altering the turnover rate of the catalytic reaction.[287] This same concept can be applied to changing the identity of the metal bound to the nitrogen active site of NCNCs as one possible explanation for the difference in half-wave potential between NCNCs of similar nitrogen content synthesized from different metals. Admittedly, the electrocatalytic properties of NCNC[Fe] were inferior to the commercial Pt/C, which may be due to the relatively low nitrogen concentration (~1%) and iron concentration (<0.2%) in our material, as some studies have demonstrated a positive correlation between the nitrogen concentration[267, 277] or iron doping[288-289] and the ORR activity.

Furthermore, detailed ORR mechanism could be investigated through the RRDE results by calculating the transferred electron number (n) per oxygen molecule, using the following equation:

$$n = 4I_D/(I_D+I_R/N) \qquad (5\text{-}1)$$

where I_D is the faradaic disk current, I_R is the faradaic ring current, and N = 0.37 is the collection efficiency (calibrated and is consistent with reported value by manufacturer). An n value of 4 corresponds to a complete four-electron reduction process from O_2 directly to H_2O while an n value of 2 implies a two-electron reduction process from O_2 to H_2O_2.

Interestingly, as showed in Table 5-1 and also can be observed in Figure 5-3c in the ring current portion, NCNC[Ni] and MWCNT[Ni] had high n values of 3.9 ± 0.1 and 3.8 ± 0.1, almost exclusively a four-electron process similarly observed for Pt/C, with little H_2O_2 detected. This value is significantly higher than the n values reported for some nickel phthalocyanine-

based electrocatalysts in the literature.[290] MWCNT[Ni] were not expected to have a highly selective process due to the absence of nitrogen functionalities in the material. One possible explanation for the unusual activity is the incorporation of Ni into naturally occurring defects in the MWCNT[Ni]. Although the ORR mechanism is selective for the four-electron process, due to the choice of metal, the limited availability of active sites to bind metal limits the half-wave potential of the material supporting the hypothesis that the number of active sites dictates the half-wave potential while the bound metal affects the mechanism that occurs at each active site. On the other hand, NCNC[Fe], MWCNT[Fe], NCNC[Co] and MWCNT[Co] all exhibited a mixed process of four-electron and two-electron processes. Similarly, NCNC[Fe] and MWCNT[Fe] had similar *n* values as did NCNC[Co] and MWCNT[Co] which strengthen the assumption that the metal bound to the active site dictates what type of mechanism occurs (the larger variation between NCNC[Co] and MWCNT[Co] could be explained by the poor quality of those samples from the instable cobaltocene catalyst). Based on these results we can hypothesize that the different ORR mechanisms are strongly correlated with different metal catalysts and the resulting metal-nitrogen-carbon hybrid active sites given the fact that all NCNCs had a similar nitrogen and metal concentration. To confirm our hypothesis and ensure that Pt-contamination from the counter electrode was not responsible for the improved catalytic activity of NCNC[Ni] and MWCNT[Ni], RRDE of those samples was performed against a graphite counter electrode (Figure 5-11). As can be seen both materials still have a negligible ring current and a resulting electron transfer number of 3.9 confirming that the improved catalytic activity does not result from Pt contamination.

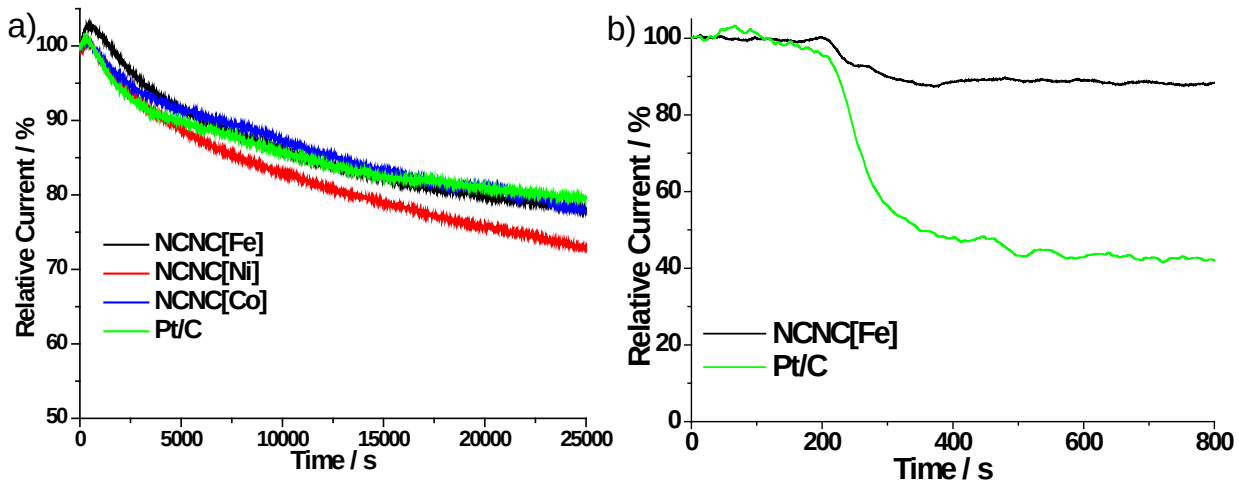

Figure 5-4. a) The chronoamperometric responses for NCNC[Fe](black), NCNC[Ni](red), NCNC[Co](blue) and Pt/C(green) on rotating electrode at 1000 rpm for oxygen reduction reaction in 0.1 M KOH at −0.5 V; b) CO poisoning effect tests for NCNC[Fe] and Pt/C. A 26 sccm CO flow (19%) was introduced into a 112 sccm O_2 flow at 200 s.

ORR stability tests for NCNC[Fe], NCNC[Ni], NCNC[Co] and Pt/C modified electrodes were conducted at steady state by measuring the chrono-amperometric responses (i-t curve) of the catalyst materials at the rotating electrode at 1000 rpm. As shown in Figure 5-4a, NCNC[Fe] and NCNC[Co] had similar stability compared to Pt/C, while NCNC[Ni] had a slightly larger decrease in the relative current. It is worth mentioning here that we also did stability tests using regular glassy carbon electrodes (Figure 5-12, in Section 5.8 Supporting Information). NCNC[Fe] had the best performance with the smallest relative current drop compared to other NCNCs and Pt/C. In this case, diffusion on the electrode also affects the current which is also the concern in actual fuel cell setup.[291] Furthermore, as we discussed in the ORR mechanism part, NCNC[Fe] when held at – 0.5 V for the stability testing could produce a large amount of H_2O_2 which might oxidize normal porous carbon catalyst support in fuel cell electrode. However NCNC[Fe] under such condition showed good stability which makes them a promising materials

for fuel cell applications. And the stability of NCNCs is also consistent with our previous degradation study, demonstrating that NCNCs were stable for as long as 80 days of incubation in a Fenton oxidation environment (1×10^{-4} M $FeCl_3$ and daily addition of 800 μM H_2O_2). [292]

Since NCNC[Fe] was identified as the best ORR catalysts among studied NCNCs, CO poisoning effect for NCNC[Fe] and Pt/C was examined by introducing CO into the electrolyte at 200 sec while holding the working electrode at – 0.5 V. As evident from Figure 5-4b, Pt/C was poisoned by CO while NCNC[Fe] remained unaffected. The slight drop of relative current for NCNC[Fe] could be explained by the decrease of O_2 partial pressure.

5.5 CONCLUSIONS

This information is critical to the next step in ORR catalyst development. The mechanism of this material can now be controlled during synthesis to yield materials that have an electron transfer number comparable to platinum. This concept could also be applied to other synthesis procedures of carbon nanomaterials in order to selectively control their electron transfer number towards improvement of ORR electrocatalysts. The future direction of this project is to develop NCNC[Ni] with higher nitrogen content in order to provide enough active sites to increase the ORR peak potential closer to that of commercial Pt catalysts. With the preferential four electron transfer number determined by the Ni metal catalyst and the increased peak potential from additional nitrogen active sites, this material could show comparable activity to commercial Pt catalysts.

In summary, NCNCs with stacked-cups structure were synthesized successfully from ferrocene, nickelocene and cobaltocene catalysts using CVD method. By comparing the ORR

performance of NCNC[Fe], NCNC[Ni], and NCNC[Co] as well as MWCNT[Fe], MWCNT[Ni], MWCNT[Co] and Pt/C, we have shown that NCNC[Fe] had significantly enhanced catalytic activity while NCNC[Ni] and NCNC[Co] only demonstrated activity slightly better than un-doped MWCNTs. We believe that the active site in this material is analogous to a metal-nitrogen-carbon structure where the number of active sites in the material is correlated to the half-wave potential and the identity of the metal determines the mechanism that occurs at each active site. This is supported by the almost four-electron process of NCNC[Ni] and MWCNT[Ni] while NCNC[Fe] and MWCNT[Fe] (having similar *n* values), together with NCNC[Co] and MWCNT[Co] (having similar *n* values) possessed a combination of two-electron and four-electron processes. Furthermore, NCNC[Fe] demonstrated similar chronoamperometric stability and much higher CO tolerance compared to commercial Pt/C catalysts. These findings are of great importance for tailoring the properties of non-precious-metal catalysts for future low-cost fuel cells.

5.6 ACKNOWLEDGEMENT

This work was supported by NSF career award No. 0954345. Y. T. and Y. Z. acknowledge a graduate student fellowship through Bayer MaterialScience. We thank the Department of Biological Sciences and the Department of Materials Science and Engineering at the University of Pittsburgh for access to the TEM and SEM instrumentation. We also thank RJ Lee Group, Inc. for the help in XPS testing.

5.7 SUPPORTING INFORMATION

This supporting information contains TEM of NCNC[Ni] at different temperatures(Figure 5-5); XPS spectra of NCNC[Fe], NCNC[Ni] and NCNC[Co] (Figure 5-6); SEM images of electrode materials (Figure 5-7); Raman spectroscopy of the electrode materials(Figure 5-8); cyclic voltammograms for electrochemical activation process (Figure 5-9), double layer capacitance measurements (Figure 5-10); RRDE voltammetry for NCNC[Ni] and MWCNT[Ni] using graphite counter electrode(Figure 5-11); chronoamperometric responses of NCNCs under non-steady-state condition (Figure 5-12) and table for relative electrochemical active surface areas and normalized ORR currents (Table 5-2).

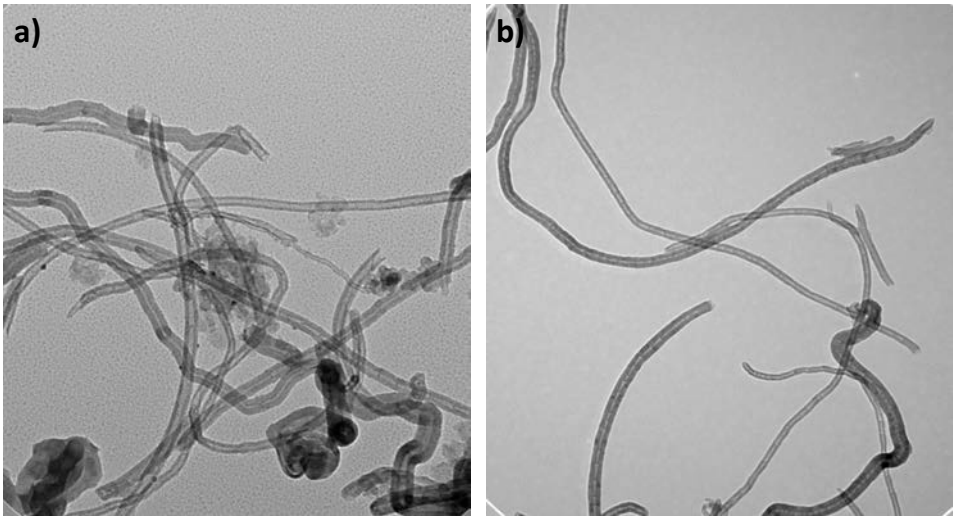

Figure 5-5. a) SEM image of NCNC[Ni] grown at 800°C, illustrating the poor quality of the desired stacked-cups structure; b) SEM image of NCNC[Ni] grown at 750°C, illustrating the improved quality of sample and achieved stacked-cups structure. Both scale bars are 100nm.

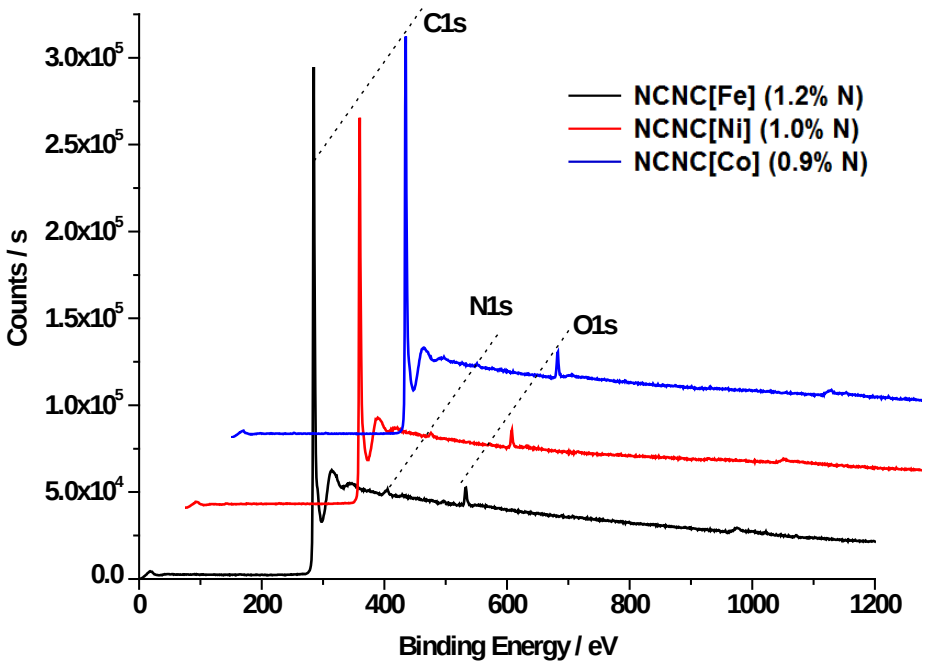

Figure 5-6. X-ray photoelectron spectroscopy (XPS) survey spectra for NCNC[Fe] (black), NCNC[Ni] (red) and NCNC[Co] (blue); nitrogen content, as determined by XPS, is contained within the legend.

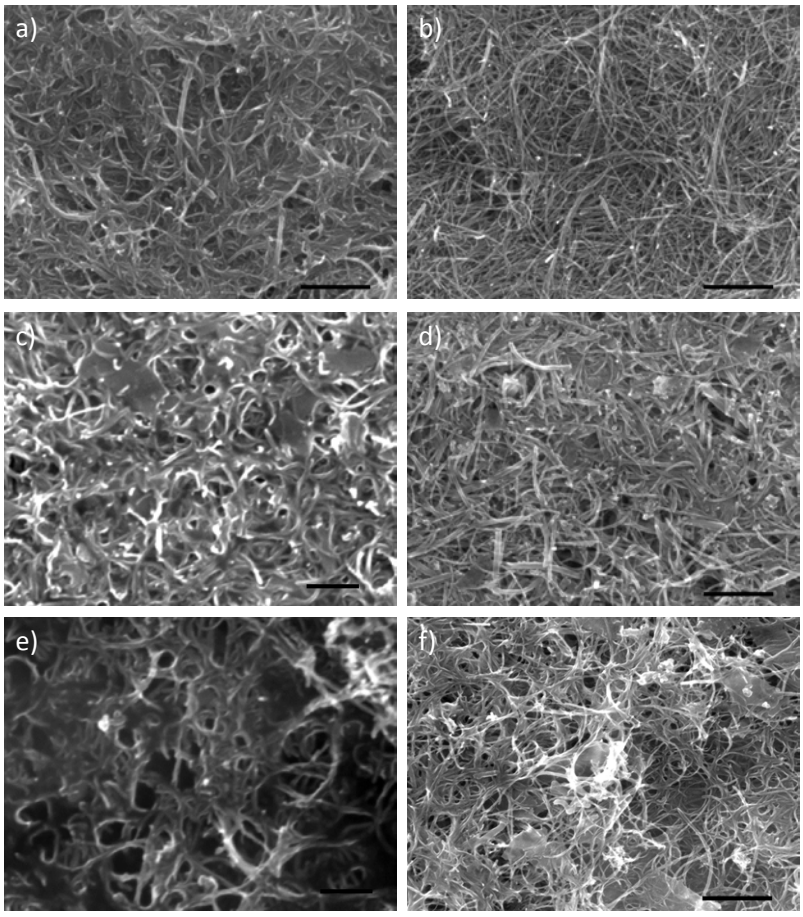

catalyst metal/carbon ratio	
MWCNT[Fe] 0.16 %	NCNC[Fe] 0.16 %
MWCNT[Ni] 0.14 %	NCNC[Ni] 0.15 %
MWCNT[Co] 0.27 %	NCNC[Co] 0.09 %

Figure 5-7. Scanning electron microscope (SEM) images of a) MWCNT[Fe], b) NCNC[Fe], c) MWCNT[Ni], d) NCNC[Ni], e) MWCNT[Co], and f) NCNC[Co] catalyst films drop-casted from the corresponding catalyst ink. All scale bars are 1 µm. The table gives the catalyst metal/carbon ratio for each sample as determined by energy-dispersive X-ray spectroscopy (EDX).

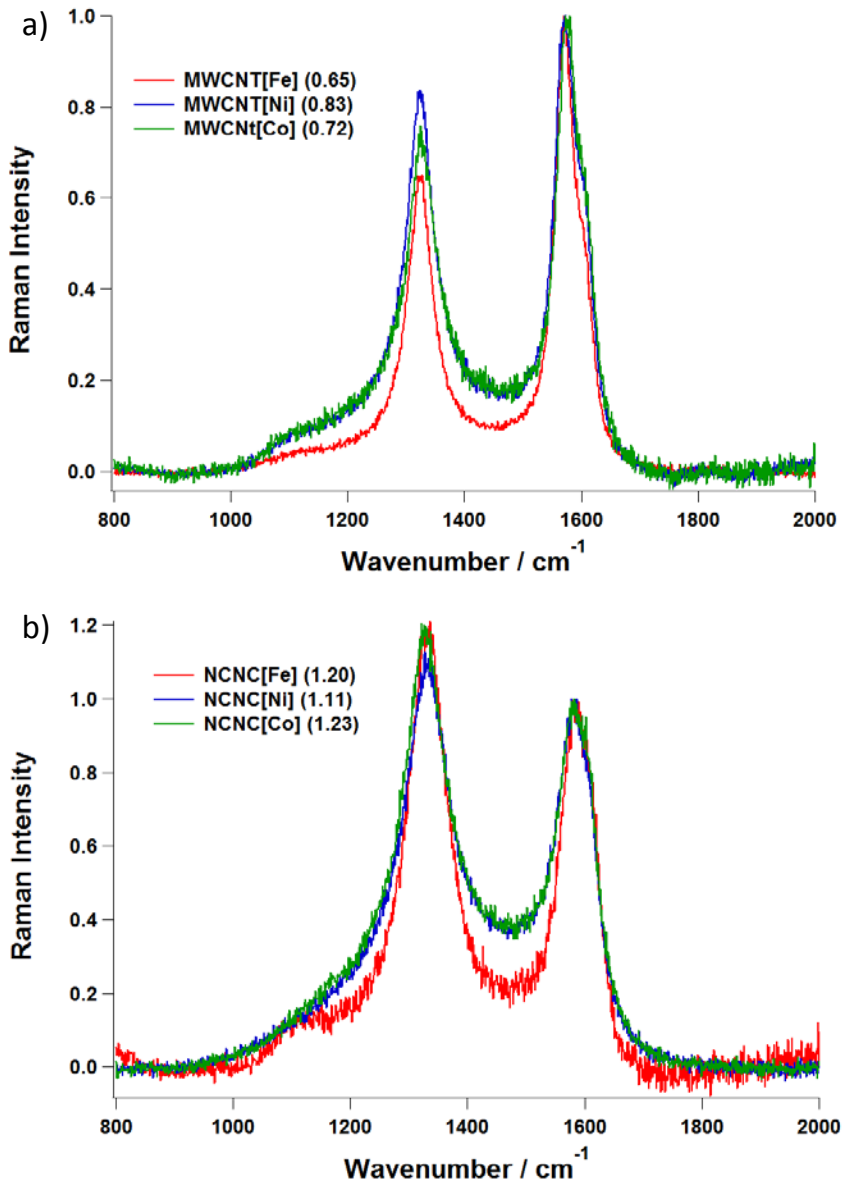

Figure 5-8. Raman spectra of a) MWCNTs, and b) NCNCs normalized to the G peak, with the D/G ratio for each material in parenthesis.

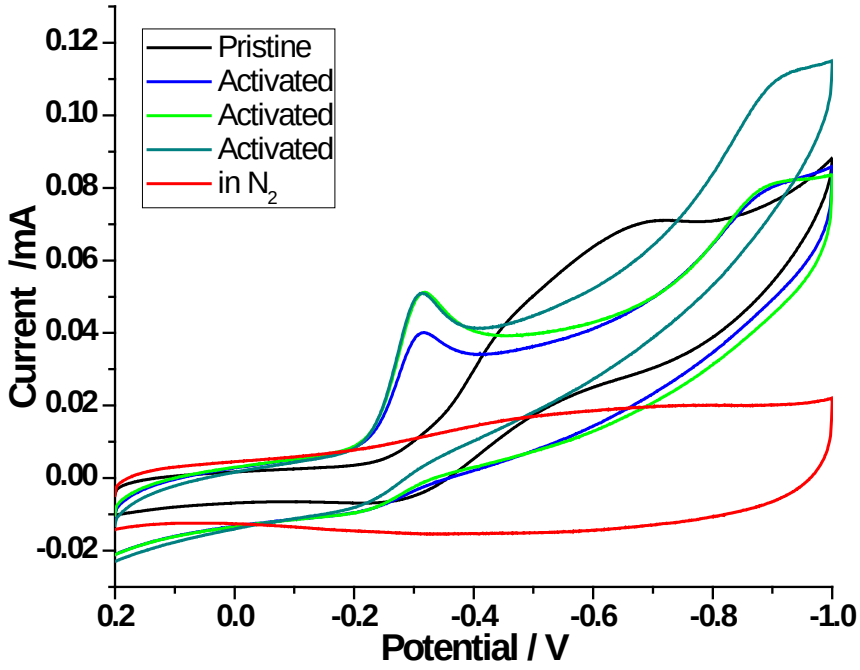

Figure 5-9. Cyclic Voltammetry (CV) curves of pristine NCNC[Ni] (black) for oxygen reduction reaction in O2 saturated 0.1 M KOH showing a poor ORR performance before activation; three different electrodes of NCNC[Ni] after electrochemical activation (blue, green, dark cyan) for oxygen reduction reaction in O_2 saturated 0.1 M KOH, demonstrating good and reproducible ORR peaks; and a sample run for NCNC[Ni] after electrochemical activation in N_2 saturated 0.1 M KOH (red) confirming the origin of ORR peaks.

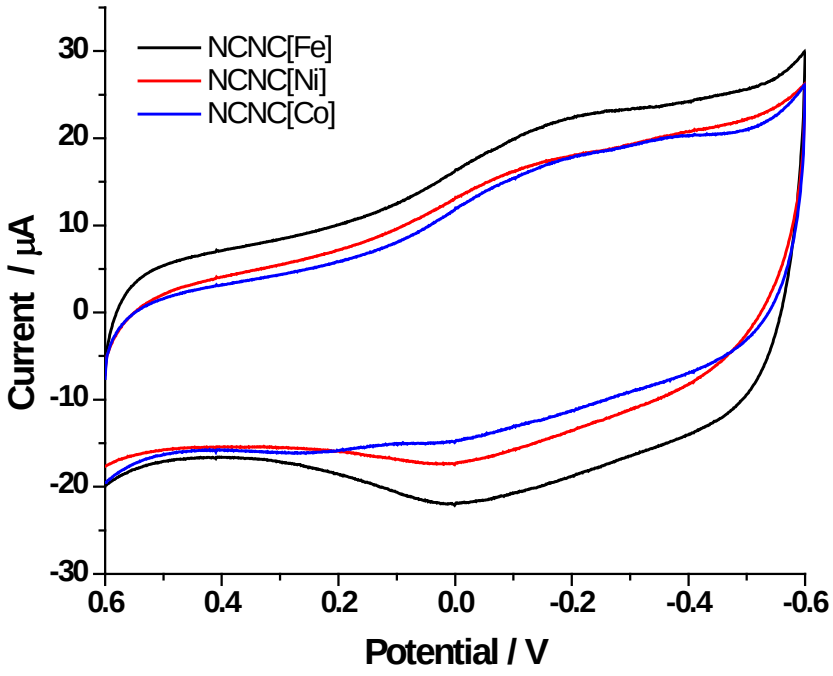

Figure 5-10. Double layer capacitance measurement of NCNCs using cyclic voltammetry in phosphate buffer solution (PBS, pH = 7.2) at a scanning rate of 0.05 V/s showing the different relative surface areas.

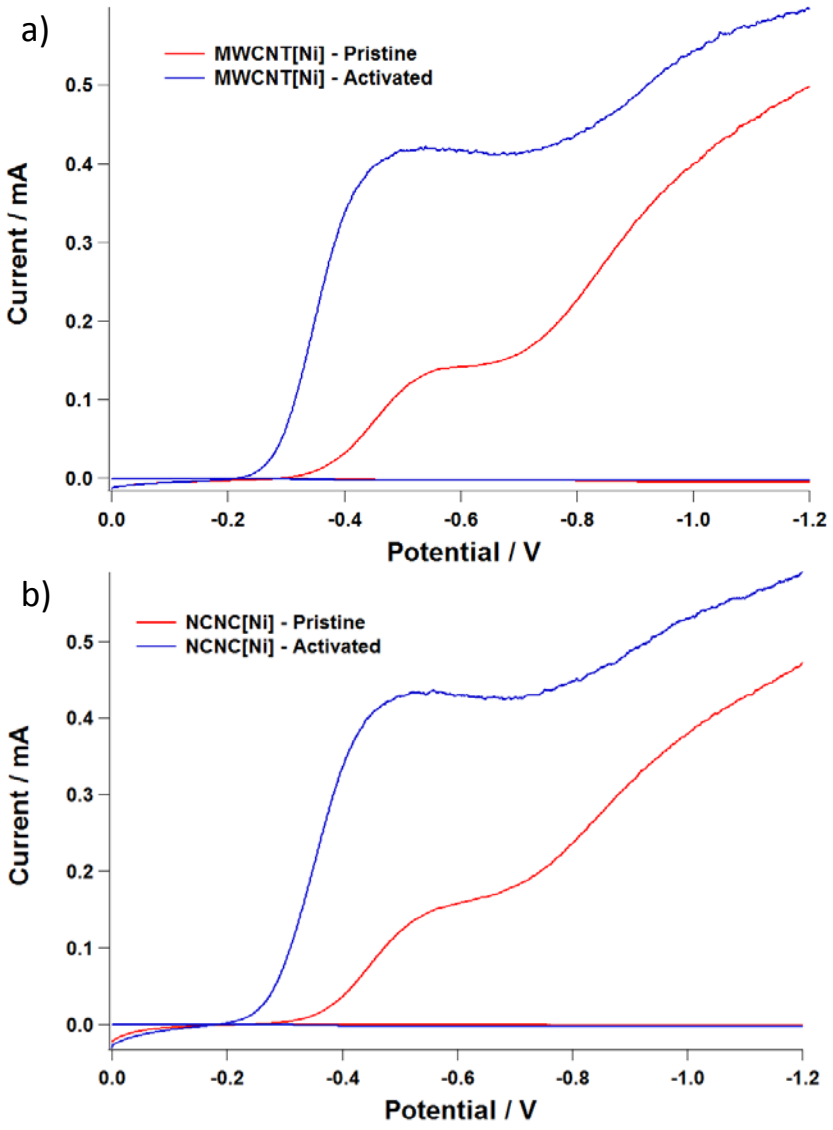

Figure 5-11. RRDE of a) MWCNT[Ni] (n = 3.9), and b) NCNC[Ni] (n = 3.9) before (red) and after (blue) the activation process versus a graphite counter electrode ensuring the 4-electron mechanism does not come from contaminate platinum.

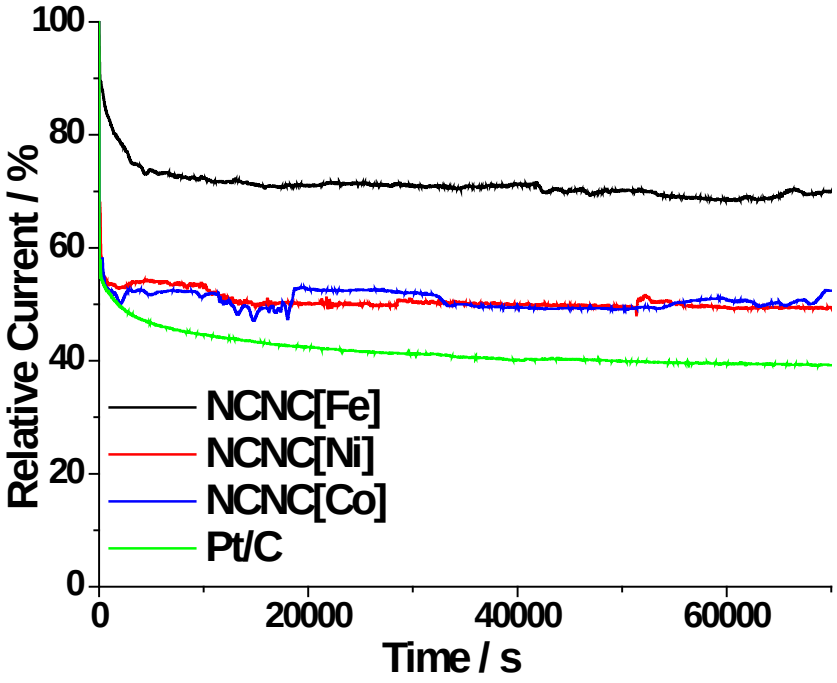

Figure 5-12. The chronoamperometric responses for NCNC[Fe], NCNC[Ni], NCNC[Co] and Pt/C on glassy carbon electrode for oxygen reduction reaction in 0.1 M KOH at - 0.5 V.

Table 5-2. Relative electrochemical active surface area and normalized ORR current.

	NCNC[Fe]	NCNC[Ni]	NCNC[Co]
ORR Current / μA	55.8	51.2	46.2
Double Layer Capacitance / mF[a]	0.620	0.494	0.461
Relative Surface Area	1.00	0.797	0.743
Normalized Current / μA[b]	55.8	64.2	62.2

a. Double layer capacitance was calculated using cyclic voltammetry data of electrochemically activated NCNCs sample in 50 mM N_2 saturated PBS solution. The value would be proportional to the active surface area of the electrode.

b. Normalized current was calculated taking the active surface area of NCNC[Fe] as 1 by comparing the double layer capacitance.

6.0 SEPARATION OF NITROGEN-DOPED CARBON NANOTUBE CUPS

6.1 CHAPTER PREFACE

The nitrogen-doped carbon nanotube cups (NCNCs) have attractive electrocatalytic activity as demonstrated in chapters 4 and 5. On the other hand, their unique cup-shape structure is also of great interest to applications such as drug delivery or nano-reactors. How to effectively separate the stacked nanocups into individual ones would be the first concern we are facing for such applications. The aim of this chapter was to investigate sonication methods to separate stacked NCNCs into individual nanocups. Specifically, NCNCs were suspended in concentrated KCl solution and treated in bath sonication, and the separation results were compared to other solutions in order to obtain some initial understanding about the separation mechanism.

In this chapter, nitrogen-doped carbon nanotube cups (NCNCs) is of great interest to researchers in materials, biomedical and electrochemical areas due to their unique structures and properties. Separating stacked NCNCs into individual ones is an attractive way to further manipulate their morphology, providing additional opportunities for both applications and fundamental structure-property studies. Here we demonstrate an effective, simple, low-cost and safe separation method to obtain individual NCNCs of around 180 nm in the length, by sonicating as-synthesized stacked NCNCs in concentrated KCl solution. Another advantage of this technique is that it is highly selective to the separation of adjacent NCNCs and capable of

preserving the surface structure and functionalities of stacked NCNCs. We have discovered that the presence of potassium ions is vital for the separation and we hypothesized that the separation mechanism involves a partial intercalation that facilitates the separation of NCNCs.

The material contained in this chapter was prepared for submission.

List of Authors: Yifan Tang, Yong Zhao, Mengning Ding, Seth C. Burkert, and Alexander Star

Author contributions: All authors contributed to the design of experiments and writing of the paper. YT, YZ synthesized the NCNCs materials using CVD. YT conducted the separation experiments and characterized the materials using TEM, SEM microscopic and EDX spectroscopic techniques. YZ performed the high-res TEM and Raman characterization. MD performed the XRD characterization. YT and SCB carried out the electrochemical characterizations.

6.2 INTRODUCTION

With their outstanding electrochemical properties,[293,294] especially after the demonstration of their excellent catalytic activity towards oxygen reduction reaction (ORR) in 2009,[30-31] stacked nitrogen-doped carbon nanotube cups (NCNCs) have attracted extensive interest for wide range of applications including energy generation (fuel cells),[31] storage (supercapacitors[17] and batteries)[16] and electrochemical sensor/biosensors.[80,295] However, their intrinsic morphology – the stacked-cups structure – which is believed to be derived from the nitrogen doping, is to some extent less studied compared to the aforementioned applications.[296] Compared to regular

undoped multi-walled carbon nanotubes (MWCNTs), which have a tubular structure with relatively long inaccessible hollow interiors, stacked NCNCs are formed by compartmented hollow structures resembling stacked cups that are held together only through weak van der Waals interactions between their graphitic surfaces.[297,298] Therefore by overcoming the multiple interlayer noncovalent interactions, they can be further separated into individual NCNCs with typical lengths around or under 200 nm.[47,298] Such separated NCNCs with well-defined inner cavities could be of great interest for the applications in drug delivery and nano-sized containers. Moreover, their higher biocompatibility compared to undoped MWCNTs[299,296] and versatile surface chemistry due to the nitrogen doping could also facilitate their biomedical applications.[300] On the other hand, it would also be interesting to investigate the change of electrochemical catalytic activities after the separation of stacked NCNCs in order to gain more insight into the origin of their electrocatalytic properties and to establish the structure-property relationship for this nanomaterial.

Several methods have been reported to date on separation of NCNCs or stacked-cup shaped carbon nanotubes, including grinding with mortar and pestle,[47, 65] oxidation treatment,[301] bath sonication[302] and probe-tip sonication.[298, 300] However, they all have their limitations. Grinding with mortar and pestle is a labor-intensive technique which provides poor yields and unsatisfactory separation results. Oxidation treatment requires harsh chemicals[14] and complicated instrumentation.[301] The bath sonication reported previously[302] still requires a pre-oxidation step by heating the materials in air at ~ 500 °C. Probe-tip sonication, especially when combined with oxidation treatment is very promising and could obtain separated NCNCs with length less than 200 nm.[14] However, the oxidation step altersthe surface funtionalities, as indicated by the increase in Raman D/G ratio and higher oxgen content measured from EDX spectra.[298, 300] The

change in surface functional groups could be an issue when trying to study the electrochemical performance of seperated NCNCs. Another issue is the sample contamination by Ti nanoparticles shed from the tip of a probe-tip sonicator. These issues could be mostly neglected for many biological and chemical applications of NCNCs but are rather crucial for their electrochemical properties.

Here we report a novel separation method to convert stacked NCNCs into separated ones by simple bath sonication of pristine NCNCs in concentrated KCl solution for extended periods of time. Using this method, we can achieve effective separation of NCNCs with average length of ~180 nm while preserving pristine surface structure and functionalities. Electrochemical study for ORR also demonstrated that the separation mostly preserved the catalytic activity of the material. Initial investigation on the separation mechanism suggest that the presence of high concentration of potassium cations is vital for the effective separation. The expansion of graphitic layers was observed. We hypothesized that a process similar to potassium intercalation[303-304] might be responsible for the separation.

6.3 EXPERIMENTAL SECTION

6.3.1 Preparation of Nitrogen-doped Carbon Nanotube Cups (NCNCs)

NCNCs were synthesized using chemical vapor deposition (CVD) method as described in chapter 5 using a three-zone Lindberg/Blue furnace and a 1” quartz tube. Briefly, the CVD process was carried out by injecting a liquid precursor consisting 0.75 wt% of ferrocene, 10 wt% of acetonitrile, and 89.25 wt% of xylenes at a rate of 1 mL/h into the first zone (evaporation

zone) of furnace which was held at temperatures between 250 and 300 °C. Carrier gases of Ar at 127 sccm and H_2 at 38 sccm were used to carry the vaporized precursors to the growth zones and the growth was done at 800 °C for 60 min. The synthesized NCNCs product was collected from a quartz plate placed inside the quartz tube in the growth zones.

6.3.2 Separation of Stacked NCNCs

5 mg of NCNCs was suspended in 25 g of 32wt% KCl solution. The mixture was sonicated in a Branson 1510 bath sonicator for 150 hr. The products were centrifuged, washed with copious amounts of water multiple times in order to remove the salt and glass particles from the container and subjected to characterization and testing.

As a control, 5 mg of NCNCs were suspended in a 25 mL of 32wt% KCl or NaCl solution, or double distilled water and subjected to sonication for 100 hr.

To rule out the effect of different salt concentrations and investigate the effect of different alkali cations, similar separation process was also performed in 5 M KCl, NaCl, or LiCl solutions for 70 hr.

6.3.3 Characterization

Transmission electron microscopy (TEM) images were obtained using a Philips/FEI Morgagni microscope at 80.0 keV accelerating voltage. All samples were prepared by suspension in EtOH and drop-casting on a lacey carbon TEM grid (Pacific Grid-Tech) and by allowing the solvent to evaporate completely. The length measurements were performed with ImageJ software and for each sample at least 200 individual NCNC were measured.

Scanning electron microscopy (SEM) and energy-dispersive X-ray (EDX) spectroscopy were performed with a Phillips XL30 FEG microscope equipped with an EDAX assembly. All samples were prepared by suspension in EtOH and drop-casting onto a copper tape.

X-ray photoelectron spectroscopy (XPS) was performed with a Thermo Scientific K-Alpha X-ray photoelectron spectrometer using monochromated Al Ka X-rays as the source. The sample spot size was 400 μm. Charge compensation was provided by a low energy electron source and Ar^+ ions. Survey scans were collected using a pass energy of 200 eV and high resolution scans had a pass energy of 50 eV.

X-ray diffraction (XRD) spectroscopy was performed with a Bruker D8 Discover XRD with GADDS Detector for powder and thin film diffraction on samples dropcasted on glass slides.

Raman spectra were taken on Renishaw inVia Raman microscope with an excitation wavelength of 633 nm and 10 second exposure time.

Electrochemical characterizations were performed with using a CHI 7042 Bipotentiostat (CH Instruments, Austin, TX). A Pt wire electrode (CHI 115) and an Ag/AgCl (CHI 111, 1 M KCl) electrode were used as the counter and reference electrode, respectively. All potentials are reported versus the reference electrode. The working electrode was either a glassy carbon (GC) electrode (CHI 104, GC area 0.0707cm^2, total area 0.196 cm^2) or rotating ring-disk electrode (Pine AFE7R9GCPT, GC disk area 0.2475 cm^2), and modified with 20 μL of catalyst ink of 1 mg/mL staked or separated NCNCs and 0.04 % Nafion at the glassy carbon part.

6.4 RESULTS AND DISCUSSION

As we can see in Figure 6-1 a, c and e, the as synthesized stacked NCNCs have long fibril structures. Their average length is around 4.3 μm, with a length distribution ranging from a few hundred nanometers to tens of micrometers. The fibril structure was comprised of many conical compartments in the shape of cups stacked in a head-to-tail fashion along the common direction of the tube axis. After sonication in KCl solution for 150 hr, the resulting suspension of separated NCNCs had an average length of around 180 nm, and about 90% of the nanocups were within the range of 0 ~ 300 nm (Figure 6-1 b, d, f). This result provides clear evidence that we can achieve effective separation of NCNCs by simple KCl sonication treatment. Compared to other methods, this process requires neither harsh chemicals (oxidation reagents) nor expensive instruments (probe-tip sonicator). It worth mentioning, however, that this process resulted in the formation of glass particles from the glassware during the long time sonication. The glass particles could be easily removed from the NCNCs sample by centrifugation or low concentration HF washing.

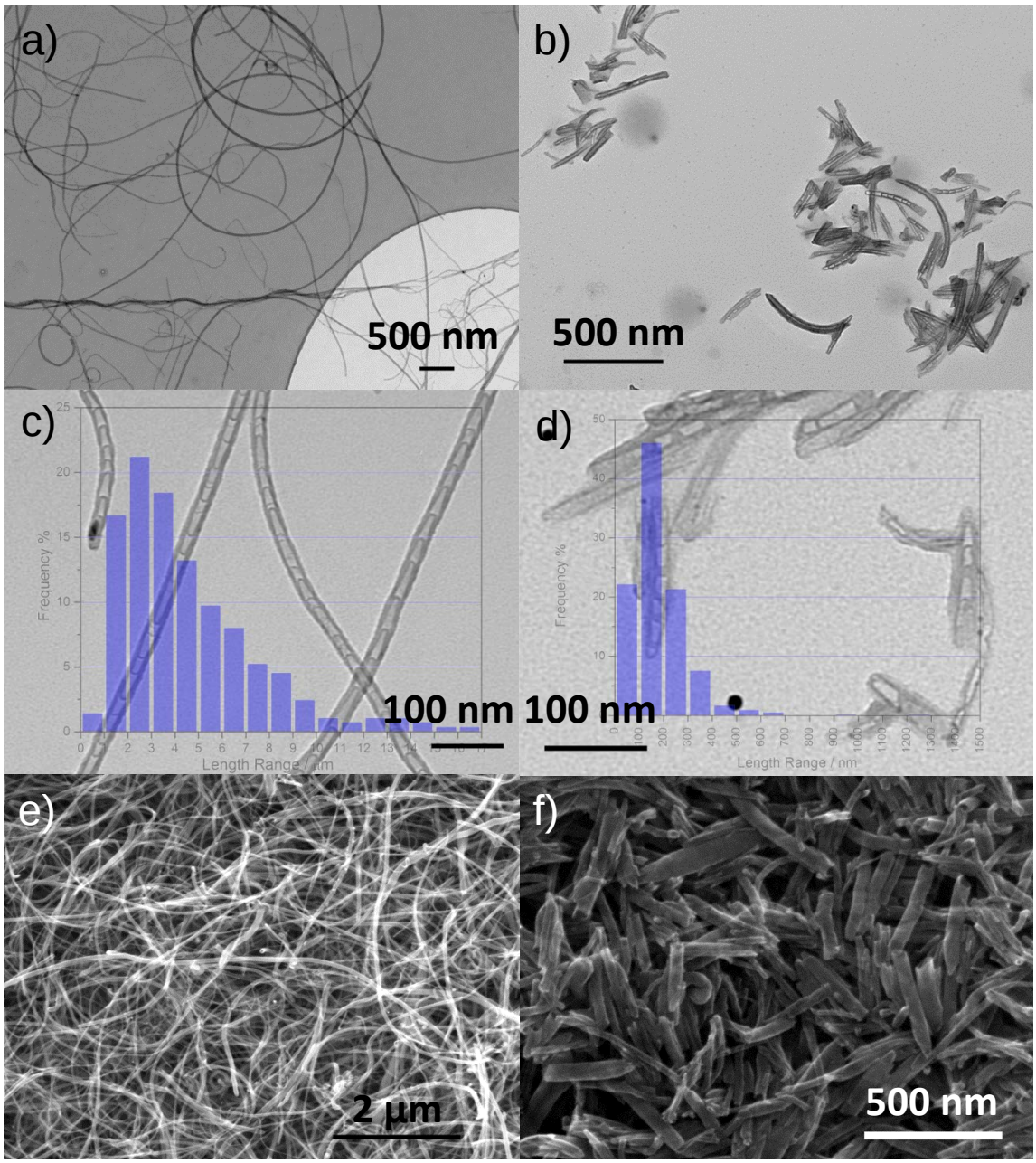

Figure 6-1. Electron microscopy characterization of the NCNCs separation: Low magnification transmission electron microscopy (TEM) images of a) as-synthesized, b) separated NCNCs; higher magnification TEM images of c) as-synthesized, d) separated NCNCs, with the corresponding length histogram; scanning electron microscopy (SEM) images of e) as-synthesized, f) separated NCNCs. The separation of NCNCs was achieved by sonication in 32% KCl solution for 150 hr.

Further characterization showed that, this KCl sonication method not only separated stacked NCNCs but also largely preserved their original surface structure. This is quite unique compared to the oxidation or probe-tip sonication methods since these methods typically result in a significant change in the surface functionalities and thus the physical, chemical or electrochemical properties of the NCNCs materials. Table 6-1 shows the summary of elemental analysis of stacked and separated NCNCs. It should be noted that the relative concentration of oxygen remained unchanged compared to the previously reported data (~4 at%) for the oxidation or probe-tip sonication methods.[298, 300] The relative nitrogen concentration was also preserved in this separation process. This could be expected since only KCl (not oxidation reagent) was used and the bath sonication conditions are much gentler than probe-tip sonication.

Table 6-1. Elemental analysis of stacked and separated NCNCs showing relative oxygen and nitrogen content.

Relative Concentration	Stacked NCNCs	Separated NCNCs
C	1	1
O (from EDX)	0.010±0.004	0.013±0.002
N (from XPS)	0.014±0.003	0.016

More interestingly, Raman results (Figure 6-2a) showed that the D/G ratio changed from 1.16 of stacked NCNCs to 1.07 of separated NCNCs, compared to the probe-tip method where the D/G ratio increases constantly with the process time.[298] Such a decrease in the D/G ratio might be related to the removal of extra amorphous carbon[298] or other highly defected structures during the separation process, while leaving the major surface of NCNCs unaffected. This

Raman result showed a superior selectivity of the KCl sonication process towards breaking up the interlayer π-π interaction of adjacent cups or amorphous carbon structure rather than attacking the whole graphitic surface of NCNCs.

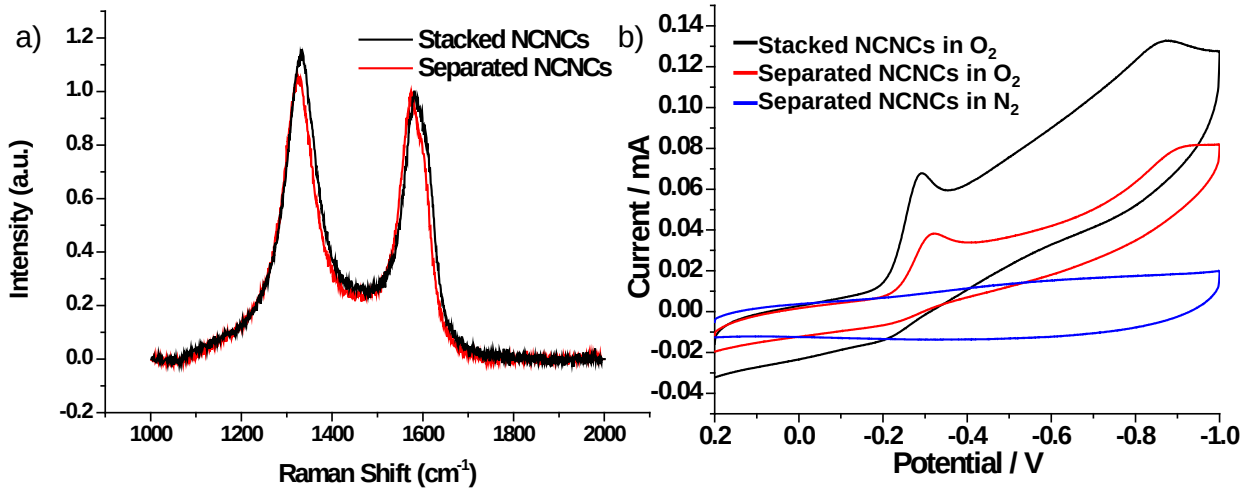

Figure 6-2. a) Raman spectra of stacked and separated NCNCs; b) cyclic voltammograms for stacked and separated NCNCs in O_2/N_2 saturated 0.1 M KOH demonstrating the oxygen reduction reaction activity.

Oxygen reduction reaction (ORR) – arguably one of the most important applications of nitrogen-doped carbon materials –was studied here to investigate the effect of the KCl treatment on the structure and electrochemical properties of NCNCs. As we can see in Figure 6-2b, separated NCNCs remained catalytically active towards ORR, although there is a slight negative shift in the ORR peak potential. The major difference between the electrochemical performance of the stacked NCNCs and separated NCNCs was the measured current. We attribute the much smaller current of separated NCNCs to their significantly shortened structures. For separated NCNCs, their length (~180 nm) is already comparable to their diameter (20~50 nm). This aspect ratio could result in a much denser packing of the separated NCNCs compared to stacked NCNCs (Figure 6-1 e, f) and lead to a decreased electrochemically active surface area as shown

by the double layer capacitance in the CVs. Also the much shorter separated NCNCs are expected to have higher resistance due to increased contacts between individual cups, making them relatively unfavorable as the electrode materials.

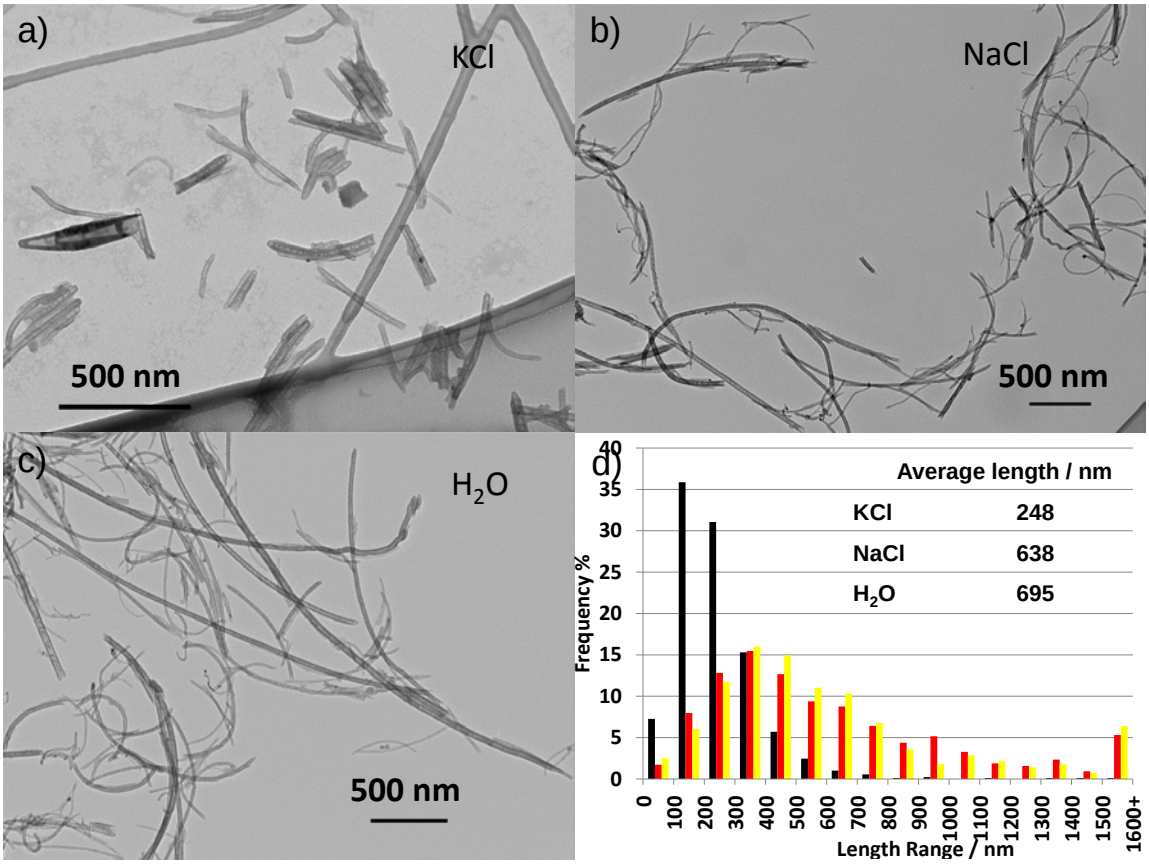

Figure 6-3. Representative TEM images of NCNCs treated with a) 32 wt% KCl, b) 32wt% NaCl, c) DI water for 100 hr; d) histogram and table with average length (inset) of the three different separated NCNCs samples showing the relative effect of KCl in the NCNCs separation.

In order to investigate the mechanism of the KCl separation, we repeated the separation process in 32 wt% KCl, 32 wt% NaCl and pure DI water for 100 hr. The representative TEM images and length histograms are shown in Figure 6-3. To our surprise only KCl solution showed effective separation, while the results from NaCl solution and water are quite similar to each other. It seems that NaCl has little effect towards the separation of NCNCs and the length

decrease in the latter two is merely due to the sonication power. Thus we can hypothesize that potassium ions are primarily responsible for the observed separation of NCNCs.

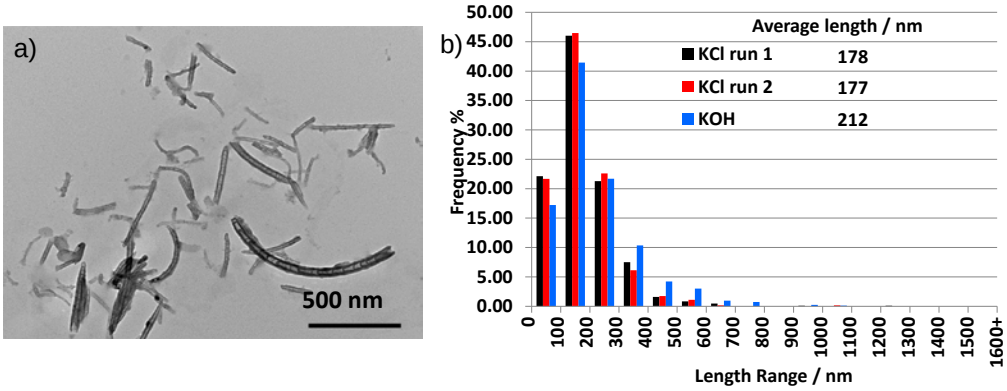

Figure 6-4. a) A representative TEM image of NCNCs treated with 50% KOH solution for 26 hr. b). Histogram of NCNCs treated with KOH and KCl, and table of average length (inset).

We also performed similar separation process in 50 wt% KOH solution, in order to once again confirm the important role of potassium towards the separation. The treatment was stopped at 26 hr due to the strong corrosive effect of KOH towards the glassware. However in Figure 6-4, we can still see the similar effective separation of NCNCs as KCl did even with a much shorter treatment time.

Potassium had been long used to form intercalation material such as C_8K with graphite[303, 305]. Typical intercalation process such as two-zone vapor transport method usually was performed at high temperatures, inert atmosphere. In our case, no intercalation product was found as the product analysis showed no detectable potassium signal. Moreover, compounds like C_8K are not expected to be stable in aqueous solution conditions. However, we suspect that during the sonication, partial intercalation of potassium did happen to facilitate the separation of graphitic interlayers between the adjacent individual NCNCs. As shown in Figure 6-5 a and b, the lattice distance increased from 0.344±0.003 nm for stacked NCNCs to 0.395±0.013 for separated NCNCs. This was further confirmed by the XRD spectra in Figure 6-5c. A slight shift

of (002) peak from ~26.1° to ~26.3° was observed, although the peaks were much weaker and broadened compared to graphite, due to the limited graphitic layer numbers and area.[306]

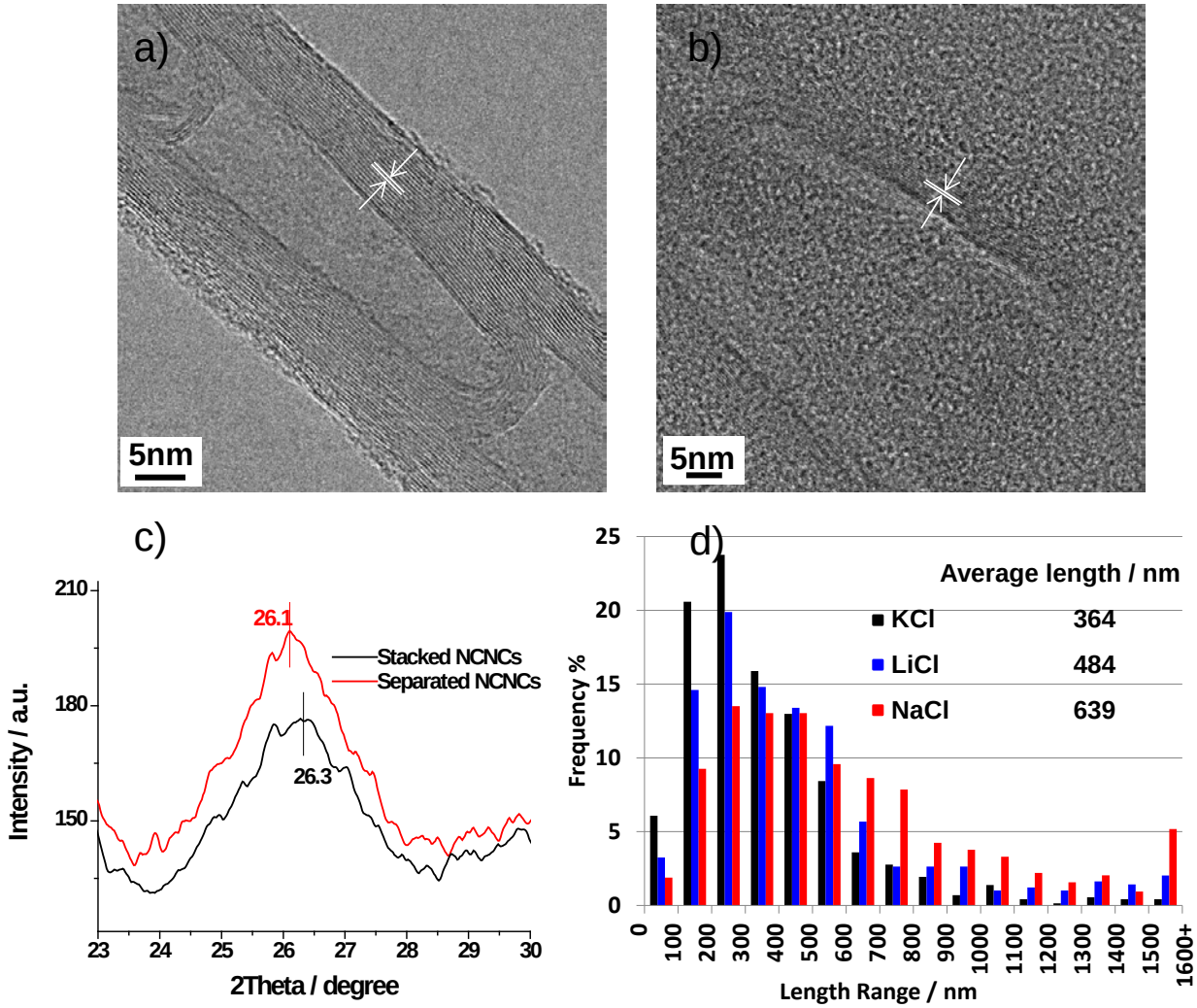

Figure 6-5. High-resolution TEM images of a) stacked and b) separated NCNCs; white markers showing the graphitic lattice; c) X-Ray Diffraction spectra of stacked and separated NCNCs showing a down shift of the (002) peak position; d) histogram of NCNCs treated with 5M KCl, 5M LiCl and 5M NaCl for 70 hr and table of average length (inset).

Lithium is also another common metal used for intercalation applications.[307] It is possible that Li salt could also help the separation as KCl does. So we again tested the separation process by comparing the effect of 5M KCl, LiCl and NaCl solution. This time, relatively lower but

identical molar concentrations were used for different metal salts in order to exclude any effect of different ion concentrations. As the salt concentration and process time decreased, relatively poor separation results were achieved (Figure 6-5d). However KCl still showed the best results compared to LiCl and NaCl. NCNCs treated in NaCl had almost the same average length as in the previous control experiments with NaCl and H_2O, again demonstrating that NaCl has very little effect towards the separation of NCNCs. The observed trend of $K^+ > Li^+ > Na^+$ in alkali metals ions is mostly consistent with the previously reported observations of intercalation compounds.[304] The detailed reason for LiCl being better than NaCl but not as good as KCl is not clear yet. One possible explanation might be related to the strong hydration effect of Li^+.[308]

6.5 CONCLUSIONS

To sum up, we reported here a novel method to separate stacked NCNCs into separated NCNCs by simple and easy sonication in concentrated KCl solution. This process is effective and also selective. We obtained NCNCs with an average length of 180 nm while preserving the original material surface composition, functionalities and electrochemical properties. A hypothesis of partial potassium intercalation was suggested for the separation mechanism as control experiments demonstrated that the presence of potassium is crucial for the separation.

6.6 ACKNOWLEDGEMENT

This work was supported by NSF career award No. 0954345. Y. Z. acknowledges a graduate student fellowship through Bayer MaterialScience. We thank the Department of Biological Sciences, the Department of Materials Science and Engineering and NFCF at the University of Pittsburgh for access to the TEM, SEM, XRD and High-res TEM instrumentation. We also thank RJ Lee Group, Inc. for the help in XPS testing.

7.0 CONCLUDING REMARKS

Carbon nanomaterials are indeed the hottest topic in the field of nanoscience and nanotechnology. The chapters contained in this dissertation outline the work that I have completed while pursuing my Ph. D. in Dr. Alexander Star's research group, hoping to contribute to the progress and development of nanotechnology.

My research focused on the synthesis, functionalization, characterization of novel carbon-based nanomaterials and their electrochemical applications in sustainable energy generation and sensors. In Chapter 2.0 we compared Pt nanoparticles functionalized SWNTs to Pt NPs functionalized graphene as the sensing platforms in order compare their performance in electrochemical sensors and also to obtain some insight into the structure-property relationship in these 1D and 2D systems. Continuing the research on Pt-CNTs hybrid structures, we investigated their long-term performance as phosphoric acid fuel cells (PAFC) cathodes in chapter 3.0, showing that CNTs based electrodes had improved performance (life-time) and required less expensive Pt material. Then we moved one step further, in chapter 4.0, with the novel nitrogen-doped carbon nanotube cups (NCNCs) that we synthesized in our lab, we used them as non-precious-metal catalysts trying to replace expensive Pt based catalysts in both fuel cells and sensor/biosensors. Then chapter 5.0 continued to focus on revealing the origin of the catalytic activity of NCNCs from the structure/composition point of view, showing that both iron and nitrogen are essential for the improved ORR catalytic activity. Finally, in chapter 6.0, we

performed structural manipulation of NCNCs by separating them using a simple sonication process in concentrated KCl solution, paving the pathway towards future application of NCNCs for drug delivery and nano-reactors.

The connections between each chapter are materials/application driven; however, each application is deeply rooted in the understanding of structure-property relationship of the materials. My hope is that these projects will contribute to the field of nanoscience and nanotechnology, not only by demonstrating several novel nanomaterials and their electrochemical properties/applications, but also by paving the way to the further manipulation of their structure and/or composition based on the knowledge of their structure-property relationship, and finally by developing better materials with improved properties.

APPENDIX A

XPS CHARACTERIZATION ON NITROGEN-DOPED CARBON NANOTUBE CUPS

This appendix contains additional X-ray photoelectron spectroscopy (XPS) characterization on nitrogen-doped carbon nanotube cups (NCNCs) discussed in chapter 5. High-resolution N1s spectra were analyzed and discussed.

X-ray photoelectron spectroscopy was obtained with a Thermo Scientific K-Alpha X-ray photoelectron spectrometer using monochromated Al Kα x-rays (1486.6 eV) as the source. The sample spot size was 400 μm. Charge compensation was provided by a low energy electron source and Ar^+ ions. Survey scans were collected using a pass energy of 200 eV and high resolution scans had a pass energy of 50 eV. XPS samples were prepared by dropcasting the corresponding NCNC suspension in ethanol onto an aluminum substrate on a hot plate. XPS binding energies were corrected using the C1s peak at 285 eV as an internal standard. Deconvolution of the high-res N1s spectra were performed after background subtraction of a Shirley type baseline. Peak positions and heights were optimized with fixed Gaussian:Lorentzian ratio of 80:20.

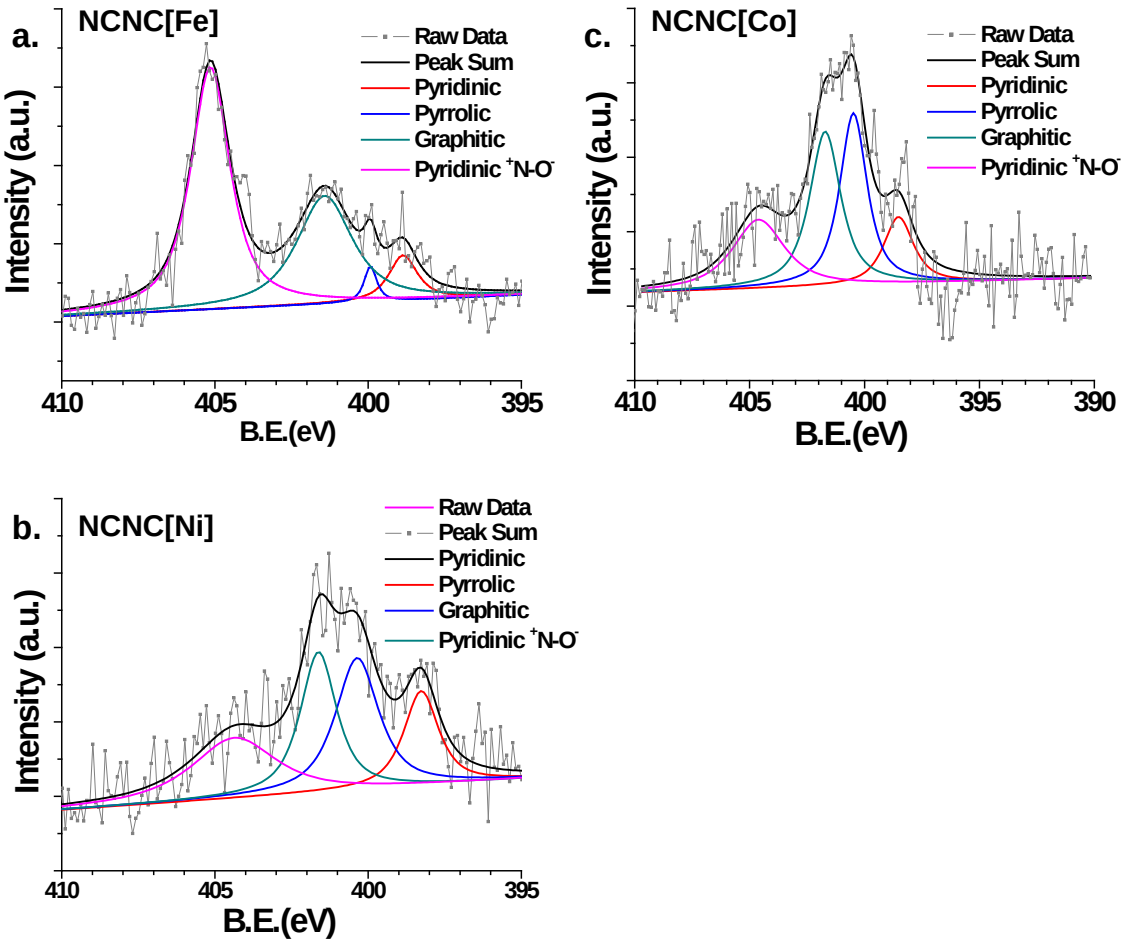

Figure Appendix 1. High-resolution N1s x-ray photoelectron spectroscopy of a) NCNC[Fe], b) NCNC[Ni] and c) NCNC[Co] with the raw data in scattered dots and devonvoluted peaks in solid lines.

Figure Appendix 1 shows the deconvoluted high-resolution N1s XPS spectra of all three NCNC samples. The corresponding survey scans are shown in Figure 5-5 in chapter 5. As discussed in the introduction 1.1.3, high-res N1s can be assigned into several different nitrogen functionalities: pyridinic N (398.2 – 398.9 eV), pyrrolic N (399.9 – 400.5 eV), graphitic/ quaternary N (401.4 – 401.8 eV), and nitrogen oxides of pyridinic N (pyridinic $^{+}$N-O^{-}, 404.3 – 405.1 eV). The relative concentrations of each nitrogen species are listed in the table below.

Table Appendix 1. Relative concentration of different nitrogen species in NCNCs.

Relative Concentration / %	Pyridinic N (398.2 – 398.9 eV)	Pyrrolic N (399.9 – 400.5 eV)	Graphitic N (401.4 – 401.8 eV)	Pyridinic $^{+}$N-O^{-} (404.3 – 405.1 eV)
NCNC[Fe]	7.5	2.6	34.9	55.0
NCNC[Ni]	17.1	29.8	26.6	26.5
NCNC[Co]	13.2	33.2	29.3	24.3

All three samples have relative high nitrogen oxide (Pyridinic $^{+}$N-O^{-}) concentration. It is even dominating in the NCNC[Fe] sample. On the other hand, NCNC[Fe] also has relative higher graphitic N concentration, which could be another contributing factor for its enhanced ORR performance in terms of the current and on-set potential. We attribute such increased graphitic N content to the using of Fe catalyst which was demonstrated to facilitate the forming of graphitic N species.[96] However for NCNC[Ni] and NCNC[Co], comparable amount for different nitrogen functionalities were observed. Considering the significant difference in the ORR mechanism between NCNC[Ni] (with the electron transfer number close to 4) and NCNC[Co] (with the electron transfer number around 3), it further supports our explanation that metal also plays a crucial role in the ORR, affecting the reaction path-way significantly.

terials with improved properties.

APPENDIX B

CONTRIBUTING ROLE IN ADDITIONAL PROJECTS

The following abstracts are taken from publications in which I played a contributing role to the research. My contributions are described in detail.

B.1 UNDERSTANDING INTERFACES IN METAL–GRAPHITIC HYBRID NANOSTRUCTURES

Citation: Ding, M.; Tang, Y.; Star, A. *J. Phys. Chem. Lett.* **2013**, *4*, 147.

Abstract

Metal–graphitic interfaces formed between metal nanoparticles (MNPs) and carbon nanotubes (CNTs) or graphene play an important role in the properties of such hybrid nanostructures. This Perspective summarizes different types of interfaces that exist within the metal–carbon nanoassemblies and discusses current efforts on understanding and modeling the interfacial conditions and interactions. Characterization of the metal–graphitic interfaces is described here, including microscopy, spectroscopy, electrochemical techniques, and electrical measurements.

Recent studies on these nanohybrids have shown that the metal–graphitic interfaces play critical roles in both controlled assembly of nanoparticles and practical applications of nanohybrids in chemical sensors and fuel cells. Better understanding, design, and manipulation of metal–graphitic interfaces could therefore become the new frontier in the research of MNP/CNT or MNP/graphene hybrid systems.

For this review article, my contribution was on writing on topics related to fuel cells and electrochemical characterization of the nanohybrid structures.

B.2 SYNTHESIS AND FUNCTIONALIZATION OF NITROGEN-DOPED CARBON NANOTUBE CUPS WITH GOLD NANOPARTICLES AS CORK STOPPERS

Citation: Zhao, Y.; Tang, Y.; Star, A., *J Vis Exp* **2013**, e50383.

Abstract

Nitrogen-doped carbon nanotubes consist of many cup-shaped graphitic compartments termed as nitrogen-doped carbon nanotube cups (NCNCs). These as-synthesized graphitic nanocups from chemical vapor deposition (CVD) method were stacked in a head-to-tail fashion held only through noncovalent interactions. Individual NCNCs can be isolated out of their stacking structure through a series of chemical and physical separation processes. First, as-synthesized NCNCs were oxidized in a mixture of strong acids to introduce oxygen-containing defects on the graphitic walls. The oxidized NCNCs were then processed using high-intensity probe-tip sonication which effectively separated the stacked NCNCs into individual graphitic nanocups. Owing to their abundant oxygen and nitrogen surface functionalities, the resulted individual

NCNCs are highly hydrophilic and can be effectively functionalized with gold nanoparticles (GNPs), which preferentially fit in the opening of the cups as cork stoppers. These graphitic nanocups corked with GNPs may find promising applications as nanoscale containers and drug carriers.

For this article, I contributed to the CVD synthesis of NCNCs, SEM, EDX and XPS characterizations and also providing assistance to YZ in the separation process. All authors contributed to the design of experiments and writing of the paper.

B.3 CORKING CARBON NANOTUBE CUPS WITH GOLD NANOPARTICLE

Citation: Zhao, Y.; Tang, Y.; Chen, Y.; Star, A. *ACS Nano* **2012**, *6*, 6912.

Abstract

Nitrogen doping of carbon nanotubes during chemical vapor deposition synthesis can create unique stacked cup-shaped structures termed as nitrogen-doped carbon nanotube cups (NCNCs). These cups have semielliptical hollow cavities and elevated reactivity which could lead to various applications. In this work, by applying intense ultrasonication to the as-synthesized NCNCs, we demonstrated an effective mechanical method to isolate the individual cups with opened cavities from their stacks. The graphitic structures of the isolated cups and their inherent nitrogen functionalities were characterized by comprehensive microscopic and spectroscopic methods. In particular, we quantitatively determined the existence of amine functionalities on NCNCs and found that they were preferentially distributed at the open edges of the cups, providing localized reactive sites. Further, by thiolating the amine groups with 3-mercapto-propionic acid, we were able to effectively cork the isolated cups by gold nanoparticles with

commensurate diameters. These cup-shaped carbon nanomaterials with controlled inner volumes and gold nanoparticle corks could find potential applications as nanoscale reaction containers or drug delivery vehicles.

For this article, I contributed to the CVD synthesis of NCNCs, SEM, EDX and XPS characterizations and also providing assistance to YZ in the separation process. All authors contributed to the design of experiments and writing of the paper.

B.4 ELECTROCHEMICAL CHARACTERIZATION OF CARBON NANOTUBE FORESTS GROWN ON COPPER FOIL USING TRANSITION METAL CATALYSTS

Citation: Atthipalli, G.; Tang, Y.; Star A.; Gray J. L. *Thin Solid Films* **2011**, *520*, 1651.

Abstract

Growth of vertical, multiwalled carbon nanotubes (CNTs) on bulk copper foil substrates can be achieved by sputtering either Ni or Inconel thin films on Cu substrates followed by thermal chemical vapor deposition using a xylene and ferrocene mixture. During CVD growth, Fe nanoparticles from the ferrocene act as a vapor phase delivered catalyst in addition to the transition metal thin film, which breaks up into islands. Both the thin film and iron are needed for dense and uniform growth of CNTs on the copper substrates. The benefits of this relatively simple and cost effective method of directly integrating CNTs with highly conductive copper substrates are the resulting high density of nanotubes that do not require the use of additional binders and the potential for low contact resistance between the nanotubes and the substrate. This method is therefore of interest for charge storage applications such as double layer capacitors.

Inconel thin films in conjunction with Fe from ferrocene appear to work better in comparison to Ni thin films in terms of CNT density and charge storage capability. We report here the power density and specific capacitance values of the double layer capacitors developed from the CNTs grown directly on copper substrates.

For this article, I contributed partially to the CVD synthesis MWNTs, electrochemical characterization of the supercapacitors and interpretation of the electrochemical testing data. All authors contributed to the design of experiments and writing of the paper.

B.5 CHEMICAL SENSING WITH POLYANILINE COATED SINGLE-WALLED CARBON NANOTUBES

Citation: Ding, M.; Tang, Y.; Gou, P.; Reber, M. J.; Star, A. *Adv. Mater.* **2011**, *23*, 536.
.

Abstract

A positive synergy: Single-walled carbon nanotube/polyaniline (SWNT/PAni) nanocomposite with controlled core/shell morphology was synthesized by a noncovalent functionalization approach. Unique electron interactions between the SWNT core and the PAni shell were studied electrochemically and spectroscopically, and superior sensor performance to chemical gases and vapors was demonstrated.

For this article, I contributed to the electrochemical characterization of materials. All authors contributed to the design of experiments and writing of the paper.

B.6 THE EFFECT OF TEMPERATURE ON THE GROWTH OF CARBON NANOTUBES ON COPPER FOIL USING A NICKEL THIN FILM AS CATALYST

Citation: Atthipalli, G.; Epur, R.; Kumta, P. N.; Allen, B. L.; **Tang, Y.**; Star, A; Gray, J. L. *Thin Solid Films* **2011**, *519*, 5371.

Abstract

Growth of carbon nanotubes (CNTs) on bulk copper foil substrates has been achieved by sputtering a nickel thin film on Cu substrates followed by thermal chemical vapor deposition. The characteristics of the nanotubes are strongly dependent on the Ni film thickness and reaction temperature. Specifically, a correlation between the thin film nickel catalyst thickness and the CNT diameter was found. Two hydrocarbon sources investigated were methane and acetylene to determine the best conditions for growth of CNTs on copper. These results demonstrate the effectiveness of this simple method of directly integrating CNTs with highly conductive substrates for use in applications where a conductive CNT network is desirable.

For this article, I contributed partially to the CVD synthesis of MWNTs. All authors contributed to the design of experiments and writing of the paper.

BIBLIOGRAPHY

1. Geim, A. K.; Novoselov, K. S., *Nat. Mater.* **2007,** *6*, 183-191.
2. Pumera, M., *Chem. Soc. Rev.* **2010,** *39*, 4146-4157.
3. Baughman, R. H.; Zakhidov, A. A.; de Heer, W. A., *Science* **2002,** *297*, 787-792.
4. Dai, H., *Acc. Chem. Res.* **2002,** *35*, 1035-1044.
5. Bakker, E., *Anal. Chem.* **2004,** *76*, 3285-3298.
6. Besteman, K.; Lee, J.-O.; Wiertz, F. G.; Heering, H. A.; Dekker, C., *Nano Lett.* **2003,** *3*, 727-730.
7. Jacobs, C. B.; Peairs, M. J.; Venton, B. J., *Anal. Chim. Acta* **2010,** *662*, 105-127.
8. Kauffman, D. R.; Star, A., *Angew. Chem. Int. Ed.* **2008,** *47*, 6550-6570.
9. Ronkainen, N. J.; Halsall, H. B.; Heineman, W. R., *Chem. Soc. Rev.* **2010,** *39*, 1747-1763.
10. Shao, Y.; Wang, J.; Wu, H.; Liu, J.; Aksay, I. A.; Lin, Y., *Electroanal.* **2010,** *22*, 1027-1036.
11. Byon, H. R.; Suntivich, J.; Shao-Horn, Y., *Chem. Mater.* **2011,** *23*, 3421-3428.
12. Lin, Y.; Cui, X.; Yen, C.; Wai, C. M., *J. Phys. Chem. B* **2005,** *109*, 14410-14415.
13. Pumera, M., *Chem. Euro. J.* **2009,** *15*, 4970-4978.
14. Sherigara, B. S.; Kutner, W.; D'Souza, F., *Electroanal.* **2003,** *15*, 753-772.
15. Vu, H.; Gonçalves, F.; Philippe, R.; Lamouroux, E.; Corrias, M.; Kihn, Y.; Plee, D.; Kalck, P.; Serp, P., *J. Catal.* **2006,** *240*, 18-22.
16. Shin, W. H.; Jeong, H. M.; Kim, B. G.; Kang, J. K.; Choi, J. W., *Nano Lett.* **2012,** *12*, 2283-2288.
17. Wiggins-Camacho, J. D.; Stevenson, K. J., *J. Phys. Chem. C* **2009,** *113*, 19082-19090.

18. Girishkumar, G.; Rettker, M.; Underhile, R.; Binz, D.; Vinodgopal, K.; McGinn, P.; Kamat, P., *Langmuir* **2005,** *21*, 8487-8494.

19. Tang, J. M.; Jensen, K.; Waje, M.; Li, W.; Larsen, P.; Pauley, K.; Chen, Z.; Ramesh, P.; Itkis, M. E.; Yan, Y.; Haddon, R. C., *J. Phys. Chem. C* **2007,** *111*, 17901-17904.

20. Avouris, P., *Acc. Chem. Res.* **2002,** *35*, 1026-1034.

21. Kauffman, D. R.; Star, A., *Chem. Soc. Rev.* **2008,** *37*, 1197-1206.

22. Louie, S., Electronic Properties, Junctions, and Defects of Carbon Nanotubes. In *Carbon Nanotubes*, Dresselhaus, M.; Dresselhaus, G.; Avouris, P., Eds. Springer Berlin Heidelberg: 2001; Vol. 80, pp 113-145.

23. Sohn, J.-I.; Lee, S.; Song, Y.-H.; Sung-Yool, C.; Kyoung-Ik, C.; Nam, K.-S., *Appl. Phys. Lett.* **2001,** *78*, 901-903.

24. Gong, X.; Liu, J.; Baskaran, S.; Voise, R. D.; Young, J. S., *Chem. Mater.* **2000,** *12*, 1049-1052.

25. Lau, A. K.-T.; Hui, D., *Compos. Part. B Eng.* **2002,** *33*, 263-277.

26. Biercuk, M. J.; Llaguno, M. C.; Radosavljevic, M.; Hyun, J. K.; Johnson, A. T.; Fischer, J. E., *Appl. Phys. Lett.* **2002,** *80*, 2767-2769.

27. Okamoto, M.; Fujigaya, T.; Nakashima, N., *Small* **2009,** *5*, 735-740.

28. Bianco, A.; Kostarelos, K.; Prato, M., *Curr. Opin. Chem. Biol.* **2005,** *9*, 674.

29. Liu, Z.; Tabakman, S.; Welsher, K.; Dai, H., *Nano Res.* **2009,** *2*, 85-120.

30. Gong, K.; Du, F.; Xia, Z.; Durstock, M.; Dai, L., *Science* **2009,** *323*, 760-764.

31. Tang, Y.; Allen, B. L.; Kauffman, D. R.; Star, A., *J. Am. Chem. Soc.* **2009,** *131*, 13200-13201.

32. Ewels, C. P.; Glerup, M., *J. Nanosci. Nanotechnol.* **2005,** *5*, 1345-1363.

33. Georgakilas, V.; Gournis, D.; Tzitzios, V.; Pasquato, L.; Guldi, D. M.; Prato, M., *J. Mater. Chem.* **2007,** *17*, 2679-2694.

34. Wildgoose, G. G.; Banks, C. E.; Compton, R. G., *Small* **2006,** *2*, 182-193.

35. Ding, M.; Tang, Y.; Star, A., *J Phys. Chem. Lett.* **2012,** *4*, 147-160.

36. Iijima, S., *Nature* **1991,** *354*, 56-58.

37. Novoselov, K. S.; Geim, A. K.; Morozov, S. V.; Jiang, D.; Zhang, Y.; Dubonos, S. V.; Grigorieva, I. V.; Firsov, A. A., *Science* **2004,** *306*, 666-669.

38. Lee, C.; Wei, X.; Kysar, J. W.; Hone, J., *Science* **2008,** *321*, 385-388.

39. Park, S.; Ruoff, R. S., *Nat Nano* **2009,** *4*, 217-224.

40. Yang, W.; Ratinac, K. R.; Ringer, S. P.; Thordarson, P.; Gooding, J. J.; Braet, F., *Angew. Chem. Int. Ed.* **2010,** *49*, 2114-2138.

41. Rao, C. N. R.; Sood, A. K.; Subrahmanyam, K. S.; Govindaraj, A., *Angew. Chem. Int. Ed.* **2009,** *48*, 7752-7777.

42. Geim, A. K., *Science* **2009,** *324*, 1530-1534.

43. Cao, G., *Nanostructures and Nanomaterials: Synthe*. Imperial College Pr: 2004.

44. Delgado, J. L.; Herranz, M. a. A.; Martin, N., *J. Mater. Chem.* **2008,** *18*, 1417-1426.

45. Li, D.-C.; Dai, L.; Huang, S.; Mau, A. W. H.; Wang, Z. L., *Chem. Phys. Lett.* **2000,** *316*, 349-355.

46. Kiselev, N. A.; Sloan, J.; Zakharov, D. N.; Kukovitskii, E. F.; Hutchison, J. L.; Hammer, J.; Kotosonov, A. S., *Carbon* **1998,** *36*, 1149-1157.

47. Allen, B. L.; Kichambare, P. D.; Star, A., *ACS Nano* **2008,** *2*, 1914-1920.

48. Sinnott, S. B.; Andrews, R., *Crit. Rev. Solid State Mater. Sci.* **2001,** *26*, 145-249.

49. Charlier, J. C., *Acc. Chem. Res.* **2002,** *35*, 1063-1069.

50. Daenen, M.; De Fouw, R.; Hamers, B.; Janssen, P.; Schouteden, K.; Veld, M., The Wondrous World of Carbon Nanotubes. A Review of Current Carbon Nanotube Technologies. Eindhoven university of technology: 2003; p 89.

51. Yudasaka, M.; Komatsu, T.; Ichihashi, T.; Iijima, S., *Chem. Phys. Lett.* **1997,** *278*, 102-106.

52. Li, W. Z.; Xie, S. S.; Qian, L. X.; Chang, B. H.; Zou, B. S.; Zhou, W. Y.; Zhao, R. A.; Wang, G., *Science* **1996,** *274*, 1701-1703.

53. Viculis, L. M.; Mack, J. J.; Kaner, R. B., *Science* **2003,** *299*, 1361.

54. Xie, X.; Ju, L.; Feng, X.; Sun, Y.; Zhou, R.; Liu, K.; Fan, S.; Li, Q.; Jiang, K., *Nano Lett.* **2009,** *9*, 2565-2570.

55. Yuan, L.; Saito, K.; Hu, W.; Chen, Z., *Chem. Phys. Lett.* **2001,** *346*, 23-28.

56. Hsu, W. K.; Terrones, M.; Hare, J. P.; Terrones, H.; Kroto, H. W.; Walton, D. R. M., *Chem. Phys. Lett.* **1996,** *262*, 161-166.

57. Laplaze, D.; Bernier, P.; Maser, W. K.; Flamant, G.; Guillard, T.; Loiseau, A., *Carbon* **1998,** *36*, 685-688.

58. Popov, V. N., *Mater. Sci. Eng. R* **2004,** *43*, 61-102.

59. Journet, C.; Bernier, P., *Appl. Phys. A* **1998,** *67*, 1-9.

60. Ebbesen, T. W.; Ajayan, P. M., *Nature* **1992,** *358*, 220-222.

61. Journet, C.; Maser, W. K.; Bernier, P.; Loiseau, A.; de la Chapelle, M. L.; Lefrant, S.; Deniard, P.; Lee, R.; Fischer, J. E., *Nature* **1997,** *388*, 756-758.

62. Thess, A.; Roland, L.; Nikolaev, P.; Dai, H.; Petit, P.; Robert, J.; Xu, C.; Lee, Y. H.; Seong Gon, K.; Rinzler, A. G.; Colbert, D. T.; Scuseria, G. E.; Tománek, D.; Fischer, J. E.; Smalley, R. E., *Science* **1996,** *273*, 483-487.

63. Dai, H., *Surf. Sci.* **2002,** *500*, 218-241.

64. Nikolaev, P.; Bronikowski, M. J.; Bradley, R. K.; Rohmund, F.; Colbert, D. T.; Smith, K. A.; Smalley, R. E., *Chem. Phys. Lett.* **1999,** *313*, 91-97.

65. Allen, B. L.; Shade, C. M.; Yingling, A. M.; Petoud, S.; Star, A., *Adv. Mater.* **2009,** *21*, 4692-4695.

66. Ivanov, V.; Fonseca, A.; Nagy, J. B.; Lucas, A.; Lambin, P.; Bernaerts, D.; Zhang, X. B., *Carbon* **1995,** *33*, 1727-1738.

67. Hart, A. J.; Slocum, A. H., *J. Phys. Chem. B* **2006,** *110*, 8250-8257.

68. Anton, N. S.; Mehdi, M. Y.; Romaneh, J.; Ouseph, P. J.; Cohn, R. W.; Sumanasekera, G. U., *Nanotechnology* **2007,** *18*, 135301.

69. Hernandez, Y.; Nicolosi, V.; Lotya, M.; Blighe, F. M.; Sun, Z.; De, S.; McGovern, I. T.; Holland, B.; Byrne, M.; Gun'Ko, Y. K.; Boland, J. J.; Niraj, P.; Duesberg, G.; Krishnamurthy, S.; Goodhue, R.; Hutchison, J.; Scardaci, V.; Ferrari, A. C.; Coleman, J. N., *Nat. Nanotechnol.* **2008,** *3*, 563-568.

70. Emtsev, K. V.; Bostwick, A.; Horn, K.; Jobst, J.; Kellogg, G. L.; Ley, L.; McChesney, J. L.; Ohta, T.; Reshanov, S. A.; Rohrl, J.; Rotenberg, E.; Schmid, A. K.; Waldmann, D.; Weber, H. B.; Seyller, T., *Nat. Mater.* **2009,** *8*, 203-207.

71. Reina, A.; Jia, X.; Ho, J.; Nezich, D.; Son, H.; Bulovic, V.; Dresselhaus, M. S.; Kong, J., *Nano Lett.* **2008,** *9*, 30-35.

72. Lomeda, J. R.; Doyle, C. D.; Kosynkin, D. V.; Hwang, W.-F.; Tour, J. M., *J. Am. Chem. Soc.* **2008,** *130*, 16201-16206.

73. McAllister, M. J.; Li, J.-L.; Adamson, D. H.; Schniepp, H. C.; Abdala, A. A.; Liu, J.; Herrera-Alonso, M.; Milius, D. L.; Car, R.; Prud'homme, R. K.; Aksay, I. A., *Chem. Mater*. **2007,** *19*, 4396-4404.

74. Kosynkin, D. V.; Higginbotham, A. L.; Sinitskii, A.; Lomeda, J. R.; Dimiev, A.; Price, B. K.; Tour, J. M., *Nature* **2009,** *458*, 872-876.

75. Liu, N.; Luo, F.; Wu, H.; Liu, Y.; Zhang, C.; Chen, J., *Adv. Funct. Mater.* **2008,** *18*, 1518-1525.

76. Williams, G.; Seger, B.; Kamat, P. V., *ACS Nano* **2008,** *2*, 1487-1491.

77. Wang, H.; Maiyalagan, T.; Wang, X., *ACS Catalysis* **2012,** *2*, 781-794.

78. Han, W.-Q.; Kohler-Redlich, P.; Seeger, T.; Ernst, F.; Ruhle, M.; Grobert, N.; Hsu, W.-K.; Chang, B.-H.; Zhu, Y.-Q.; Kroto, H. W.; Walton, D. R. M.; Terrones, M.; Terrones, H., *Appl. Phys. Lett.* **2000,** *77*, 1807-1809.

79. Wang, X.; Li, X.; Zhang, L.; Yoon, Y.; Weber, P. K.; Wang, H.; Guo, J.; Dai, H., *Science* **2009,** *324*, 768-771.

80. Hong, W.; Bai, H.; Xu, Y.; Yao, Z.; Gu, Z.; Shi, G., *J. Phys. Chem. C* **2010,** *114*, 1822-1826.

81. Venkateswara Rao, C.; Ishikawa, Y., *J. Phys. Chem. C* **2012,** *116*, 4340-4346.

82. Matter, P. H.; Wang, E.; Arias, M.; Biddinger, E. J.; Ozkan, U. S., *J. Phys. Chem. B* **2006,** *110*, 18374-18384.

83. Yang, W.; Fellinger, T.-P.; Antonietti, M., *J. Am. Chem. Soc.* **2011,** *133*, 206-209.

84. Schilling, T.; Bron, M., *Electrochim. Acta* **2008,** *53*, 5379-5385.

85. Byon, H. R.; Suntivich, J.; Crumlin, E. J.; Shao-Horn, Y., *Phys. Chem. Chem. Phys.* **2011,** *13*, 21437-21445.

86. Schilling, T.; Okunola, A.; Masa, J.; Schuhmann, W.; Bron, M., *Electrochim. Acta* **2010,** *55*, 7597-7602.

87. Maldonado, S.; Stevenson, K. J., *J. Phys. Chem. B* **2004,** *108*, 11375-11383.

88. Kundu, S.; Nagaiah, T. C.; Xia, W.; Wang, Y.; Dommele, S. V.; Bitter, J. H.; Santa, M.; Grundmeier, G.; Bron, M.; Schuhmann, W., *J. Phys. Chem. C* **2009,** *113*, 14302-14310.

89. Su , D. S.; Zhang, J.; Frank, B.; Thomas, A.; Wang, X.; Paraknowitsch, J.; Schlögl, R., *ChemSusChem* **2010,** *3*, 169-180.

90. Choi, C. H.; Chung, M. W.; Park, S. H.; Woo, S. I., *RSC Advances* **2013,** *3*, 4246-4253.

91. Lin, Z.; Waller, G.; Liu, Y.; Liu, M.; Wong, C.-P., *Advanced Energy Materials* **2012,** *2*, 884-888.

92. Pels, J. R.; Kapteijn, F.; Moulijn, J. A.; Zhu, Q.; Thomas, K. M., *Carbon* **1995,** *33*, 1641-1653.

93. Artyushkova, K.; Kiefer, B.; Halevi, B.; Knop-Gericke, A.; Schlogl, R.; Atanassov, P., *Chem. Commun.* **2013,** *49*, 2539-2541.

94. Shao, Y.; Sui, J.; Yin, G.; Gao, Y., *Appl. Catal. B* **2008,** *79*, 89-99.

95. Kim, H.; Lee, K.; Woo, S. I.; Jung, Y., *Phys. Chem. Chem. Phys.* **2011,** *13*, 17505-17510.

96. Yin, J.; Qiu, Y.; Yu, J., *ECS Solid State Letters* **2013,** *2*, M37-M39.

97. Pumera, M.; Miyahara, Y., *Nanoscale* **2009,** *1*, 260-265.

98. Wu, G.; More, K. L.; Johnston, C. M.; Zelenay, P., *Science* **2011,** *332*, 443-447.

99. Eder, D., *Chem. Rev.* **2010,** *110*, 1348-1385.

100. Peng, X.; Chen, J.; Misewich, J. A.; Wong, S. S., *Chem. Soc. Rev.* **2009,** *38*, 1076-98.

101. Sun, C.-L.; Chen, L.-C.; Su, M.-C.; Hong, L.-S.; Chyan, O.; Hsu, C.-Y.; Chen, K.-H.; Chang, T.-F.; Chang, L., *Chem. Mater.* **2005,** *17*, 3749-3753.

102. Yang, D.-Q.; Sacher, E., *J. Phys. Chem. C* **2008,** *112*, 4075-4082.

103. Bommersbach, P.; Chaker, M.; Mohamedi, M.; Guay, D., *J. Phys. Chem. C* **2008,** *112*, 14672-14681.

104. Wu, B.; Kuang, Y.; Zhang, X.; Chen, J., *Nano Today* **2011,** *6*, 75-90.

105. Zhao, Y.; Fan, L.; Zhong, H.; Li, Y.; Yang, S., *Adv. Funct. Mater.* **2007,** *17*, 1537-1541.

106. Day, T. M.; Unwin, P. R.; Wilson, N. R.; Macpherson, J. V., *J. Am. Chem. Soc.* **2005,** *127*, 10639-10647.

107. Lorençon, E.; Ferlauto, A. S.; de Oliveira, S.; Miquita, D. R.; Resende, R. R.; Lacerda, R. G.; Ladeira, L. O., *ACS Appl. Mater. Interfaces* **2009,** *1*, 2104-2106.

108. Liu, X.-W.; Mao, J.-J.; Liu, P.-D.; Wei, X.-W., *Carbon* **2011,** *49*, 477-483.

109. Guo, S.; Dong, S.; Wang, E., *ACS Nano* **2009,** *4*, 547-555.

110. Azamian, B. R.; Coleman, K. S.; Davis, J. J.; Hanson, N.; Green, M. L. H., *Chem. Commun.* **2002,** *0*, 366-367.

111. Liu, L.; Wang, T.; Li, J.; Guo, Z.-X.; Dai, L.; Zhang, D.; Zhu, D., *Chem. Phys. Lett.* **2003,** *367*, 747-752.

112. Ding, M.; Sorescu, D. C.; Kotchey, G. P.; Star, A., *J. Am. Chem. Soc.* **2012,** *134*, 3472-3479.

113. Rahman, G. M. A.; Guldi, D. M.; Zambon, E.; Pasquato, L.; Tagmatarchis, N.; Prato, M., *Small* **2005,** *1*, 527-530.

114. White, R. J.; Luque, R.; Budarin, V. L.; Clark, J. H.; Macquarrie, D. J., *Chem. Soc. Rev.* **2009,** *38*, 481-494.

115. Li, W.; Liang, C.; Zhou, W.; Qiu, J.; Zhou, Z.; Sun, G.; Xin, Q., *J. Phys. Chem. B* **2003,** *107*, 6292-6299.

116. Kaniyoor, A.; Jafri, R. I.; Arockiadoss, T.; Ramaprabhu, S., *Nanoscale* **2009,** *1*, 382-386.

117. Guo, S.; Wen, D.; Zhai, Y.; Dong, S.; Wang, E., *ACS Nano* **2010,** *4*, 3959-3968.

118. Wu, H.; Wang, J.; Kang, X.; Wang, C.; Wang, D.; Liu, J.; Aksay, I. A.; Lin, Y., *Talanta* **2009,** *80*, 403-406.

119. Chen, A.; Holt-Hindle, P., *Chem. Rev.* **2010,** *110*, 3767-3804.

120. Pumera, M., *Chem. Rec.* **2009,** *9*, 211-223.

121. Brandon, N. P.; Skinner, S.; Steele, B. C., *Annu. Rev. Mater. Res.* **2003,** *33*, 183-213.

122. Kauffman, D. R.; Tang, Y.; Kichambare, P. D.; Jackovitz, J. F.; Star, A., *Energy Fuels* **2010,** *24*, 1877-1881.

123. Kymakis, E.; Amaratunga, G., *Appl. Phys. Lett.* **2002,** *80*, 112-114.

124. Kongkanand, A.; Martínez Domínguez, R.; Kamat, P. V., *Nano Lett.* **2007,** *7*, 676-680.

125. An, K. H.; Kim, W. S.; Park, Y. S.; Moon, J.-M.; Bae, D. J.; Lim, S. C.; Lee, Y. S.; Lee, Y. H., *Adv. Funct. Mater.* **2001,** *11*, 387-392.

126. Schlapbach, L.; Züttel, A., *Nature* **2001,** *414*, 353-358.

127. Katz, H. E., *Electroanal.* **2004,** *16*, 1837-1842.

128. Kruger, M.; Buitelaar, M. R.; Nussbaumer, T.; Schonenberger, C.; Forro, L., *Appl. Phys. Lett.* **2001,** *78*, 1291-1293.

129. Kruusma, J.; Mould, N.; Jurkschat, K.; Crossley, A.; Banks, C. E., *Electrochem. Commun.* **2007,** *9*, 2330-2333.

130. Meyers, J. P., *Electrochem. Soc. Interface* **2008**, 37.

131. Litster, S.; McLean, G., *J. Power Sources* **2004,** *130*, 61-76.

132. Arico, A. S.; Bruce, P.; Scrosati, B.; Tarascon, J.-M.; van Schalkwijk, W., *Nat. Mater.* **2005,** *4*, 366-377.

133. Wang, B., *J. Power Sources* **2005,** *152*, 1-15.

134. Paulus, U.; Wokaun, A.; Scherer, G.; Schmidt, T.; Stamenkovic, V.; Markovic, N. M.; Ross, P., *Electrochim. Acta* **2002,** *47*, 3787-3798.

135. Zhang, J.; Sasaki, K.; Sutter, E.; Adzic, R., *Science* **2007,** *315*, 220-222.

136. Wang, J.; Markovic, N.; Adzic, R., *J. Phys. Chem. B* **2004,** *108*, 4127-4133.

137. Stamenkovic, V. R.; Fowler, B.; Mun, B. S.; Wang, G.; Ross, P. N.; Lucas, C. A.; Marković, N. M., *Science* **2007,** *315*, 493-497.

138. Carmo, M.; Paganin, V. A.; Rosolen, J. M.; Gonzalez, E. R., *J. Power Sources* **2005,** *142*, 169-176.

139. Vante, N. A.; Jaegermann, W.; Tributsch, H.; Hoenle, W.; Yvon, K., *J. Am. Chem. Soc.* **1987,** *109*, 3251-3257.

140. Bezerra, C. W. B.; Zhang, L.; Lee, K.; Liu, H.; Marques, A. L. B.; Marques, E. P.; Wang, H.; Zhang, J., *Electrochim. Acta* **2008,** *53*, 4937-4951.

141. Collman, J. P.; Devaraj, N. K.; Decréau, R. A.; Yang, Y.; Yan, Y.-L.; Ebina, W.; Eberspacher, T. A.; Chidsey, C. E. D., *Science* **2007,** *315*, 1565-1568.

142. Winther-Jensen, B.; Winther-Jensen, O.; Forsyth, M.; MacFarlane, D. R., *Science* **2008,** *321*, 671-674.

143. Qu, L.; Liu, Y.; Baek, J.-B.; Dai, L., *ACS Nano* **2010,** *4*, 1321-1326.

144. Jasinski, R., *Nature* **1964,** *201*, 1212-1213.

145. Chen, P.; Xiao, T.-Y.; Qian, Y.-H.; Li, S.-S.; Yu, S.-H., *Adv. Mater.* **2013,** *25*, 3192-3196.

146. Zheng, Y.; Jiao, Y.; Jaroniec, M.; Jin, Y.; Qiao, S. Z., *Small* **2012,** *8*, 3550-3566.

147. Liu, G.; Li, X.; Lee, J.-W.; Popov, B. N., *Catalysis Science & Technology* **2011,** *1*, 207-217.

148. Li, Q.; Zhang, S.; Dai, L.; Li, L.-s., *J. Am. Chem. Soc.* **2012,** *134*, 18932-18935.

149. Xiong, C.; Wei, Z.; Hu, B.; Chen, S.; Li, L.; Guo, L.; Ding, W.; Liu, X.; Ji, W.; Wang, X., *J. Power Sources* **2012,** *215*, 216-220.

150. Wang, S.; Yu, D.; Dai, L.; Chang, D. W.; Baek, J.-B., *ACS Nano* **2011,** *5*, 6202-6209.

151. Wang, S.; Yu, D.; Dai, L., *J. Am. Chem. Soc.* **2011,** *133*, 5182-5185.

152. Ni, S.; Li, Z.; Yang, J., *Nanoscale* **2012,** *4*, 1184-1189.

153. Liu, R.; Wu, D.; Feng, X.; Müllen, K., *Angew. Chem. Int. Ed.* **2010,** *49*, 2565-2569.

154. Rao, C. V.; Cabrera, C. R.; Ishikawa, Y., *J Phys. Chem. Lett.* **2010,** *1*, 2622-2627.

155. Kurak, K. A.; Anderson, A. B., *J. Phys. Chem. C* **2009,** *113*, 6730-6734.

156. Yang, Z.; Nie, H.; Chen, X. a.; Chen, X.; Huang, S., *J. Power Sources* **2013,** *236*, 238-249.

157. Lai, L.; Potts, J. R.; Zhan, D.; Wang, L.; Poh, C. K.; Tang, C.; Gong, H.; Shen, Z.; Lin, J.; Ruoff, R. S., *Energy Environ. Sci.* **2012,** *5*, 7936-7942.

158. Sharifi, T.; Hu, G.; Jia, X.; Wågberg, T., *ACS Nano* **2012,** *6*, 8904-8912.

159. Gavrilov, N.; Pašti, I. A.; Mitrić, M.; Travas-Sejdić, J.; Ćirić-Marjanović, G.; Mentus, S. V., *J. Power Sources* **2012,** *220*, 306-316.

160. Lin, Z.; Song, M.-k.; Ding, Y.; Liu, Y.; Liu, M.; Wong, C.-p., *Phys. Chem. Chem. Phys.* **2012,** *14*, 3381-3387.

161. Jeon, I.-Y.; Yu, D.; Bae, S.-Y.; Choi, H.-J.; Chang, D. W.; Dai, L.; Baek, J.-B., *Chem. Mater.* **2011,** *23*, 3987-3992.

162. Yu, D.; Wei, L.; Jiang, W.; Wang, H.; Sun, B.; Zhang, Q.; Goh, K.; Si, R.; Chen, Y., *Nanoscale* **2013,** *5*, 3457-3464.

163. Lim, S. H.; Li, Z.; Poh, C. K.; Lai, L.; Lin, J., *J. Power Sources* **2012,** *214*, 15-20.

164. Choi, C. H.; Park, S. H.; Woo, S. I., *Appl. Catal. B* **2012,** *119–120*, 123-131.

165. Wen, Z.; Ci, S.; Zhang, F.; Feng, X.; Cui, S.; Mao, S.; Luo, S.; He, Z.; Chen, J., *Adv. Mater.* **2012,** *24*, 1399-1404.

166. Palaniselvam, T.; Aiyappa, H. B.; Kurungot, S., *J. Mater. Chem.* **2012,** *22*, 23799-23805.

167. Choi, C. H.; Park, S. H.; Woo, S. I., *Int. J. Hydrogen Energy* **2012,** *37*, 4563-4570.

168. Zhong, H.; Zhang, H.; Liu, S.; Deng, C.; Wang, M., *ChemSusChem* **2013,** *6*, 807-812.

169. Parvez, K.; Yang, S.; Hernandez, Y.; Winter, A.; Turchanin, A.; Feng, X.; Müllen, K., *ACS Nano* **2012,** *6*, 9541-9550.

170. Wu, Z.-S.; Yang, S.; Sun, Y.; Parvez, K.; Feng, X.; Müllen, K., *J. Am. Chem. Soc.* **2012,** *134*, 9082-9085.

171. Lefèvre, M.; Proietti, E.; Jaouen, F.; Dodelet, J.-P., *Science* **2009,** *324*, 71-74.

172. Li, Y.; Zhou, W.; Wang, H.; Xie, L.; Liang, Y.; Wei, F.; Idrobo, J.-C.; Pennycook, S. J.; Dai, H., *Nat. Nanotechnol.* **2012,** *7*, 394-400.

173. Sheng, Z.-H.; Gao, H.-L.; Bao, W.-J.; Wang, F.-B.; Xia, X.-H., *J. Mater. Chem.* **2012,** *22*, 390-395.

174. Yang, L.; Jiang, S.; Zhao, Y.; Zhu, L.; Chen, S.; Wang, X.; Wu, Q.; Ma, J.; Ma, Y.; Hu, Z., *Angew. Chem. Int. Ed.* **2011,** *50*, 7132-7135.

175. Liu, Z.-W.; Peng, F.; Wang, H.-J.; Yu, H.; Zheng, W.-X.; Yang, J., *Angew. Chem. Int. Ed.* **2011,** *50*, 3257-3261.

176. Liu, Z.; Peng, F.; Wang, H.; Yu, H.; Tan, J.; Zhu, L., *Catal. Commun.* **2011,** *16*, 35-38.

177. Yang, S.; Zhi, L.; Tang, K.; Feng, X.; Maier, J.; Müllen, K., *Adv. Funct. Mater.* **2012,** *22*, 3634-3640.

178. Yang, Z.; Yao, Z.; Li, G.; Fang, G.; Nie, H.; Liu, Z.; Zhou, X.; Chen, X. a.; Huang, S., *ACS Nano* **2011,** *6*, 205-211.

179. Jin, Z.; Nie, H.; Yang, Z.; Zhang, J.; Liu, Z.; Xu, X.; Huang, S., *Nanoscale* **2012,** *4*, 6455-6460.

180. Zheng, Y.; Jiao, Y.; Ge, L.; Jaroniec, M.; Qiao, S. Z., *Angew. Chem. Int. Ed.* **2013,** *52*, 3110-3116.

181. Zhao, Y.; Yang, L.; Chen, S.; Wang, X.; Ma, Y.; Wu, Q.; Jiang, Y.; Qian, W.; Hu, Z., *J. Am. Chem. Soc.* **2013,** *135*, 1201-1204.

182. Wang, S.; Zhang, L.; Xia, Z.; Roy, A.; Chang, D. W.; Baek, J.-B.; Dai, L., *Angew. Chem. Int. Ed.* **2012,** *51*, 4209-4212.

183. Wang , S.; Iyyamperumal , E.; Roy, A.; Xue, Y.; Yu, D.; Dai, L., *Angew. Chem. Int. Ed.* **2011,** *50*, 11756-11760.

184. Chisaka, M.; Iijima, T.; Ishihara, Y.; Suzuki, Y.; Inada, R.; Sakurai, Y., *Electrochim. Acta* **2012,** *85*, 399-410.

185. Choi, C. H.; Chung, M. W.; Kwon, H. C.; Park, S. H.; Woo, S. I., *Journal of Materials Chemistry A* **2013,** *1*, 3694-3699.

186. Choi, C. H.; Park, S. H.; Woo, S. I., *J. Mater. Chem.* **2012,** *22*, 12107-12115.

187. Liang, J.; Jiao, Y.; Jaroniec, M.; Qiao, S. Z., *Angew. Chem. Int. Ed.* **2012,** *51*, 11496-11500.

188. Choi, C. H.; Park, S. H.; Woo, S. I., *ACS Nano* **2012,** *6*, 7084-7091.

189. Zhang, L.; Xia, Z., *J. Phys. Chem. C* **2011,** *115*, 11170-11176.

190. Zhang, L.; Niu, J.; Dai, L.; Xia, Z., *Langmuir* **2012,** *28*, 7542-7550.

191. Grieshaber, D.; MacKenzie, R.; Vörös, J.; Reimhult, E., *Sensors* **2008,** *8*, 1400-1458.

192. Clark, L. C.; Lyons, C., *Ann. N. Y. Acad. Sci.* **1962,** *102*, 29-45.

193. Wang, J., *Chem. Rev.* **2008,** *108*, 814-825.

194. Wang, J., *Electroanal.* **2001,** *13*, 983-988.

195. Wang, J.; Liu, J.; Chen, L.; Lu, F., *Anal. Chem.* **1994,** *66*, 3600-3603.

196. Karyakin, A. A.; Gitelmacher, O. V.; Karyakina, E. E., *Anal. Chem.* **1995,** *67*, 2419-2423.

197. Cass, A. E. G.; Davis, G.; Francis, G. D.; Hill, H. A. O.; Aston, W. J.; Higgins, I. J.; Plotkin, E. V.; Scott, L. D. L.; Turner, A. P. F., *Anal. Chem.* **1984,** *56*, 667-671.

198. Bartlett, P. N.; Booth, S.; Caruana, D. J.; Kilburn, J. D.; Santamaría, C., *Anal. Chem.* **1997,** *69*, 734-742.

199. Patolsky, F.; Weizmann, Y.; Willner, I., *Angew. Chem. Int. Ed.* **2004,** *43*, 2113-2117.

200. Koopal, C.; Bos, A.; Nolte, R., *Sens. Actuators, B* **1994,** *18*, 166-170.

201. Palmisano, F.; Zambonin, P. G.; Centonze, D.; Quinto, M., *Anal. Chem.* **2002,** *74*, 5913-5918.

202. Hrapovic, S.; Liu, Y.; Male, K. B.; Luong, J. H. T., *Anal. Chem.* **2004,** *76*, 1083-1088.

203. Rivas, G. A.; Rubianes, M. D.; Rodríguez, M. C.; Ferreyra, N. F.; Luque, G. L.; Pedano, M. L.; Miscoria, S. A.; Parrado, C., *Talanta* **2007,** *74*, 291-307.

204. Zhao, Q.; Gan, Z.; Zhuang, Q., *Electroanal.* **2002,** *14*, 1609-1613.

205. Tang, Z. K.; Zhang, L.; Wang, N.; Zhang, X. X.; Wen, G. H.; Li, G. D.; Wang, J. N.; Chan, C. T.; Sheng, P., *Science* **2001,** *292*, 2462-2465.

206. So, H.-M.; Won, K.; Kim, Y. H.; Kim, B.-K.; Ryu, B. H.; Na, P. S.; Kim, H.; Lee, J.-O., *J. Am. Chem. Soc.* **2005,** *127*, 11906-11907.

207. Goldsmith, B. R.; Coroneus, J. G.; Khalap, V. R.; Kane, A. A.; Weiss, G. A.; Collins, P. G., *Science* **2007,** *315*, 77-81.

208. Tang, Y.; Kotchey, G. P.; Vedala, H.; Star, A., *Electroanal.* **2011,** *23*, 870-877.

209. Snow, E. S.; Perkins, F. K.; Robinson, J. A., *Chem. Soc. Rev.* **2006,** *35*, 790-798.

210. Agüí, L.; Yáñez-Sedeño, P.; Pingarrón, J. M., *Anal. Chim. Acta* **2008,** *622*, 11-47.

211. Allen, M. J.; Tung, V. C.; Kaner, R. B., *Chem. Rev.* **2009,** *110*, 132-145.

212. Kauffman, D. R.; Star, A., *Analyst* **2010,** *135*, 2790-2797.

213. Stankovich, S.; Piner, R. D.; Chen, X.; Wu, N.; Nguyen, S. T.; Ruoff, R. S., *J. Mater. Chem.* **2006,** *16*, 155-158.

214. Kovtyukhova, N. I.; Ollivier, P. J.; Martin, B. R.; Mallouk, T. E.; Chizhik, S. A.; Buzaneva, E. V.; Gorchinskiy, A. D., *Chem. Mater.* **1999,** *11*, 771-778.

215. Si, Y.; Samulski, E. T., *Nano Lett.* **2008,** *8*, 1679-1682.

216. Si, Y.; Samulski, E. T., *Chem. Mater.* **2008,** *20*, 6792-6797.

217. Zhang, Z.-B.; Liu, X.-J.; Campbell, E. E. B.; Zhang, S.-L., *J. Appl. Phys.* **2005,** *98*, 056103-3.

218. Banks, C. E.; Compton, R. G., *Anal. Sci.* **2005,** *21*, 1263-1268.

219. Garsany, Y.; Baturina, O. A.; Swider-Lyons, K. E.; Kocha, S. S., *Anal. Chem.* **2010,** *82*, 6321-6328.

220. Ang, P. K.; Chen, W.; Wee, A. T. S.; Loh, K. P., *J. Am. Chem. Soc.* **2008,** *130*, 14392-14393.

221. Rosenblatt, S.; Yaish, Y.; Park, J.; Gore, J.; Sazonova, V.; McEuen, P. L., *Nano Lett.* **2002,** *2*, 869-872.

222. DasA; PisanaS; ChakrabortyB; PiscanecS; Saha, S. K.; Waghmare, U. V.; Novoselov, K. S.; Krishnamurthy, H. R.; Geim, A. K.; Ferrari, A. C.; Sood, A. K., *Nat. Nanotechnol.* **2008,** *3*, 210-215.

223. Kauffman, D. R.; Star, A., *Nano Lett.* **2007,** *7*, 1863-1868.

224. Kauffman, D. R.; Sorescu, D. C.; Schofield, D. P.; Allen, B. L.; Jordan, K. D.; Star, A., *Nano Lett.* **2010,** *10*, 958-963.

225. Zangwill, A., *Physics at Surfaces*. Cambridge University Press: Cambridge, UK, 1988.

226. Kim, B.-K.; Park, N.; Na, P. S.; So, H.-M.; Kim, J.-J.; Kim, H.; Kong, K.-J.; Chang, H.; Ryu, B.-H.; Choi, Y.; Lee, J.-O., *Nanotechnology* **2006,** *17*, 496.

227. Che, G.; Lakshmi, B. B.; Fisher, E. R.; Martin, C. R., *Nature* **1998,** *393*, 346-349.

228. Mirabile Gattia, D.; Antisari, M. V.; Giorgi, L.; Marazzi, R.; Piscopiello, E.; Montone, A.; Bellitto, S.; Licoccia, S.; Traversa, E., *J. Power Sources* **2009,** *194*, 243-251.

229. Dicks, A. L., *J. Power Sources* **2006,** *156*, 128-141.

230. Park, H. S.; Choi, B. G.; Yang, S. H.; Shin, W. H.; Kang, J. K.; Jung, D.; Hong, W. H., *Small* **2009,** *5*, 1754-1760.

231. Guo, S.; Dong, S.; Wang, E., *Small* **2008,** *4*, 1133-1138.

232. Park, H. I.; Mushtaq, U.; Perello, D.; Lee, I.; Cho, S. K.; Star, A.; Yun, M., *Energy Fuels* **2007,** *21*, 2984-2990.

233. Kannan, R.; Kakade, B. A.; Pillai, V. K., *Angew. Chem. Int. Ed.* **2008,** *47*, 2653-2656.

234. Liu, C.; Wang, C.-C.; Kei, C.-C.; Hsueh, Y.-C.; Perng, T.-P., *Small* **2009,** *5*, 1535-1538.

235. Li, W.; Liang, C.; Qiu, J.; Zhou, W.; Han, H.; Wei, Z.; Sun, G.; Xin, Q., *Carbon* **2002,** *40*, 791-794.

236. Qu, L.; Zhao, Y.; Dai, L., *Small* **2006,** *2*, 1052-1059.

237. Rajesh, B.; Ravindranathan Thampi, K.; Bonard, J. M.; Xanthopoulos, N.; Mathieu, H. J.; Viswanathan, B., *J. Phys. Chem. B* **2003,** *107*, 2701-2708.

238. Mu, Y.; Liang, H.; Hu, J.; Jiang, L.; Wan, L., *J. Phys. Chem. B* **2005,** *109*, 22212-22216.

239. Xu, J.; Hua, K.; Sun, G.; Wang, C.; Lv, X.; Wang, Y., *Electrochem. Commun.* **2006,** *8*, 982-986.

240. Lebert, M.; Kaempgen, M.; Soehn, M.; Wirth, T.; Roth, S.; Nicoloso, N., *Catal. Today* **2009,** *143*, 64-68.

241. Shao, Y.; Yin, G.; Zhang, J.; Gao, Y., *Electrochim. Acta* **2006,** *51*, 5853-5857.

242. Wang, X.; Li, W.; Chen, Z.; Waje, M.; Yan, Y., *J. Power Sources* **2006,** *158*, 154-159.

243. Shaijumon, M. M.; Ramaprabhu, S.; Rajalakshmi, N., *Appl. Phys. Lett.* **2006,** *88*, 253105-3.

244. Brown, G. D., Deposition of dispersed metal particles onto substrates using supercritical fluids. U.S. Patent No. 6,958,308: 2005.

245. Bard, A. J. F., L.R., In *Electrochemical Methods: Fundamentals and Applications*, 2 ed.; John Wiley and Sons: New York, 2001; pp 231-232.

246. Mukerjee, S., *J. Appl. Electrochem.* **1990,** *20*, 537-548.

247. Watanabe, M.; Sei, H.; Stonehart, P., *J. Electroanal. Chem. Interfacial Electrochem.* **1989,** *261*, 375-387.

248. Barsoukov, E.; Macdonald, J. R., In *Impedance Spectroscopy: Theory, Experiment, and Applications*, 2 ed.; Barsoukov, E. M., J.R., Ed. John Wiley and Sons: Hoboken, NJ, 2005; pp 14-20.

249. Li, W.; Waje, M.; Chen, Z.; Larsen, P.; Yan, Y., *Carbon* **2010,** *48*, 995-1003.

250. Neergat, M.; Shukla, A. K., *J. Power Sources* **2001,** *102*, 317-321.

251. Yoon, K. H.; Choi, J. Y.; Jang, J. H.; Cho, Y. S.; Jo, K. H., *J. Appl. Electrochem.* **2000,** *30*, 121-124.

252. Wei, Z. D.; Zhang, S. T.; Tang, Z. Y.; Guo, H. T., *J. Appl. Electrochem.* **2000,** *30*, 723-725.

253. Benítez, R.; Chaparro, A. M.; Daza, L., *J. Power Sources* **2005,** *151*, 2-10.

254. Wang, J., *Electroanal.* **2005,** *17*, 7-14.

255. Alwarappan, S.; Erdem, A.; Liu, C.; Li, C.-Z., *J. Phys. Chem. C* **2009,** *113*, 8853-8857.

256. Terrones, M.; Terrones, H.; Grobert, N.; Hsu, W. K.; Zhu, Y. Q.; Hare, J. P.; Kroto, H. W.; Walton, D. R. M.; Kohler-Redlich, P.; Ruhle, M.; Zhang, J. P.; Cheetham, A. K., *Appl. Phys. Lett.* **1999,** *75*, 3932-3934.

257. Han, W.-Q.; Kohler-Redlich, P.; Seeger, T.; Ernst, F.; Ruhle, M.; Grobert, N.; Hsu, W.-K.; Chang, B.-H.; Zhu, Y.-Q.; Kroto, H. W.; Walton, D. R. M.; Terrones, M.; Terrones, H., *Appl. Phys. Lett.* **2000,** *77*, 1807-1809.

258. Wang, E. G., *J. Mater. Res.* **2006,** *21*, 2767-2773.

259. Wang, J., *Chem. Rev.* **2007,** *108*, 814-825.

260. Lefèvre, M.; Dodelet, J. P.; Bertrand, P., *J. Phys. Chem. B* **2002,** *106*, 8705-8713.

261. Lyon, J. L.; Stevenson, K. J., *Langmuir* **2007,** *23*, 11311-11318.

262. Liang, Y.; Li, Y.; Wang, H.; Dai, H., *J. Am. Chem. Soc.* **2013,** *135*, 2013-2036.

263. Ma, Y.; Sun, L.; Huang, W.; Zhang, L.; Zhao, J.; Fan, Q.; Huang, W., *J. Phys. Chem. C* **2011,** *115*, 24592-24597.

264. Chen, Z.; Higgins, D.; Chen, Z., *Electrochim. Acta* **2010,** *55*, 4799-4804.

265. Liu, Q.; Zhang, J., *Langmuir* **2013,** *29*, 3821-3828.

266. Maldonado, S.; Stevenson, K. J., *J. Phys. Chem. B* **2005,** *109*, 4707-4716.

267. Chen, Z.; Higgins, D.; Chen, Z., *Carbon* **2010,** *48*, 3057-3065.

268. Olson, T. S.; Pylypenko, S.; Fulghum, J. E.; Atanassov, P., *J. Electrochem. Soc.* **2010,** *157*, B54-B63.

269. Uhm, S.; Jeong, B.; Lee, J., *Electrochim. Acta* **2011,** *56*, 9186-9190.

270. Chen, T.; Cai, Z.; Yang, Z.; Li, L.; Sun, X.; Huang, T.; Yu, A.; Kia, H. G.; Peng, H., *Adv. Mater.* **2011,** *23*, 4620-4625.

271. Wang, Z.; Jia, R.; Zheng, J.; Zhao, J.; Li, L.; Song, J.; Zhu, Z., *ACS Nano* **2011,** *5*, 1677-1684.

272. Ma, Y.; Zhao, J.; Zhang, L.; Zhao, Y.; Fan, Q.; Li, X. a.; Hu, Z.; Huang, W., *Carbon* **2011,** *49*, 5292-5297.

273. Sheng, Z. H.; Shao, L.; Chen, J. J.; Bao, W. J.; Wang, F. B.; Xia, X. H., *ACS Nano* **2011,** *5*, 4350-4358.

274. Yu, D.; Zhang, Q.; Dai, L., *J. Am. Chem. Soc.* **2010,** *132*, 15127-15129.

275. Chen, S.; Bi, J.; Zhao, Y.; Yang, L.; Zhang, C.; Ma, Y.; Wu, Q.; Wang, X.; Hu, Z., *Adv. Mater.* **2012,** *24*, 5593-5597.

276. Yang, Z.; Nie, H.; Chen, X. a.; Chen, X.; Huang, S., *J. Power Sources* **2013,** *236*, 238-249.

277. Wiggins-Camacho, J. D.; Stevenson, K. J., *J. Phys. Chem. C* **2011,** *115*, 20002-20010.

278. van Dommele, S.; Romero-Izquirdo, A.; Brydson, R.; de Jong, K. P.; Bitter, J. H., *Carbon* **2008,** *46*, 138-148.

279. Lin, M.; Tan, J. P. Y.; Boothroyd, C.; Loh, K. P.; Tok, E. S.; Foo, Y.-L., *Nan Lett.* **2007,** *7*, 2234-2238.

280. Wulfsberg, G., *Inorganic Chemistry*. University Science Books: Sausalito, 2000.

281. Shin, D.; Jeong, B.; Mun, B. S.; Jeon, H.; Shin, H.-J.; Baik, J.; Lee, J., *J. Phys. Chem. C* **2013,** *117*, 11619-11624.

282. Thorum, M. S.; Hankett, J. M.; Gewirth, A. A., *J Phys. Chem. Lett.* **2011,** *2*, 295-298.

283. Bin, W., *J. Power Sources* **2005,** *152*, 1-15.

284. Titov, A.; Zapol, P.; Kral, P.; Liu, D.-J.; Iddir, H.; Baishya, K.; Curtiss, L. A., *J. Phys. Chem. C* **2009,** *113*, 21629-21634.

285. Feng, H.; Ma, J.; Hu, Z., *J. Mater. Chem.* **2010,** *20*, 1702-1708.

286. Kochubey, D.; Kaichev, V.; Saraev, A.; Tomyn, S.; Belov, A.; Voloshin, Y., *J. Phys. Chem. C* **2013,** *117*, 2753-2759.

287. Koslowski, U. I.; Abs-Wurmbach, I.; Fiechter, S.; Bogdanoff, P., *J. Phys. Chem. C* **2008,** *112*, 15356-15366.

288. Choi, J.-Y.; Higgins, D.; Chen, Z., *J. Electrochem. Soc.* **2012,** *159*, B86-B89.

289. Yin, J.; Qiu, Y.; Yu, J., *ECS Solid State Lett.* **2013,** *2*, M37-M39.

290. Ding, L.; Xin, Q.; Zhou, X.; Qiao, J.; Li, H.; Wang, H., *J. Appl. Electrochem.* **2013,** *43*, 43-51.

291. Haile, S. M., *Acta Mater.* **2003,** *51*, 5981-6000.

292. Zhao, Y.; Allen, B. L.; Star, A., *J. Phys. Chem. A* **2011,** *115*, 9536-9544.

293. Terrones, M.; Ajayan, P.; Banhart, F.; Blase, X.; Carroll, D.; Charlier, J.; Czerw, R.; Foley, B.; Grobert, N.; Kamalakaran, R., *Appl. Phys. A* **2002,** *74*, 355-361.

294. Maldonado, S.; Morin, S.; Stevenson, K. J., *Carbon* **2006,** *44*, 1429-1437.

295. Zhang, J.; Lei, J.; Pan, R.; Leng, C.; Hu, Z.; Ju, H., *Chem. Commun.* **2011,** *47*, 668-670.

296. Zhao, M. L.; Li, D. J.; Yuan, L.; Yue, Y. C.; Liu, H.; Sun, X., *Carbon* **2011,** *49*, 3125-3133.

297. Ma, X.; Wang, E.; Tilley, R.; Jefferson, D.; Zhou, W., *Appl. Phys. Lett.* **2000,** *77*, 4136-4138.

298. Zhao, Y.; Tang, Y.; Chen, Y.; Star, A., *ACS Nano* **2012,** *6*, 6912-6921.

299. Carrero-Sánchez, J. C.; Elías, A. L.; Mancilla, R.; Arrellín, G.; Terrones, H.; Laclette, J. P.; Terrones, M., *Nano Lett.* **2006,** *6*, 1609-1616.

300. Zhao, Y.; Tang, Y.; Star, A., *J. Vis. Exp.* **2013**, e50383.

301. Wang, Y.; Bai, X., *Mater. Lett.* **2009,** *63*, 206-208.

302. Shimamoto, D.; Fujisawa, K.; Muramatsu, H.; Hayashi, T.; Kim, Y. A.; Yanagisawa, T.; Endo, M.; Dresselhaus, M. S., *Carbon* **2010,** *48*, 3643-3647.

303. Inoshita, T.; Nakao, K.; Kamimura, H., *J. Phys. Soc. Jpn.* **1977,** *43*, 1237-1243.

304. Enoki, T.; Endo, M.; Suzuki, M., *Graphite intercalation compounds and applications*. Oxford University Press on Demand: 2003.

305. Dresselhaus, M. S.; Dresselhaus, G., *Adv. Phys.* **2002,** *51*, 1-186.

306. Sun, G.; Li, X.; Qu, Y.; Wang, X.; Yan, H.; Zhang, Y., *Mater. Lett.* **2008,** *62*, 703-706.

307. Disma, F.; Aymard, L.; Dupont, L.; Tarascon, J. M., *J. Electrochem. Soc.* **1996,** *143*, 3959-3972.

308. Richens, D. T., *The Chemistry of Aqua Ions: Synthesis, Structure and Reactivity: A Tour Through the Periodic Table of the Elements*. Wiley: 1997.